Stabilized and Functionalized Self Assembled Nanoparticle Arrays for Protein Separation

by

Narges Shaabani

A thesis submitted in partial fulfillment of the requirements for the degree of

Doctor of Philosophy

Department of Chemistry
University of Alberta

Abstract

This thesis reports a facile method to stabilize colloidal self-assembled (CSA) 310 and 50 nm nanoparticles packed in microchannels for high speed size-based separation of denatured proteins. Silica nanoparticles, self-assembled in a network of microfluidic channels, were stabilized with a methacrylate polymer prepared in situ through photopolymerization. The entrapment conditions were investigated to minimize the effect of the polymer matrix on the structure of packing and the separation properties of the CSA beds. Scanning electron microscopy (SEM) shows the methacrylate matrix links the nanoparticles at specific sphere-sphere contact points that improves the stability of the CSA structure at high electric fields (up to at least 1,800 V/cm) and allows fast and efficient separation. The optimized entrapped CSA beds demonstrated better separation performance than similarly prepared on-chip CSA beds without the polymer entrapment. Polymer entrapped CSA beds also exhibited superior protein resolving power. The minimum resolvable molecular weight difference of proteins in the polymer entrapped CSA bed is 1-2 kDa comparing ~9 kDa for the native silica CSA bed without polymer entrapment.

The method and the processes required to photograft charged monomer to 310 nm silica nanoparticle surface for native protein separation is described. Photo-initiated polymerization enabled coating the nanoparticles in microfluidic devices. The surface chemistry was then tailored to fit the specific application by subsequent photografting of the surface. This coating strategy allows a fast and robust wall coating with controlled surface chemistry and surface biocompatibility. The results indicate that the coatings are

quite effective in reducing protein adsorption, compared to a native silica particle packed bed.

Preface

This thesis is original work by Narges Shaabani. Some parts of this research (chapter 2, chapter 3, and chapter 4 of this thesis) have been published or presented as:

- Narges Shaabani, Abebaw Jemere, D. Jed Harrison, Stabilization of Colloidal Self Assembled Nanoparticle Arrays for On Chip Separation, *CSC Conference,* May 28, 2013 Quebec city (presentation)

- Narges Shaabani, Abebaw Jemere, D. Jed Harrison, High speed size based Proteins separation on Stabilized Colloidal Self Assembled (CSA) Nanoparticle Arrays, *Proceedings of Micro-Total Analysis Systems*, San Antonio, Texas, USA, (2402-2404) 2014.

- Narges Shaabani, Abebaw Jemere, D. Jed Harrison, Electrochromatography proteins separation on polymar coated silica nanoparticles packed in microchannles, *Proceedings of Micro-Total Analysis*, Korea, USA, (1945-1946) 2015.

- Narges Shaabani, Abebaw Jemere, D. Jed Harrison, Size-based proteins separation using polymer entrapped colloidal self-assembled nanoparticles on-chip, *32nd International Symposium on Microscope Separations and Bioanalysis*, April 3-7, 2016, Niagara-on-the-Lake, Ontario (presentation)

- Narges Shaabani, Abebaw Jemere, D. Jed Harrison, Size based proteins separation on stabilized colloidal self-assembled nanoparticle packed microchip column, *Electrophoresis*, 2016, (In press)

I was responsible for the data collection and analysis as well as the manuscripts composition. Dr. Jed Harrison (supervisory author) and Dr. Abebaw Jemere were involved with concept formation and manuscript composition.

Dedicated to

To my beloved husband, Reza

Acknowledgements

I am eternally grateful and thankful to Allah, the Almighty Who continues to bless my life.

Foremost, I would like to express my sincere gratitude to my supervisor Dr. D. Jed Harrison for his continuous support, patience and guidance and for providing me with a rich and rewarding academic experience. Despite being very busy as a departmental chair, he spent enough time to help me with my research. I also faithfully thank him for supporting me in attending conferences and offering me opportunities to broaden my horizon and perspective.

I thank Dr. Robert Campbell, Dr. Juli Gibbs-Davis, and Dr. Michael J. Serpe for being in my supervisory committee and for their insightful comments during my candidacy exam, which helped me to develop a more profound understanding of the nature of this research.

Thanks to the members of my examining committee Dr. Aaron Wheeler, Dr. Steven H. Bergens, and Dr. M. Joanne Lemieux for reviewing my thesis.

I thank Dr. Abebaw Jemere, Dr. Reza Sabbagh and Dr. Hamid Ramezani for the brainstorming discussions on different aspects of my research. I thank support and friendship from all DJH group members, including Wenmin Ye, Neda Nazemifard, Ali MalekpourKoupaei, Huiying Sheng, Sabrina Peng, Yonxin Zhao, Reshma Singh, Mohammad Azim, Le Zhang, Ya Zhou, Yufeng Zhao, Jing Ji, Md Minhajul Islam, and Yuting Hou.

A greatest thank you to my parents for their love and sacrifice. No words can fully express my gratitude to them and my sisters Nasim and Negin. They have supported me in any and every possible way throughout my education. Many thanks to my grandparents and parents-in-law whom I am grateful for their assistance. Your prayer for me is what sustains me thus far.

Words fall short of expressing my deep appreciation to my beloved spouse, Reza, for his love, understanding, and support. Also special thanks go to my little angles Sara and Saba. I feel lucky to have such lovely companions to spend the rest of my life with.

Lastly, I offer my regards and blessings to all of those who supported me in any respect during the completion of the thesis.

CONTENTS

LIST OF FIGURES

LIST OF TABLES

LIST OF ABBREVIATIONS

ACN	Acetonitrile
BSA	Bovine Serum Albumin
BMA	Butyl MethAcrylate
CGE	Capillary Gel Electrophoresis
CSA	Colloidal Self-Assembly
CQAs	Critical Guality Attributes
DC	Direct Current
DLS	Dynamic Light Scattering
DNA	Deoxyribo Nucleic Acid
EDL	Electrical Double Layer
EOF	Electroosmotic Flow
EDMA	Ethylene Glycol Dimethacrylate
EDX	Energy Dispersive X-Ray Analysis
FITC	Fluorescein IsoThioCyanate
FTIR	Fourier Transform Infrared Spectroscopy
HEMA	Hydroxy Ethyl Methacrylate
HETP	Height Equivalent Theoretical Plate
MS	Mass Spectrometry
META	[2-(Methacryloyloxy) Ethyl]TrimethylAmmonium chloride
PA	Poly Acrylamide
PDMS	Poly(DimethylSiloxane)
POC	Point-Of-Care
PGA	Polyethylene glycol
RDF	Radial Distribution Function
RSD	Relative Standard Deviation
rMAb	Recombinant Monoclonal Antibody
SDS	Sodium Dodecyl Sulfate

SEM	Scanning Electron Microscopy
SBMA	SulfoBetaine MethAcrylate
TAS	Total Analysis Systems
TBE	Tris-Borate-EDTA
TOF-SIMS	Time-of-Flight Secondary Ion Mass Spectrometry
TEM	Transmission Electron Microscopy
UV	UltraViolet
XPS	X-ray Photoelectron Spectroscopy

LIST OF NOMENCLATURE

a	Pore size
D	Diffusion coefficient
E	Electric field
f	Friction coefficient
H	Plate height
I	Current
K_B	Boltzmann constant
K^{-1}	Thickness of the double layer
l	Capillary effective length
m	Total number of ions
n_i	Density of the i_{th} ion
N	Theoretical plates
Q	Total charge
R_g	Radius of gyration
R_s	Resolution
t	Time
V	Length of the crystal
y	Voltage
W	Peak width

Greek symbols

μ_{EOF}	Electro osmotic mobility

μ_{app}	Apparent mobility
μ_e	Electrophoretic mobility
ζ	Zeta potential
η	Dynamic viscosity of liquid phase
ϕ_0	Surface potential
ρ	Density
ψ	Global Orientational Order Parameter

LIST OF CHEMICAL STRUCTURES

Benzoin

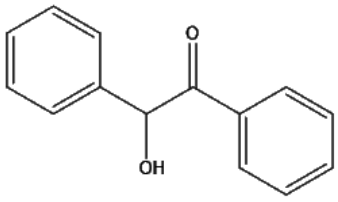

4-(dimethylamino) benzophenone

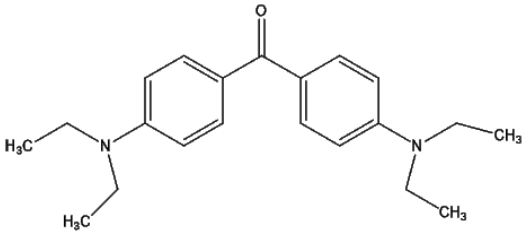

Ethylene Glycol Dimethacrylate (EDMA)

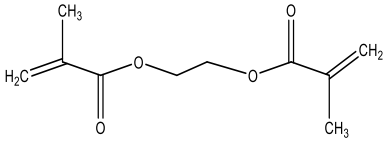

2-Hydroxy Ethyl Methacrylate (HEMA)

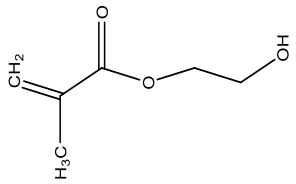

2-(Methacryloyloxy) Ethyl Trimethyl Ammonium chloride (METAC)

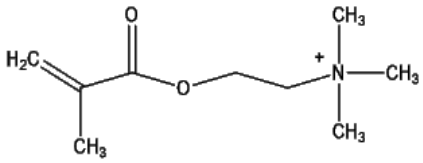

SulfoBetaine MethAcrylate (SBMA)

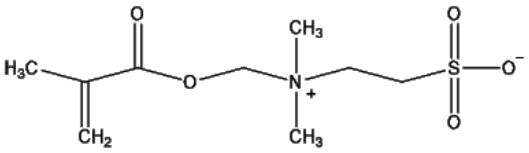

Fluorescein Isothiocynate (FITC)

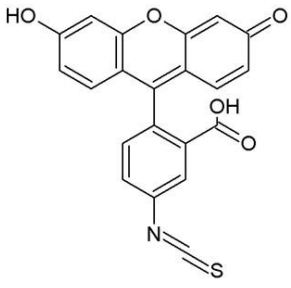

CHAPTER 1: INTRODUCTION

1.1 Background and motivations

The study of proteins and their function is central to understanding both cells and organisms. Methods for efficient separation and purification of proteins are of utmost importance in diagnostics, chemical biology, proteomics, and genomics [1–3]. Micro total analysis systems (μTAS), also known as "lab-on-a-chip" technology, has been developing rapidly since its introduction in the early 1990s [4]. Microfluidics, generally defined as the science and technology of manipulating small amounts of fluids (10^{-9} to 10^{-15} L), has been a keystone idea for the miniaturization of analytical devices and systems, and it offers opportunities to develop new separation methods and materials. The miniaturization and the concept of total analysis systems (TAS) initiated in 1990 by Manz et al. [4]. Works of Harrison [5–8], Ramsey [9–11], Mathies [12–14], and Whitesides [15–17] developed the concept to achieve short analysis times, small amounts of samples and the ability to integrate and automate processes. These efforts have rendered the impact of this technology on life-sciences more significant. Separation of these biological molecules with electrokinetic microfluidic chips has found numerous applications embracing clinical and pharmaceutical, [18–21] food and agricultural [22–25] as well as proteomic and metabolomics analysis [26–28].

Numerous micro-/nanofabricated nanoporous sieving matrices have been studied as alternatives to randomly structured gels for size based separations of biomolecules [29–

[37]. These rigid, fabricated sieving structures have long-term stability compared to gels, which are typically prepared fresh for each analysis, and provide a means to improve the efficiency and speed of separation. Micro-/nanofabrication of sieving matrices, however, requires sophisticated time consuming procedures, such as electron beam lithography and deep reactive ion etching, and result in two-dimensional architectures, all of which impedes their applications on a routine basis.

Separation beds formed by colloidal self-assembly (CSA) of nanoparticles provide a means to make porous networks for on-chip size based separation of proteins and DNA [38–40]. The pore size of the sieving matrix in CSA is determined by the size of the nanoparticles, and can be tuned to maximize separation performance for a given biomolecule, as demonstrated by Zeng and Harrison [38]. However, high speed and efficiency require high electric fields, which native silica particle beds cannot withstand. In this thesis we employ a combination of CSA particle beds with organic polymer entrapment of the particles for stabilization, fabricated using low resolution soft-lithography, to produce a highly efficient sieving media within the interstitial particle space. The procedure offers an alternative to polyacrylamide (PA) gels and to nanofabricated post structures, yielding a highly efficient sieving matrix for size based electrophoretic separation of proteins.

1.2 Motivations and scope

Achieving high quality electrophoretic and electrochromatographic separation of protein suitable for commercial, clinical and point-of-care (POC) diagnosis is an open and challenging field of research worldwide. The quality of a protein separation is dependent on the separating matrix, the conditions under which the electrophoresis is run and the properties of the molecule being separated. This thesis is focused on stabilization and functionalization of the matrix. Previously, a microfluidic colloidal self-assemble (CSA) approach was developed in the Harrison group for DNA and protein separation [38,41]. However, high speed and efficiency requires high electric fields, which native silica particle beds cannot withstand. Here we report the polymer entrapment of CSA beds composed of 540, 310, and 50 nm silica particles. The photo-polymerization of porogenic methacrylates is fast, uncomplicated and more versatile than other methods [42–45]. This report demonstrates the technique works with smaller particles and pore structures than have been employed in the past [38]. Given the wall-coating characteristics of porogenic polymers in extremely small dimensions, the method is ideally suited to stabilization of smaller particles. Furthermore, introducing a second photografting step allows immobilization of various surface functional groups in photolithographically defined patterns, which can be selected to control electroosmatic flow (EOF), separation of intact proteins, and prevents protein adsorption on the packed particles.

This thesis is organized as described below:

Chapter 2 discusses a method of polymer entrapment of CSA beds, characterization methods and parameter optimization. The characterization methods are divided into imaging and nonimaging techniques. Scanning Electron Microscope (SEM), Energy Dispersive X-Ray Analysis (EDX), Time-of-Flight Secondary Ion Mass Spectrometry (TOF-SIMS), and Transmission electron microscopy (TEM) are imaging techniques. Measuring the EOF and joule heating within the entrapped self-assembled colloidal arrays is also discussed, as are nonimaging characterization. Fast and reproducible detection of fluorescein was utilized to demonstrate the feasibility of using the entrapped CSA bed as a stable bed at high field.

In chapter 3 we are focused on the separation performance of a wide range of proteins masses from 6.5 to 660 kDa, using polymer entrapped nanosieve CSA beds. The polymer entrapped CSA bed was evaluated in terms of plate height (H) vs migration rate of trypsin inhibitor by varying the applied electric field and the data fitted to the classical Van Deemter equation [46]. The effects of electric field intensity, particle size, and detection length on separation efficiency were studied. In addition, the separation mechanism, presumed to be Ogston sieving, and the feasibility of molecular weight determination are discussed. The results presented here demonstrate the flexibility and high reproducibility of this entrapped CSA bed methodology for protein separation across a wide size ranges.

Chapter 4 reports the photografting of entrapped CSA bed with [2-(methacryloyloxy) ethyl] trimethylammonium chloride (META) monomer which is positively charged, and with sulfobetaine methacrylate (SBMA) as a zwitterionic

monomer. The experimental processes of the surface photografting, characterization, and application of surface devices for separating of acidic and basic intact proteins, are described in this chapter. The results show the improved separation efficiency of these proteins compared to non-grafted surfaces of HEMA on CSA beds.

An in situ study of crack formation with 50 nm silica nanoparticles used in the packing process is discussed in chapter 5. The packing procedure was optimized, and the 50 nm silica particle bed entrapped by HEMA coating provided better separation efficiency than native 50 nm silica beds. We show that an electric field of 1250 V/cm can be used for protein separation, which is a big improvement compared to previous work with 50 nm particles.

Chapter 6 concludes the present progress of this work, discusses some future perspective and presents initial data obtained with real sample applications.

Before we move on, a brief review of recent trends in protein separation, separation matrixes and the applications, separation principles and fundamental, and methods of surface characterizations are presented to facilitate discussions.

1.3 Recent trend in protein separation

Proteins, complex biopolymers composed of amino acids, are the most important biomolecules. Acting as enzymes, enzyme substrates and inhibitors, hormones, receptors, structural units, antigens, antibodies, drugs, and toxins, they play a vitally important role in all living organisms [47]. By incorporating older technologies with advantages brought by microfluidics concept many important biochemical analysis method could benefit [48]. This was demonstrated for the first time by Effenhauser and co-workers [49]. In that work,

they reported the first successful application of polyacrylamide gel electrophoresis in micromachined planar glass structures [49]. A high performance separation of five proteins on a polyacrylamide gel in a microfluidic channel was performed by Herr and Singh [50]. Such a separation was done in less than 30 seconds, which is much faster than the conventional approach. They studied the effect of pore size and electrical field strength upon the performance of separation.

Nagata et al. [51] demonstrated an effective method for separating proteins using polymethyl methacrylate (PMMA) microchips. Their method effectively utilized reversed flow (EOF) as counter flow to electrophoretic migration of proteins using dynamically SDS-coated PMMA microchips. High-speed (6 s) separation of proteins and peptides up to 116 kDa was successfully achieved using this system.

A two-dimensional microfluidic system is reported for protein separations combining isoelectric focusing (IEF) and SDS-PAGE, employing in situ photopolymerized PA gels [52,53]. In an alternate approach to the microchannel array used in that work, a microchamber was fabricated to support 2-D protein separations (Figure 1-1) [54]. Spatially distinct PA gels were formed by photopatterning; one for IEF with immobilized pH gradient and another for sizing of focused proteins.

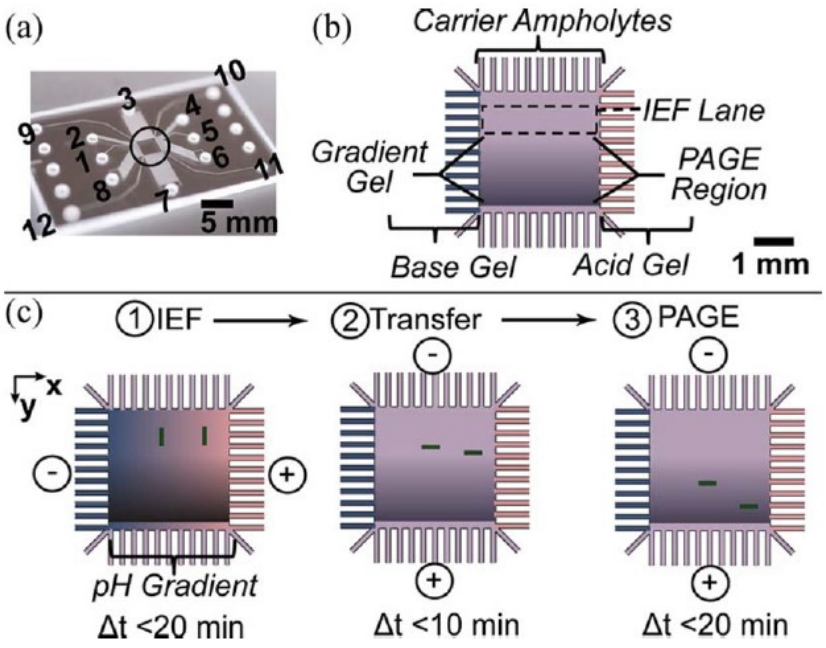

Figure 1-1. Design and operation of gel photopatterning for microchamber 2D electrophoresis (2DE). (a) Etched glass microdevice features microchamber flanked by channels for sample loading and electric field control. (b) The device houses contiguous PA gel regions with distinct chemicophysical properties to define the IEF and PAGE separation axes. (c) Operation procedure of micro-2DE (Reprinted with permission from T. Augusto et al. [54]*. Copyright 2013, ©American Chemical Society).*

Colloidal self-assembly and the use of colloids is used for making structures with tunable narrow pore size distribution and flexible ordered/disordered morphologies. This is opposed to what is attainable by use of any kind of gel and resulted in moving bioseparation research in another direction. Zeng and Harrison [38] showed for the first time that a colloidal crystal can be fabricated in a microfluidic channel via CSA using silica particles of 160 nm diameter. The sieving matrix with an average pore size of about 25 nm, was used to separate five proteins with molecular weights ranging from 20.1 to 116 kDa within a few minutes, reliably and reproducibly. Based on the measured

mobility, a governing SDS-protein complex electromigration was diagnosed. Wirth's group stabilized CSA silica nanoparticles in a glass microcapillary and used their beds to investigate electrochromatographic protein separation. They achieved a plate height of 50 nm for native proteins by electrochromatography [42]. They also modified 350 and 500 nm silica particles with a brush layer of polyacrylamide for size based separation of SDS denatured proteins. Plate heights of 400 nm were obtained in that work [55].

1.4 Separation matrix

The separation matrix is one of the most important functional elements in microfluidic applications. The separation matrix in microfluidics can be divided into several categories, like organic gel, monolith polymer, micro/nanoparticles, and micro/nanomachined structures.

1.4.1 Gel

Electrophoresis traditionally has been performed in anti-convective media, such as polyacrylamide or agarose gels. A gel-based sieving matrix can be largely categorized into crosslinked gels and non-crosslinked gels [56]. Crosslinked gels have a well-defined gel pore structure (Figure 1-2) [57].

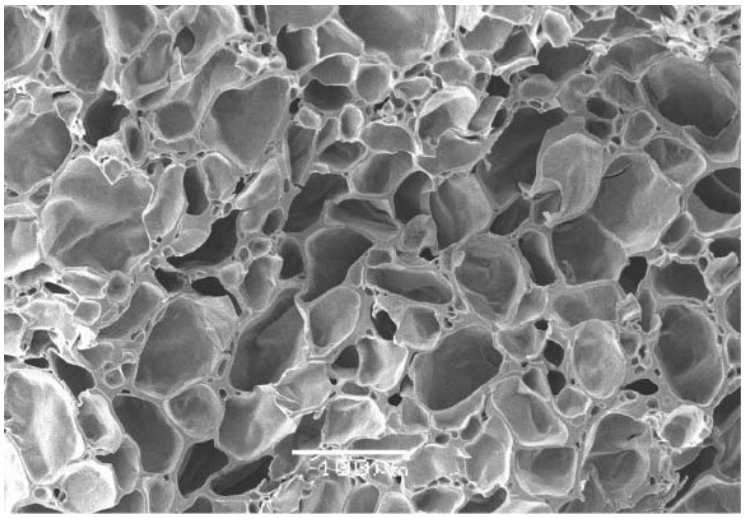

Figure 1-2. SEM image of macroporous polyacrylamide gel network (Reprinted with permission from F. Plieva et al. [57] Copyright © 2006, Royal Society of Chemistry).

The pore size strongly depends on total monomer (%T) and crosslinker concentration. Polyacrylamide gel is the most widely used crosslinked sieving matrix. Because of extremely high viscosity, the gels are usually polymerized inside the capillary [13,58] or microchannels [54,56,59–65]. Gels also provide hydrodynamic resistance, to eliminate cross flow, and to balance pressure between channels [3]. However, conventional gels suffer from some common disadvantages such as long analysis times, low efficiencies, low mechanical strength, high swelling ratio, and low tolerance for strong inorganic solvents and extreme pH [66,67].

1.4.2 Monolith polymer and confinement effect

In the early 1990s a macroscopic rigid porous monolith (Figure 1-3), prepared in situ by a thermally initiated polymerization process was introduced [68]. A number of

applications were explored, including HPLC and CEC from small molecules, chiral compounds, proteins, peptides, and nucleic acids [68–71]. Monolithic capillary columns are attractive alternatives as a sieving matrix , with benefits from the absence of retaining frits, low backpressure, and fast mass transfer [72,73]. The monoliths can be classified as polymer monoliths, silica monoliths, and organic–silica hybrid monoliths. Polymer monoliths are widely used as stationary phases, with advantages of facile preparation by polymerization of monomers in a porogenic solvent, high chemical stability over a wide pH range, and ease of modification with various functional groups [71]. Organic polymer-based monolithic columns, such as polystyrenes, polymethacrylates, and polyacrylamides have good stability to pH and are easy to prepare and tune the surface chemistry [74–77]. Free-radical polymerization, especially thermally initiated or photoinitiated polymerization, is conventionally used to prepare polymer monoliths, with suitable functional monomers and cross-linker monomers being chosen [75,78]. Most polymer monoliths are based on styrene-divinylbenzene and/or methacrylate copolymerization.

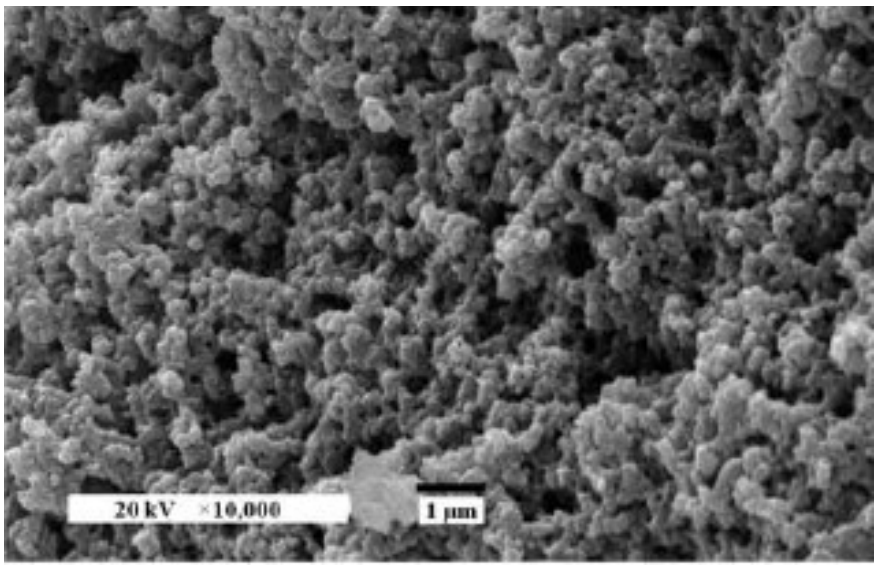

Figure 1-3. SEM images of organic–silica hybrid monolith (Reprinted with permission from Z. Zhang et al. [74], Copyright © 2006, Royal Society of Chemistry).

One of the methods of polymerization is based on photoinitiated free radical polymerization. In free radical polymerization, a photoinitiator absorb lights and undergoes homolytic decomposition in an excited state to produce free radicals. As an example, benzoin decomposing under UV exposure can be described as follows [79]:

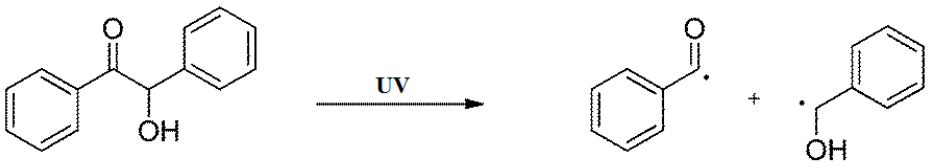

The subsequent polymerization the radical initiator follows the path indicated below:

Initiation

$$\text{Initiator} + h\nu \longrightarrow R^{\bullet}$$

$$R^{\bullet} + M \longrightarrow RM^{\bullet}$$

Propagation

$$RM^{\bullet} + M_n \longrightarrow RM^{\bullet}_{n+1}$$

Termination

combination

$$RM^{\bullet}_n + {}^{\bullet}M_m R \longrightarrow RM_n M_m R$$

disproportionatio

$$RM^{\bullet}_n + {}^{\bullet}M_m R \longrightarrow RM_n + M_m R$$

Figure 1-4. Mechanism of free radical polymerization, where R is radical and M is monomer.

In the free radical mechanism of radiation curable systems, light absorbed by a photoinitiator generates free-radicals which induce cross-linking reactions of a mixture of functionalized oligomers and monomers to generate the polymer [80]. The mechanism which is shown in Figure 1-4 includes three basic steps: initiation, chain propagation,

and chain termination. The three steps are depicted in the scheme where $R^{\bullet}$ represents the radical that forms upon interaction with radiation during initiation, and M is a monomer. The active monomer that is formed is then propagated to create growing polymer chain radicals. In photocurable materials the propagation step involves reactions of the chain radicals with reactive double bonds of the monomers. The termination reaction usually proceeds through combination, in which two chain radicals are joined together, or through disproportionation, which occurs when an atom (typically hydrogen) is transferred from one radical chain to another resulting in two polymer chains.

Porous polymer monoliths have been prepared by photoinitiated polymerization of butyl methacrylate (BMA) and ethylene glycol dimethacrylate (EDMA) monomers in porogenic solvent of methanol [81]. Suzhu Yu and coworkers [81] showed porosity of the porous polymers is mainly dependent on porogen concentration. Pore size of the porous polymers is greatly affected by UV intensity, fraction of initiator, fraction of crosslink agent, and porogen solvent concentration. A higher fraction of porogenic methanol will result in porous polymers with higher porosity and larger pore size; a higher fraction of initiator, EDMA crosslinker as well as higher UV intensity usually leads to the formation of polymers with smaller pore size.

The classical mechanism of pore formation that occurs during the polymerization process depends on the type of porogen used for the reaction. In the process, the solvent is a better solvating agent for the monomer than the polymer. Therefore, the initiated nuclei are precipitated and enlarged by their continuing polymerization and by capturing other branches. Finally, nuclei are associated into clusters by polymer chains that crosslink the near nuclei, and the cluster remains dispersed within the inert solvent. The

interconnected matrix becomes reinforced by crosslinking, which leads to the final porous polymer network. The solvent remains trapped in the voids of the crosslinked polymer [82].

The physical and chemical properties of monolith polymers can be readily tuned by adjusting the polymerization mixture composition. Figure 1-5a shows SEM images of the morphological evolution of porous polymer monoliths within capillaries, when controlled by scaling limits associated with the containment volume. When the ratio of the capillary's diameter to the pore size of the bulk monolith is less than 5, photopolymerized structures evolve to a single polymer layer on the wall surface. The SEM image in Figure 1-5b shows a fairly smooth polymer film thickness of 260 nm formed on the wall of a 7 μm deep microchannel. The thickness of the polymer layer can be tuned by adjusting the monomer concentration [83].

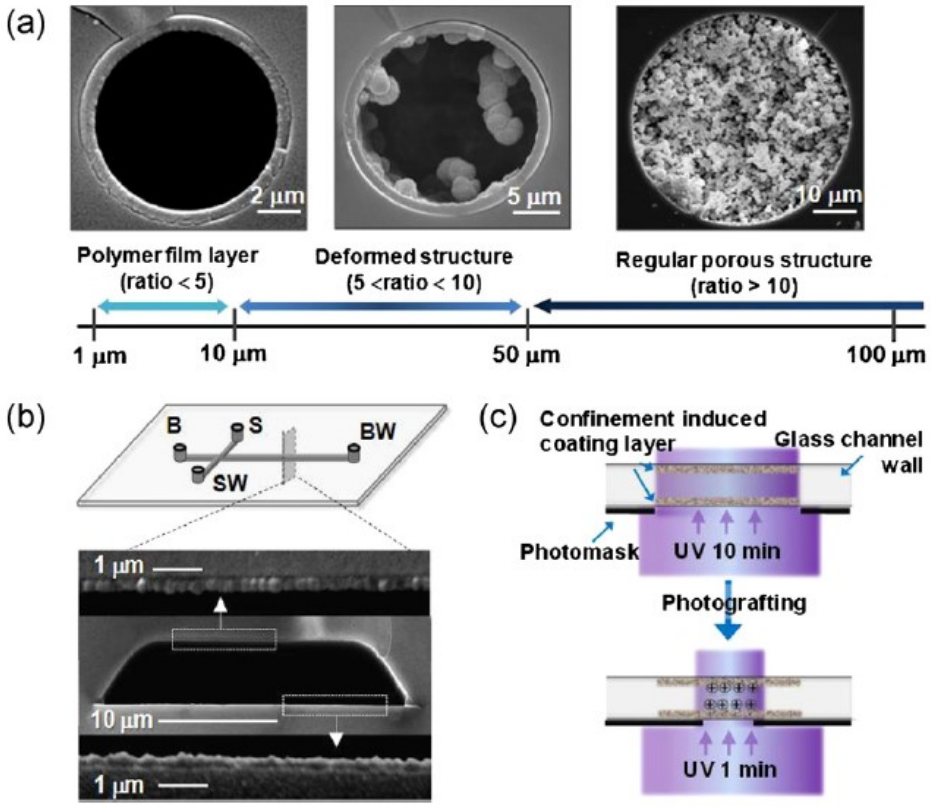

Figure 1-5. (a) The morphological evolution of porous polymer monoliths within conduit controlled by scaling limits. As a ratio of spatial scaling to bulk monolithic pore size decreases, the material becomes more porous and sparse. At the ratio of less than 5, a uniform polymer coating with thickness in the range of hundreds of nanometers is obtained. (b) Microfluidic chip layout and cross-sectional SEM view of microfluidic channel with 260 nm thick polymer coating. (c) Depiction of photopatterning a HEMA layer, then photografting with versatile surface chemistries in a microfluidic channel (Reprinted from M. He et al. [83], Copyright (2012), with permission from Elsevier).

1.4.3 Micro/nanomachined structures

In the early 1990s, the group of Austin [29] pioneered the use of microfabricated post arrays to replace the gel matrix for DNA analysis. Since then, a variety of

micro/nanofluidic structures have been developed that utilize different separation mechanisms.

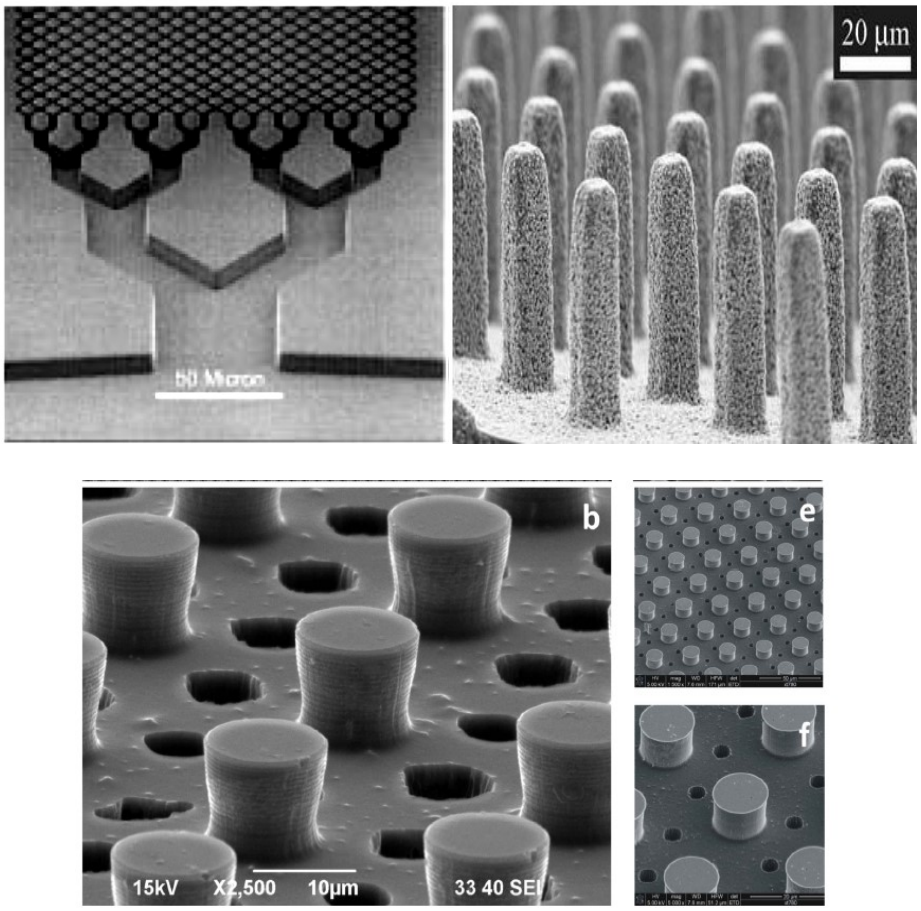

Figure 1-6. a) A 10µm thick monolith column microfabricated by reactive etching on quartz microchip based liquid phase chromatography, (Reprinted with permission from B. He et al, [84] Copyright © 2006, Royal Society of Chemistry). b) An array of micropillars made by replication from a PDMS mold(Reprinted with permission from T Rosqvist et al. [85] Copyright © 2002 Elsevier Science B.V. All rights reserved). c) Super-hydrophobic surfaces are designed and microfabricated. These comprise silicon micropillars arranged to form a regular hexagonal motif; the devices are therefore modified to incorporate, throughout the substrate, a pattern of holes, conveniently aligned with the pillars [86].

Figure 1-6 presents typical micrometer sized structures of different geometries, produced by plasma etching on quartz [84], imprinting in a PDMS substrate [85], and a silicon micropatterned structure [86]. He et al. [84] used a nanocolumn fabricated structure for liquid chromatography for separation of nonretained and retained rhodamine 123 at 1700 V/cm in a 4.5 cm column length. Plate heights in these columns were typically 0.6 μm in the nonretained and 1.3 μm in the retained modes of operation. They concluded that micromachining provides a route to high efficiency micro- and nanovolume liquid chromatography columns that is simpler and probably more reproducible than the conventional packed column approach. The technical limitations of nanolithography, such as very high cost, tedious fabrication steps, and challenges in fabrication for practical application still impede the applications of micron and sub-micron lithographically patterned separation columns [40,87].

1.4.4 Colloidal Self-Assembly (CSA) and stabilization

Spontaneous organization of monodispersed micro or nanoparticles is termed colloidal self-assembly (CSA). Self-assembled colloidal crystals have a relatively simple fabrication process and produce a crystalline or poly-crystalline three-dimensional structure. The hexagonal close packed lattice formed by CSA creates a lattice of pores with a highly tortuous pathway that will lead to frequent collision between analytes and particle surfaces. The pore size of CSA structure is around 15% of the particle size, which is the radius of narrowest tunnel surrounded by three adjacent spherical particles (Figure 1-7). A simple 2D mathematical model, shown in Figure 1-7, was used to calculate the pore size, with $r = (1/(\cos 30°)-1)\ R = 0.154\ R$.

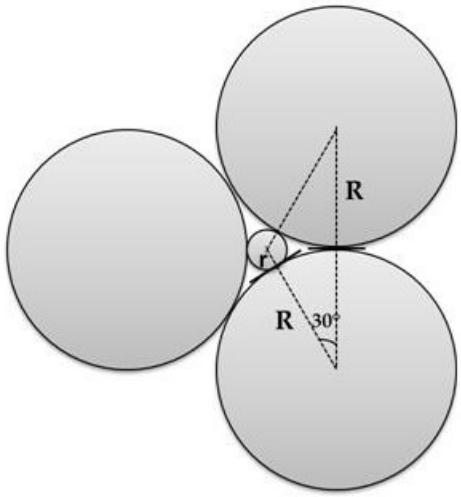

Figure 1-7. Structure of Pore size calculation.

This uniquely ordered porous structure has attracted interests in the fields of separation [38]. Self-assembled colloidal lattices have been employed to probe Brownian diffusion and electrophoretic migration [88,89] of confined single biopolymer molecules. One of the most studied applications of colloidal crystals in the literature has been in photonics [90], [91]. When the sizes of particles become comparable to the wavelengths of light, they strongly interact with it, confining and controlling photons of a specific wavelength. Hence propagation of light of a given wavelength can be blocked by the organized structure of particles in a lattice. The advantages brought by these nanoparticle arrays, including narrow pore size distribution, tunable morphology, mechanical stability, and ability to incorporate within microfluidics, make them an excellent candidate to be considered for sized-based separation of sodium dodecylsulfate (SDS)-protein complexes. However, their CSA beds are stable only at a low voltage (~300 V/ cm). Due to bonding by van der Waals forces and/or hydrogen bonds, the immobilization of the CSA bed is relatively weak, so the beds are not able to withstand a high voltage. High

voltages are the key factor improving the separation efficiency in CE and electrochromatography so better stability is needed [38].

A number of groups have attempted to stabilize CSA nanostructures for high performance separations for both on-chip and glass capillary based separations. Wirth's group stabilized CSA silica nanoparticles in glass capillaries using a horizontal polymerization technique, achieving a plate height of 50 nm for native proteins using 1,400 V/cm in electrochromatography [92] and 400 nm for size based separation of SDS denatured proteins [43]. Gong et al. [44] integrated a nano-film into a three-layered microfluidic device, serving as a frit to confine the nanoparticles in the microchannels, and showed the separation of fluorescein and 5-carboxyfluorescein by applying 125 V/cm, but did not report separation performance. These methods of CSA immobilization can be complicated, so alternative thermal approaches have been sought [45],[93]. Park et al. [45] used a hot embossing machine to thermally bond a cyclic olefin copolymer plate onto an on-chip CSA silica nanocrystal to "immobilize' the CSA. They demonstrated high speed capillary electrochromatography (CEC) of amino acids at ~1,300 V/cm. Liao et. al. [93] reported the use of thermal stabilization of CSA for on-chip separation of fluorescein isothiocyanate (FITC) labeled peptides and amino acids. In that work they achieved 500 nm plate heights for FITC using applied field strength of 1,000 V/cm, and reported crack free structures. Preventing crack formation in CSA beds during drying, a necessary consequence of thermal curing, is known to be challenging [37,41], so an alternative approach to stabilization would be valuable for achieving a high yield of functional devices from a fabrication run.

The use of organic polymers to overcome column instability in frit-less capillary columns packed with microparticles for CEC and HPLC separations has been reported [94–99], and polymers are explored here as a route to stabilizing sub-micron particle beds. Remcho [94] and Oleschuk [95–98] groups used in situ polymerization of methacrylate polymers to entrap 3 – 5 μm stationary phases in glass capillaries to overcome column instability for fritless CEC and HPLC separations. They showed that by using a minimum amount of organic polymer the interstitial spaces remain free for liquid flow. Harrison et al. previously reported that when the ratio of an open microchannel's size to the pore size of a bulk porogenic polymer system is less than 5, a single polymer layer forms on the wall surface, instead of a porous monolith column in the channel [83]. The interstitial space between particles in CSA structures (e.g. ~47 nm pore size for 310 nm silica nanoparticles) is well within the range where confinement leads to surface coatings instead of porous monoliths, when working with porogenic methacrylate compositions. Consequently, these same porogenic methacrylates are well suited to stabilizing CSA nanoparticles by photopolymerization in situ to coat the walls and bind the particles, without forming other structures within the interstitial space of the particles.

1.5 Photografting

The photografting of solid surfaces with layers of polymers has become a very important technique used in areas such as microelectronic packaging, biochips, or pH sensitive membranes [100,101]. Surface photografting enables the introduction of specific properties derived from the grafted layer, while also preserving the bulk and structural properties of the underlying material [102]. Figure 1-8 illustrates the proposed grafting

process. Initially, only a limited number of polymer chains grow from the surface [103]. As the polymerization continues, the degree of branching increases, since grafting also occurs via H-abstraction from the already grafted chains. While the density of chains increases, cross-linking becomes increasingly prevalent, and finally, a dense, cross-linked polymer network is formed. Considering the nature of the grafting reactions, forming a polymer layer cross-linked via intermolecular termination reactions of the branched polymer chains, the cross-linking density must clearly depend on the distance between the individual chains [103].

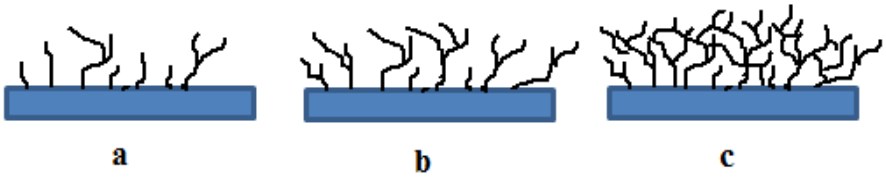

Figure 1-8. Schematic representation of the growing polymer chains during photografting with increasing irradiation time from (a) to (c)[103].

An appealing approach involves the packing of a microchannel with particles, as this significantly increases the available surface area and enables the introduction of specific chemistries into the device. Moreover, grafting of a particle surface could considerably increase the functional capabilities [104–106]. Zheng and coworkers [107] demonstrated poly(SBMA) grafted gold surfaces are highly resistant to protein adsorption. They showed that the polymer layers prepared all have excellent protein-resistant properties, with thickness ranges between 5 and 12 nm. Frechet and other research groups used the photografting technique to create axial gradient functionality for multi-enzyme reactions and pH gradient separation [103]. He et al. demonstrated

photografting of SBMA onto HEMA coated surfaces for use in CE [83]. They showed CE separation of a FITC-BSA digested with the microchip, with 15 resolved peaks. Compared to the results for neutral HEMA coated channels, SBMA grafted HEMA coated channels gave longer retention times and more resolved peaks under the same conditions, indicating better separation ability [83].

1.6 Electrophoresis of proteins

1.6.1 Fundamentals of Electrophoresis

Figure 1-9 illustrates schematically the most general model for an electrical double layer, where the surface charge is negative and a layer of some ionic and nonionic species in the solution is specifically absorbed on the surface. Such specific absorption is not just due to Coulombic interactions, but is mainly resulted from chemical affinity of ionic species to the solid surface (Delgado et al. [108]). Outside the layer of specifically absorbed ions, counter ions (cations) are attracted by the negatively charged surface due to the Coulombic force only. Based on the model shown in Figure 1-9, the plane located at $x = \beta_i$ is called the inner Helmholtz plane (IHP) with no water of hydration and the plane at $x = \beta_d$ is called the outer Helmholtz plane (OHP), in which the ions are hydrated. The IHP is the plane cutting through the center of the adsorbed species. The OHP is the plane cutting through the counter ions at their position of closest approach. The region between $x = 0$ and $x = \beta_d$ is often named the Stern layer, or the compact part of the double layer. The portion extending from $x = \beta_d$ is called the diffuse layer or the diffuse part of the double layer. The concentration of counter ions in the diffuse layer decreases as the location moves away from the surface. The plane located at $x = \beta_\zeta$ is called the shear

plane (SP). The well-known zeta potential is defined as the potential difference between this plane and the bulk solution. In general, SP is not co-planar with the OHP. At the shear plane, it is assumed that the viscosity of the liquid medium jumps discontinuously from infinity in the Stern layer to a finite value in the diffuse layer. The shear plane is the boundary that separates the EDL into a mobile part and an immobile part. For the sake of convenience, the zeta potential ζ is taken to be equivalent to the potential at the OHP in most circumstances, i.e. $\Psi_d = \zeta$ [109].

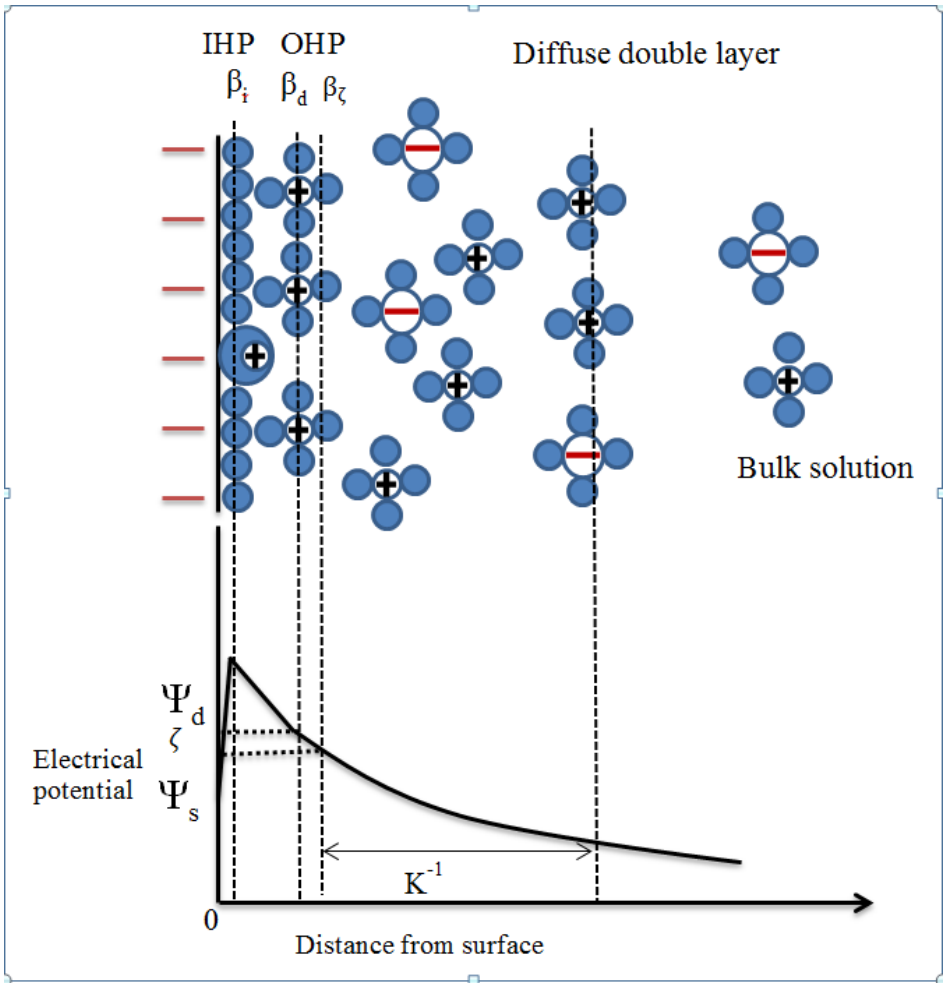

Figure 1-9. Schematic illustration of electric double layer (EDL) of a negatively charged surface, filled circles are H_2O and others are ions or surface charge.

The thickness of the EDL, a property of the electrolyte solution, based on the Debye-Huckel equation can be estimated via the following equation

$$k^{-1} = \sqrt{\frac{\in k_b T}{2e^2 I}} \qquad 1\text{-}1$$

Where ϵ is the dielectric permittivity of the electrolyte solution, k_b is the Boltzmann constant and e is the elementary charge. The ionic strength, I, is calculated by

$$I = \frac{1}{2}\sum_{i=1}^{m} {z_i}^2 n_i \qquad 1\text{-}2$$

with z_i, n_i and m being valence, density of the ith ion and total number of ions, respectively. When a negatively charged object immersed in an electrolyte is subjected to an external electrical field, $\vec{E}$, both the object and its surrounding cloud of ions start to move towards the electrode that has the opposite type charge. i.e. negatively charged ions towards anode and the surrounding cations towards cathode. Hence, there is a hydrodynamic interaction between the object and its surrounding ions. The free solution electrophoretic mobility of the charged object is defined as [110]

$$\mu = \frac{|\vec{V}|}{|\vec{E}|} \qquad 1\text{-}3$$

where $\vec{V}$ is the velocity of the migrating object [111]. Based on the thickness of the EDL two limiting cases have been considered. First, when the EDL thickness is larger than the

object, i.e. $k^{-1} \gg R_g$, the electric and viscous forces equilibrate each other; hence the mobility can be estimated via [110]:

$$\mu = \frac{Q}{f} \qquad 1\text{-}4$$

where Q is the total charge and f is the friction coefficient calculated by

$$f = 6\pi\eta R \qquad 1\text{-}5$$

where η and R are the viscosity of solvent, and radius of the object respectively. The second limiting case includes the Smoluchowski model, the mobility for the case when the Debye length is very thin compared to the object size, i.e. $k^{-1} \ll R_g$, can be estimated as [110]:

$$\mu = \frac{\epsilon\phi_0}{\eta} \approx \frac{\sigma k^{-1}}{4\pi\eta} \qquad 1\text{-}6$$

where ϕ_0 and σ are the surface potential and charge density, respectively. In this regime the mobility is not dependent on particle size.

1.7 Electroosmotic flow (EOF)

Electroosmotic flow (EOF) is the bulk movement of an aqueous solution along a stationary solid surface, which has an electrical double layer (EDL) as illustrated in Figure 1-9 [108,112]. The flow results from applying an electric field in the presence of free ions and the charged surface at the solid-liquid interface. The surface charge attracts

counter ions from solution, creating an electric double layer at the interface. The field parallel to the surface mobilizes anions to the anode and cations to the cathode. Since the negative surface is immobile, this creates a net flow of cations and solvent in the double layer towards the anode. In the solution bulk, the motion of anions and cations cancel each other, so only the double layer region outside the plane of shear (Figure 1-9) creates the electroosmotic flow. Once an external electric field is applied, charged species start to migrate along the field due to an electrostatic force, F_{el}. In addition, the double-layer is also dragged by an electrostatic force, F_{ret}, in the direction opposite to the particle motion, and the bulk solvent exerts a frictional force, F_f (Figure 1-10). The apparent velocity comes from the balance of the three forces. Electrophoretic mobility, μ is the ratio of the velocity with respect to an applied electric field. Viscosity and laminar flow effects then generate a plug flow of solvent in the bulk of the fluid. The mobility of EOF can be expressed as:

$$\mu_{EOF} = \frac{\epsilon\zeta}{\eta} \qquad 1\text{-}7$$

while the velocity of EOF can be expressed as [112]:

$$\upsilon_{EOF} = \frac{\epsilon\zeta}{\eta}E \qquad 1\text{-}8$$

where ϵ is the dielectric constant, η is the solution viscosity, ζ is the zeta potential and E is the electric field strength. The solution ionic strength and the surface charge have a profound influence on the zeta potential. Consequently, EOF is always strongly dependent on these two parameters.

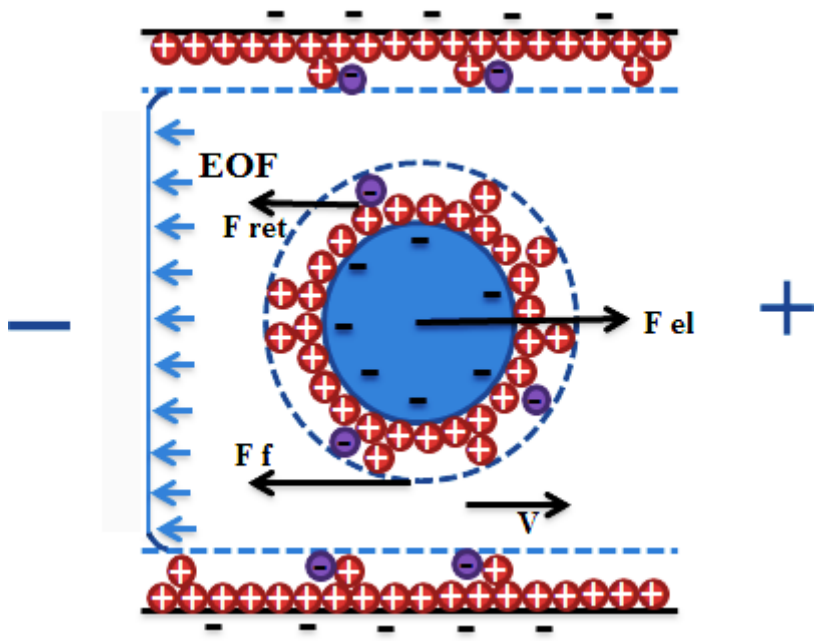

Figure 1-10. Electrophoresis of a negatively charged particle in an electrolyte solution with negatively charged substrate, anions and cations are shown.

A unique characteristic of EOF in the capillary is the flat profile of the flow, as shown in Figure 1-11a. Since the driving force of the flow is uniformly distributed along the capillary there is no pressure drop within the capillary, and the flow is nearly uniform throughout. The flat flow profile is beneficial since it does not directly contribute to the dispersion of solute zones. This is in contrast to that generated by an external pump which yields a laminar or parabolic flow due to the shear force at the wall (Figure 1-11b). The figure shows that the flow rate drops off rapidly at the wall. This quiescent solution layer is caused by friction against flow at the surface. Since this layer extends a short way into the solution, it is relatively unimportant to the overall separation process [66]. Another benefit of the EOF is that it causes movement of nearly all species, regardless of charge, in the same direction.

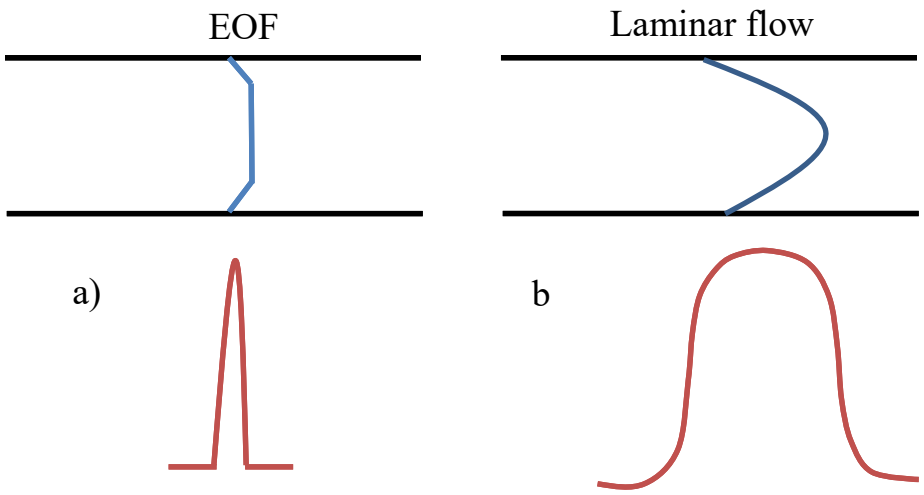

Figure 1-11. Flow profile and corresponding solute zone.

1.8 Size-based protein separation

Natural proteins are heteropolymers composed of covalently bonded amino acid residues. They are ubiquitous and essential for living organisms [33]. Proteins have different electrical charges and unique native shapes determined by hydrogen, hydrophobic, and disulfide linkages of different branches on the backbone the protein. They are denatured in the presence of heat and/or a detergent, such as sodium dodecyl sulfate (SDS). As a chaotrope, SDS binds to both native and denatured proteins, and unfolding is driven by the higher affinity for the denatured state [110]. The mode of SDS binding to proteins [113] is according to the concentration of surfactant: whether at the level of sub-CMC (critical micelle concentration) or beyond. At sub-CMC concentrations, SDS monomers bind to proteins by predominantly hydrophobic interactions, causing unfolding of the tertiary structure, and at concentrations higher than the CMC, the micelles nucleate on the hydrophobic patches of the protein chain driving, it to expand (Figure 1-12) [113]. The driving force for the expansion emanates from charge–charge repulsion between the

micelles and between the micelles and anionic side chains of the protein. Bhuyan showed that highly denatured and negatively charged cytochrome c interacts with SDS, suggesting that the interactions are hydrophobic in nature, and the effect is expansion of the chain [113]. Above the CMC the micellar rosettes on the protein chain deposited by cooperative aggregation of SDS monomers give the complex a necklace-like look [114]. As shown in Figure 1-12 the ‘‘necklace model’’ for SDS–protein interaction has two versions: in one, the hydrophobic patches along the protein chain act as nucleation sites for micelle growth, and in the other, the protein wraps around the micelles.

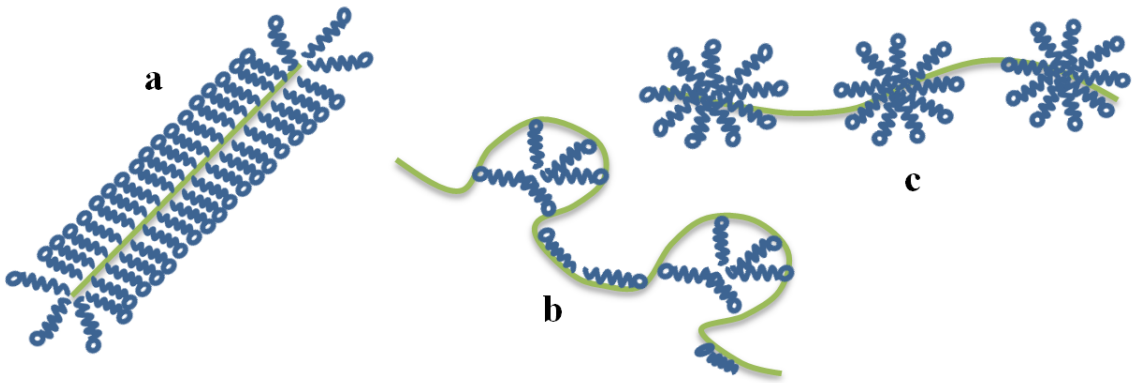

Figure 1-12. Structural models for protein-surfactant complexes. (a) Surfactant molecules cover the denatured protein chain forming a rod-like micelle; (b) Surfactant micelles are decorated by the denatured protein; (c) Micelles are formed along the denatured protein forming a necklace like structure.

The separation mechanisms of gel electrophoresis are not yet understood fully at the microscopic level [81,115–117]. Depending on the relative size of the macromolecule (radius of gyration, R_g) compared with the gel pore size (a), three basic separation mechanisms have emerged to explain how flexible linear macromolecules migrate through a gel medium. These models are Ogston sieving ($R_g / a < 1$), entropic trapping ($R_g / a = 1$) and reptation ($R_g / a > 1$) (Figure 1-13).

1.8.1 Ogston sieving

In Ogston sieving, the macromolecule is smaller than the gel pores. Because $R_g/a < 1$, the molecule moves rather freely through the gel matrix (Figure 1-13a). The molecule adopts a random coil and is not influenced by the surroundings, except through friction. The concept of Ogston sieving has been studied extensively by Rodbard and Chrambach using Ogston's calculation for the pore-size distributions in random arrays of geometrically idealized obstacles [118]. The Ogston sieving process has been suggested as an electric-field-driven partitioning process [59,113,117]. Based on the Ogston sieving model, the logarithm of the electrophoretic mobility of the SDS-protein objects are proportional to their molecular sizes. i.e. $\ln \mu \propto -M$ [119,120].

1.8.2 Entropic trapping

Entropic trapping applies when $R_g/a = 1$ and the conformation of the flexible macromolecule must deform or fluctuate to pass through the gel medium (Figure 1-13b). The molecule's coil shape changes to fit through the pores, with an entropic energy penalty. In the entropic trapping regime the logarithm of the mobility of the SDS-protein complexes is proportional to the logarithm of the molecular weights. i.e. $\ln \mu \propto -\ln M$. Hence a log-log plot of mobilities versus molecular weights should have a negative unit slope at the limit of very small electric field strength [120,121].

1.8.3 Reptation

Reptation can be envisioned as a long linear flexible macromolecule occupying multiple pores, threading its way through the gel in a snake-like fashion (Figure 1-13c)

[122]. Lumpkin [123] discovered that mobilities will also be governed by the magnitude of the electrical field. i.e. $\mu = \frac{1}{M} + bE^2$ where b is a function of the mesh size of the lattice network, charge and segment length of the migrating species and E is electrical field strength [120].

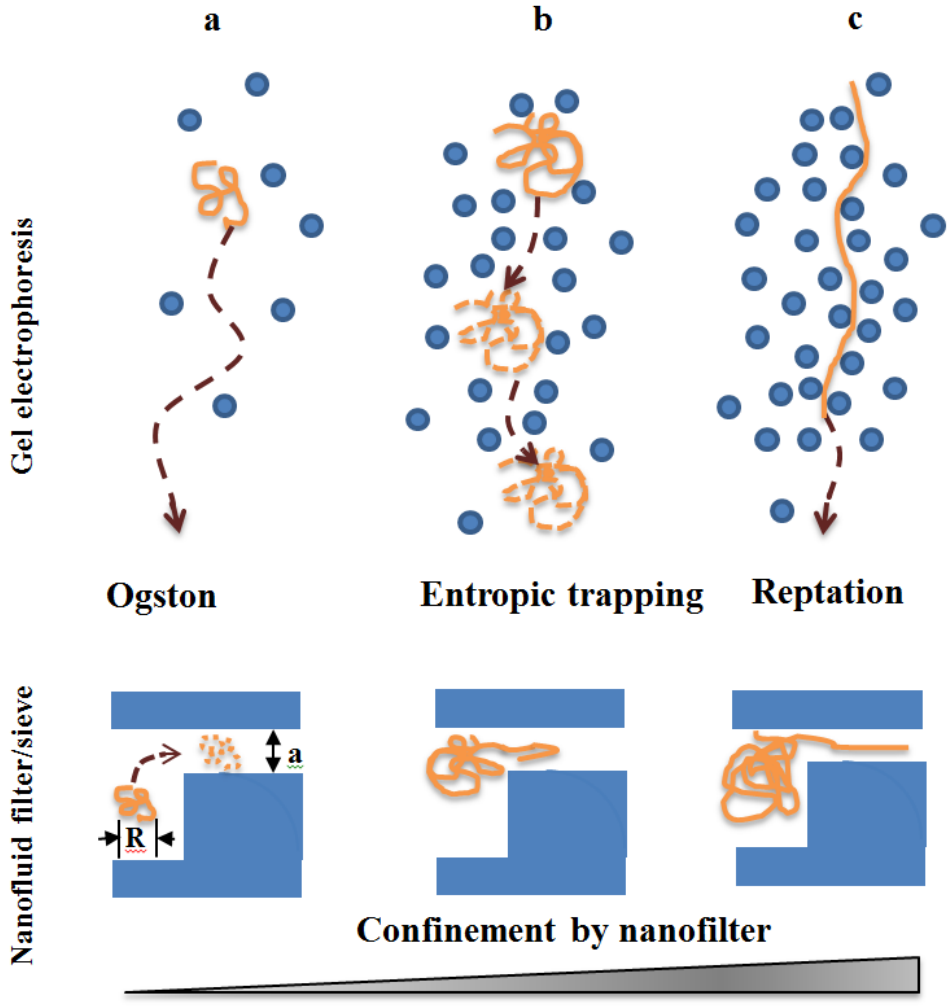

Figure 1-13. Different sieving regimes: gel electrophoresis (top) versus artificial nanofluidic sieves and filters (bottom). (a) Ogston sieving mechanism, (b) Entropic trapping mechanism, and (c) Reptation mechanism. Circles are posts or immobile gel structures.

1.9 Separation efficiency

The basis of separation in electrokinetic separation is either the difference in electrophoretic mobility of ions under an applied field, chromatographic interaction with a stationary phase, or a combination of both. The basic equation proposed by Gidding [124] to calculate the theoretical plates can be used to determine efficiency in electrokinetic separation. The number of theoretical plates, N, can be obtained by

$$N = \left(\frac{l}{\sigma}\right)^2 \qquad 1\text{-}9$$

where l is capillary effective length, and can be related to the height equivalent to a theoretical plate (HETP), H, by

$$H = \left(\frac{l}{N}\right) \qquad 1\text{-}10$$

Under ideal conditions (small injection plug length and no solute-wall interactions) the sole contribution to solute-zone broadening in CE can be considered to be longitudinal diffusion along the capillary. Radial diffusion across the capillary is unimportant due to the plug flow profile. Thus, the efficiency can be related to the molecular diffusion term in chromatography [66]. That is

$$\sigma^2 = 2Dt = \frac{2DlL}{\mu_e V} \qquad 1\text{-}11$$

where D is the diffusion coefficient of solute. Substituting equation 1-11 into equation 1-9 yields a fundamental electrophoretic expression for plate number

$$N = \frac{\mu_e V l}{2DL} = \frac{\mu_e E l}{2D} \qquad 1\text{-}12$$

From equation 1-12, the reason for the application of high fields is evident. This follows simply because the solute spends less time in the capillary at high field and has less time to diffuse. In addition, this equation shows that large molecules such as proteins and DNA, which have low diffusion coefficients, will show less dispersion than small molecules.

The theoretical plate number can be determined directly from an electropherogram, using, for example,

$$N = 5.54\left(\frac{t}{W_{1/2}}\right)^2 \qquad 1\text{-}13$$

where t is migration time and $W_{1/2}$ is temporal peak width at half height. Resolution of sample components is the ultimate goal in separation science. Resolution is most simply defined as [125]:

$$R = \frac{2(t_2 - t_1)}{W_1 + W_2} \qquad 1\text{-}14$$

where t is migration time and W is baseline peak width. The resolution of two components can also be expressed with respect to efficiency. Equation 1-15 [66] shows that

there is a square root relation between resolution and voltage. The voltage must be quadrupled to double the resolution.

$$R = \frac{1}{4\sqrt{2}} (\Delta\mu)\left(\frac{V}{D(\bar{\mu} + \mu_{EOF})}\right)^{1/2} \quad \text{1-15}$$

Separation by electrophoresis is based on differences in protein velocity in an electric field. The velocity of a protein can be given by equation 1-16:

$$V = \mu_{app} E \quad \text{1-16}$$

The electric field is simply the quotient of the applied voltage and channel length (in V/cm). The mobility, for a given protein and medium, is a constant which is characteristic of that protein. The mobility is determined by the electric force that the protein experiences [126].

The resolution of two proteins in a separation depends on two factors; peak sharpness and selectivity, as indicated in equation 1-17.

$$R_S = \frac{\sqrt{\frac{L}{H}}}{4} \frac{\Delta t}{t} \quad \text{1-17}$$

where the term L is the separation length and H is the plate height, which is proportional to peak variance. The equation shows that the smaller the value of H, the sharper the peak. The term $\Delta t/t$ describes the selectivity for the two components being separated,

where Δt is the difference in migration time of the two components and t is their average migration time. Equation 1-17 shows that improvements in resolution could come from increased length [92]. On the other hand, it is important that the sample plug length be minimized during the injection. If the length is longer than the dispersion caused by diffusion, efficiency and resolution are sacrificed [126–128]. However, when the ratio of injection plug length to the total length of the microchannel is decreased by increasing the detection length, the efficiency and resolution are improved.

1.10 Surface chemistry characterizations techniques

In the following part the different characterization methods which were employed in this thesis are discussed.

1.10.1 Energy Dispersive X-Ray Analysis (EDX)

Energy Dispersive X-Ray Analysis (EDX) also referred to as EDS or EDAX, is an x-ray technique used to identify the elemental composition of materials [129]. The EDX technique detects x-rays emitted from the sample during bombardment by an electron beam to characterize the elemental composition of the analyzed volume. Features or phases as small as 1 μm or less can be analyzed. When the sample is bombarded by the SEM's electron beam, core electrons are ejected from the atoms. The resulting electron vacancies are filled by electrons from a higher filled electronic state, and an x-ray is emitted to balance the energy difference between the two electronic states. The x-ray energy is characteristic of the element from which it was emitted. Because electrons do

not penetrate very far into a material, this method gives a surface and near surface analysis.

The EDS x-ray detector measures the relative abundance of emitted x-rays versus their energy. The detector is typically a lithium-drifted silicon, solid-state device. When an incident x-ray strikes the detector, it creates a charge pulse that is proportional to the energy of the x-ray. The charge pulse is converted to a voltage pulse (which remains proportional to the x-ray energy) by a charge-sensitive preamplifier. The signal is then sent to a multichannel analyzer where the pulses are sorted by voltage. The energy, as determined from the voltage measurement, for each incident x-ray is sent to a computer for display and further data evaluation. The spectrum of x-ray energy versus counts is evaluated to determine the elemental composition of the sampled volume [129].

1.10.2 Time-of-Flight Secondary Ion Mass Spectrometry (TOF-SIMS)

SIMS provides elemental, chemical state, and molecular information from surfaces of solid materials. In SIMS the surface of the sample is subjected to bombardment by high energy ions. This bombardment leads to the ejection (or sputtering) of both neutral and charged (+/-) species from the surface (Figure 1-14). The ejected species may include atoms, clusters of atoms and molecular fragments. A time-of-flight analyzer is used to measure the exact mass of the emitted ions and clusters. From the exact mass and intensity of the SIMS peak, the identity of an element or molecular fragments can be determined [130].

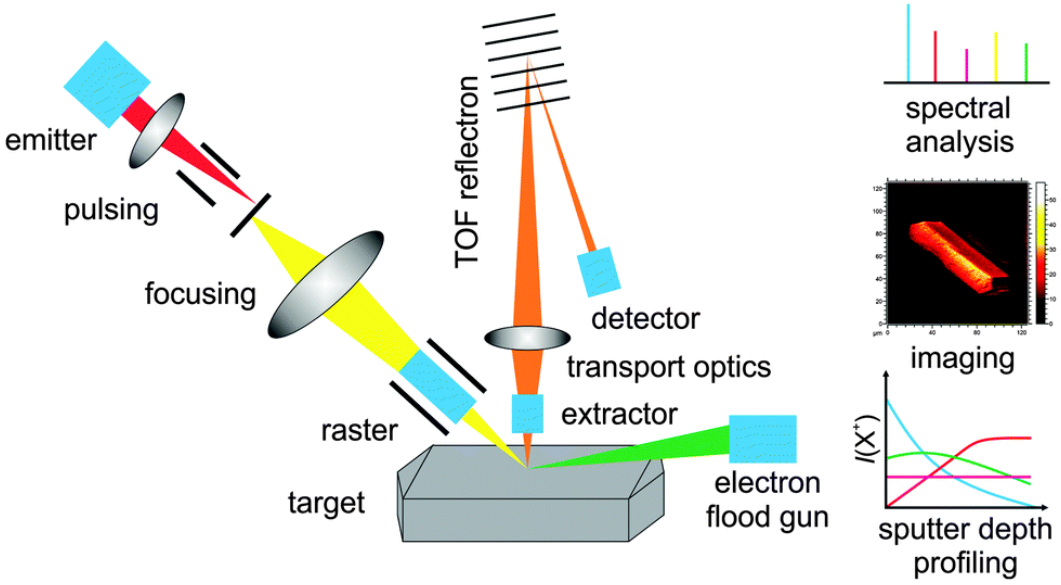

Figure 1-14. Sketch of the functional principle of a ToF-SIMS instrument and options for surface and bulk analysis of solid catalyst samples by (1) mass spectrometric analysis of surface borne secondary ions, (2) imaging of the lateral distribution of secondary ions, and (3) sputter depth profiling[130].

1.10.3 X-Ray Photoelectron Spectroscopy (XPS)

The XPS technique is used to investigate the chemistry at the surface of a sample. The basic mechanism behind an XPS instrument is illustrated in Figure 1-15 [131]. Photons of a specific energy are used to excite the electronic states of atoms on and below the surface of the sample. Electrons ejected from the surface are energy filtered via a hemispherical analyser (HSA) before the intensity for a defined energy is recorded by a detector. Since core level electrons in solid-state atoms are quantized, the resulting energy spectra exhibit resonance peaks characteristic of the electronic structure for atoms at the sample surface. While the x-rays may penetrate deep into the sample, the escape depth of the ejected electrons is limited. That is, for energies around 1400 eV, ejected

electrons from depths greater than 10 nm have a low probability of leaving the surface without undergoing an energy loss event, and therefore contribute to the background signal rather than well-defined primary photoelectric peaks [132].

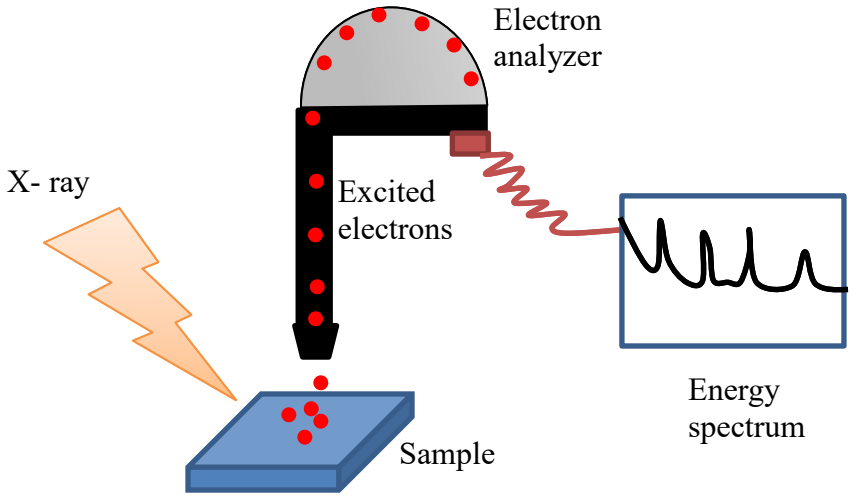

Figure 1-15. Schematic of XPS instrument.

1.10.4 Transmission electron microscope (TEM)

TEM operates on the same basic principles as the light microscope but uses electrons instead of light. The TEM uses electrons as a light source, and their much shorter wavelength gives resolution a thousand times better than with a light microscope [133]. It is possible to resolve objects to the order of a few angstroms. The possibility for high magnifications has made the TEM a valuable tool in medical, biological, and materials research. Successful sample preparation depends on the kind of sample under examination and its structural details, and the methods do not work to the same extent for all morphological types. Therefore, to perform a full structural determination it is often necessary to apply several complex sample preparation techniques [134].

1.11 Conclusion

A brief review of recent trends in protein separation, separation matrices and their applications, separation principles and fundamentals, and methods of surface characterization are presented above. In the following chapters, we will focus on the polymer entrapment technique for stabilization of CSA beds, and photografting methods to modify the surface chemistry of the beds. Characterization of the polymerization and surface modification is performed using the methods described above, and the performance of the materials for separation is examined in detail.

CHAPTER 2: ENTRAPPED SELF ASSEMBLED COLLOIDAL ARRAY NANOPARTICLE AND CHARACTERIZATION[1]

2.1 Introduction

Methods for efficient separation and purification of biomolecules are of utmost importance in diagnostics, chemical biology, proteomics, and genomics [1–3]. The dominant separation method is polyacrylamide gel electrophoresis of sodium dodecylsulphate denatured proteins (SDS-PAGE), in slab or capillary format. Numerous micro-/nanofabricated nanoporous sieving matrices have been studied as an alternative to randomly structured gels for size based separations of biomolecules [29–37]. These rigid, fabricated sieving structures have long-term stability compared to gels, which are typically prepared fresh for each analysis, and provide a means to improve the efficiency and speed of separation. Micro-/nanofabrication of sieving matrices, however, requires sophisticated, time consuming procedures, such as electron beam lithography and deep reactive ion etching, and results in two-dimensional architectures, all of which impedes their applications on a routine base. In this work, a combination of colloidal self-assembly (CSA) of particle beds, with organic polymer entrapment for stabilization and low resolution soft-lithography is employed to produce a highly efficient sieving media within the interstitial particle space. The procedure offers an alternative to polyacrylamide gels and to nanofabricated post structures, yielding a highly efficient sieving matrix for size based electrophoretic separation of proteins.

---

[1] Aversion of this chapter is in-press in *Electrophoresis*, 2016

The method of polymer entrapment of a CSA bed, characterization based on imaging/non-imaging techniques, sample injection, and sample detection optimization are discussed in this chapter.

2.2 Materials and Methods

2.2.1 Reagent and Sample

Uniform silica nanoparticles were obtained from Bangs Laboratories (Fishers, IN). Benzoin, methanol, 2-hydroxyethyl methacrylate (HEMA), and ethylene dimethacrylate (EDMA), and fluorescein dye, were purchased from Sigma-Aldrich Canada (Oakville, ON). BODIPY 493/503 (4,4-difluro-1,3,5,7,8-penta methyl-4-bora-3a,4a-diaza-s-indecene) was from Molecular Probes (Eugene, OR). (4× TBE (Trisaminomethane Borate Ethylenediaminetetraacetic acid), 0.1% w/v Sodium Dodecyl Sulfate (SDS)) was used as a running buffer and fluorescein dye was diluted with running buffer to concentration of 10^{-7} M. Deionized water with resistivity of 18 MΩ (Milli-Q UV Plus Ultra-Pure Millipore System, Milford, MA) was used to prepare all reagents and samples. Solutions were passed through a 0.22 μm pore size filter before use.

2.2.2 Microchip fabrication

Figure 2-1 shows the sketch of the polydimethylsiloxane (PDMS) microfluidic device fabricated following standard soft lithography procedures [38] to give a device with a depth of 10 μm and width of 100 μm. The sample inlet and outlet channels had an offset equal to 100 μm (a double-T injector). The buffer and injection channels were

4 mm long and the separation channel was 15 mm long. A positive photoresist master (AZ-4620, Clariant Corp., and Charlotte, NC) was UV patterned on a 4-in. silicon wafer. Negative PDMS replicas were made by pouring a 10:1 mixture of PDMS base (Sylgard 184, Dow Corning, Midland, MI) with the curing agent over the wafer, followed by curing at 60 °C overnight. PDMS replicas were removed from the master and reservoir holes were punched to access channels. All devices were assembled by sealing PDMS replicas to clean glass slides. The PDMS and glass were washed and rinsed with ethanol and double distilled water, then dried with nitrogen gas before sealing.

a) **Prepare positive mold**

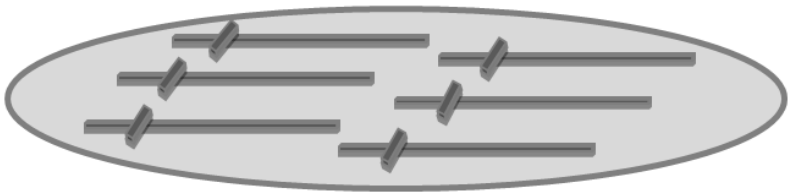

b) **Pour PDMS pre-polymer and curing at 60 °C overnight**

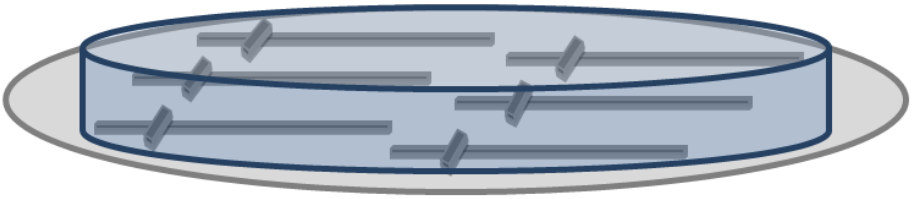

c) **Peel off the PDMS layer**

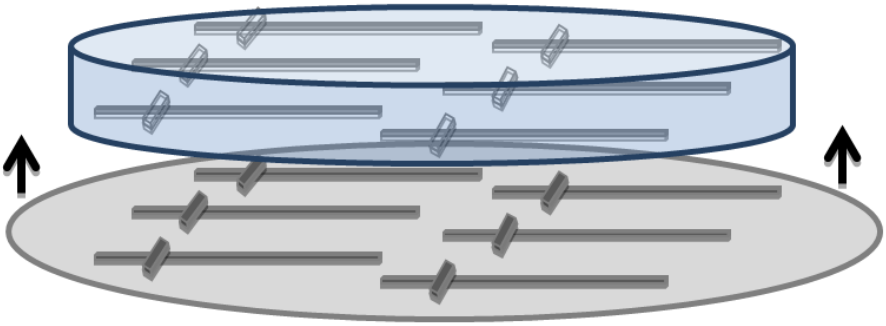

d) **Cut PDMS and Punch holes following by adhere to glass slide**

Figure 2-1. Schematic illustration of one-dimension microchip assembly.

Aqueous commercial suspensions of silica nanoparticles (Table 2-1) were ultrasonicated for 10 min prior to use, and were used without any other modification or treatment to form the on-chip colloidal self-assembly structures, following the protocol described by Zeng and Harrison [38]. A 10-15 μL colloidal suspension was injected into reservoirs 1, 2, and 3 shown in Figure 2-2. The aqueous solution fills the channels spontaneously, forming a liquid meniscus at the outlet of the channel in reservoir 4. Once all channels were filled, reservoirs 1, 2, and 3 were covered with a PDMS piece to prevent solvent evaporation. Reservoir 4 was left open so that evaporation induced colloidal growth within the channels (Figure 2-2).

Table 2-1. Particle sizes and dispersions used for packing the 1D chip.

Particle size (nm)	Dispersion (nm)
50	±10
310	±40
540	±60

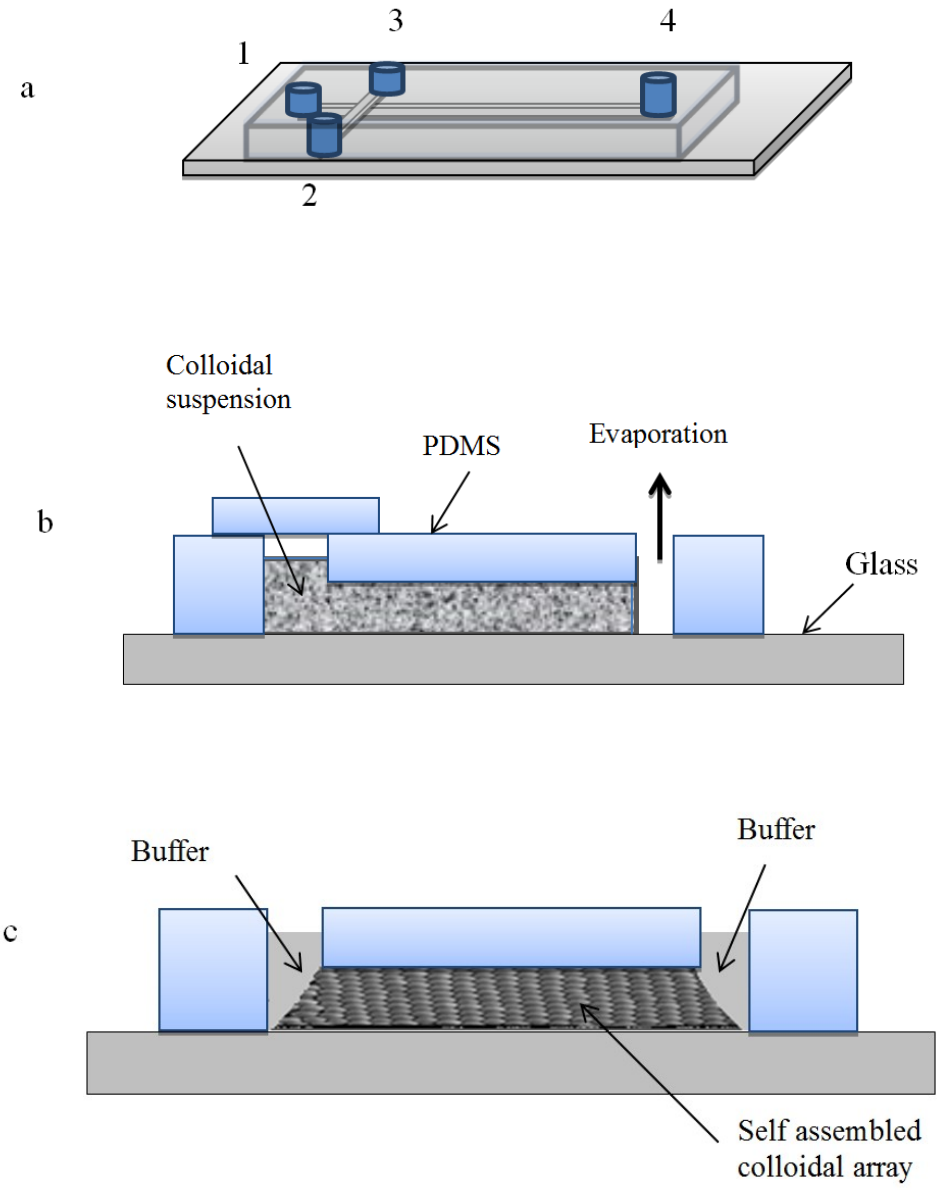

Figure 2-2. Schematic illustration of colloidal self-assembly in a one-dimensional separation microchip, a) colloidal particle suspension was injected into the reservoirs 1, 2, and 3, b) the reservoirs containing suspension were covered to prevent evaporation while reservoir 4 was left open to induce the packing while the chip was kept in a covered petri dish, c) After packing, reservoirs were filled with running buffer and the chip was used for separation. Greater wetting of glass verses PDMS gives a tail at the reservoir edge.

2.2.3 Instrumental setup

Samples were loaded from reservoir 2 by applying an electric field to reservoir 3 with other reservoirs grounded, which forming a shaped injection plug. Separation was performed under different DC electric fields with a "pull-back" voltage applied to reservoirs 2 and 3 to prevent sample leakage from the sample reservoir. A laser induced epifluorescence detection system with a 488 nm Ar^+ laser was used to monitor analyte signal 0.8 cm-1.3 cm away from the injection point. A detailed description of the detection system can be found in [135] and the setup is shown in Figure 2-3 [136].

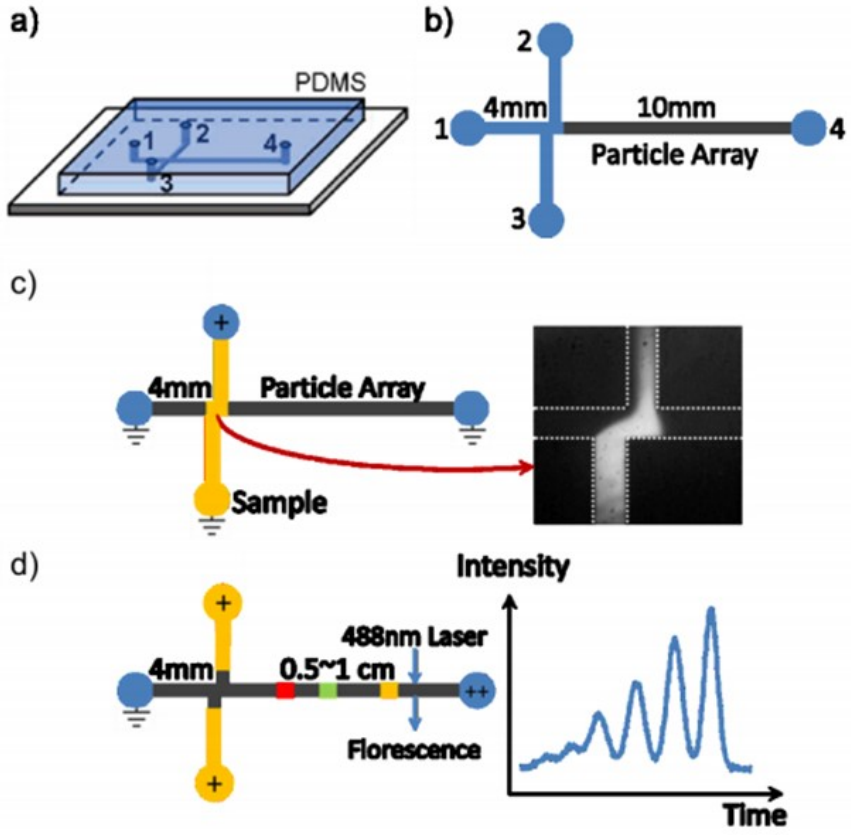

Figure 2-3. Chip structure and experimental setup. a) A PDMS chip on a glass slide. b) Chip design and reservoirs. c) Injection, the picture on the right is the fluorescent image at the crossing region. d) Separation, the right image is the intensity profile from fluorescent imaging signals [136].

Fluorescein dye, FITC (fluorescein isothiocyanate)-labeled and SDS-denatured proteins were detected using an epifluorescence microscope apparatus. The labeled proteins were excited with an expanded 488 nm argon ion laser beam. Fluorescent emissions were then collected by a 40×objective and directed, via mirrors, to a 530±30 nm band-pass filter to select excitation and detection wavelengths. After passing an 800 µm pinhole, the light intensity is detected by a photodetection device that is a photomultiplier tube (PMT). The data was collected by custom designed software using Lab view (National Instrument) and was analyzed with Origin (OriginLab Corporation). Figure 2-4 shows the experimental setup for protein detection.

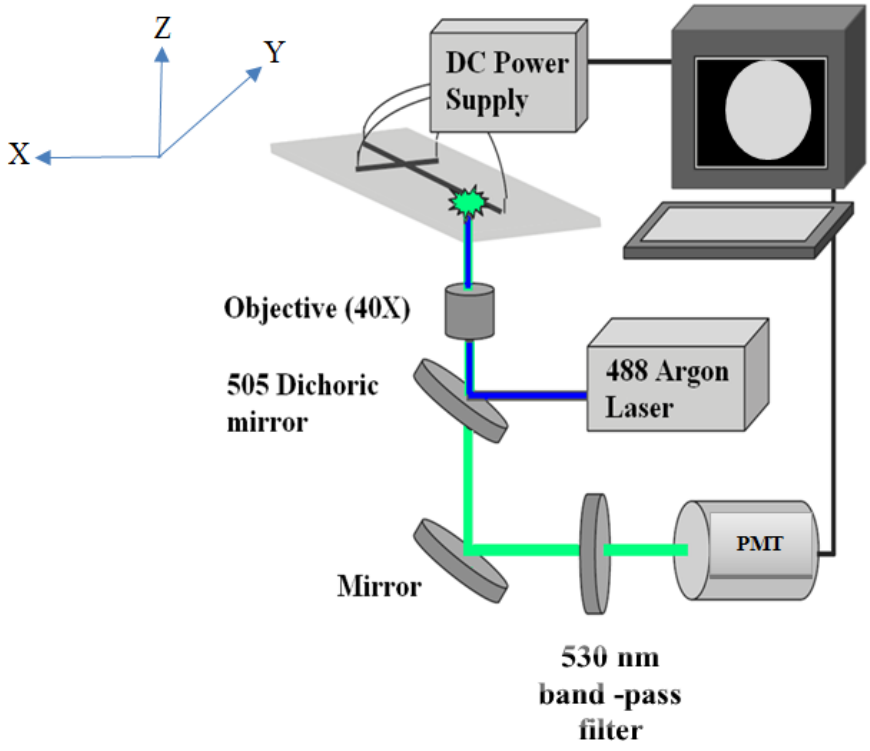

Figure 2-4. Epifluorescence microscopy setup diagram, the chip was mounted on XYZ stages.

Secondary ion mass spectrometry (SIMS) using ION-TOF IV (Ion-TOF GMBH) analysis of the CSA columns was performed at the Centre for Surface Engineering and Science (ACSES). Prior to these analyses, both native and polymer entrapped silica CSA beds were air dried, and the PDMS covers were peeled off. TOF-SIMS images were obtained using a TOF-SIMS IV instrument (ION-TOF GmbH, Germany). Bi+ ions were used as analytical source, operated at 25 kB in a static mode. The imaging areas were sputtered with O2+ ions, operated with 2 kV at different interval times.

2.2.4 Separation voltage calculation

While the voltage applied in reservoir 3 and 4 is zero (ground), voltages are applied to reservoir 1 and 2 for separating proteins. In order to calculate the electric field used for separation, calculation of the voltage at the intersection of the chip is essential.

All four channels can be modeled as a simple network of four resistors, as illustrated in Figure 2-5.

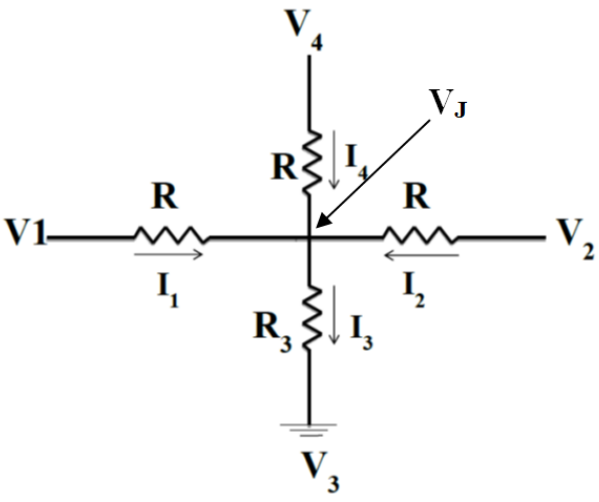

Figure 2-5. Equivalent circuit for intersection of four channels with controlled potential.

The current in each channel and the potential at the intersection are expressed using Kirchhoff's rules, such that:

$$I_3 = I_1 + I_2 + I_4 \qquad 2\text{-}1$$

$$\frac{(V_4 - V_J)}{R_4} + \frac{(V_1 - V_J)}{R_1} + \frac{(V_2 - V_J)}{R_2} = \frac{V_J}{R_3} \qquad 2\text{-}2$$

$$V_J = \frac{V_4 R_1 R_2 R_3 + V_1 R_2 R_3 R_4 + V_2 R_1 R_3 R_4}{R_2 R_3 R_4 + R_1 R_3 R_4 + R_1 R_2 R_4 + R_1 R_2 R_3} \qquad 2\text{-}3$$

In general, the potentials V_1 and V_2 can have any polarity. For this size based protein separation study V_1 was always negative and V_2 always positive. V_3 and V_4 both were zero when the voltages were applied for separation. The resistances R_1, R_2, R_3, and R_4 are proportional to the equivalent channel lengths [137].

The value of the intersection voltage V_J means that the separation voltage is about 9% less than the total applied from reservoir 1 to 4. All the separation electric fields are calculated using the intersection voltage given by equation 2-3.

2.3 Results and Discussion

2.3.1 Stabilization of the CSA structure and confinement effect

In order to entrap the CSA nanoparticles in the microchannels, monomer was introduced into the CSA beds, followed by in situ photopolymerisation. When the ratio of an open microchannel size to the pore size of a bulk porogenic polymer system is less than 5, a single polymer layer forms on the wall surface, instead of forming porous monolith columns, as can be seen in Figure 2-6 [83].

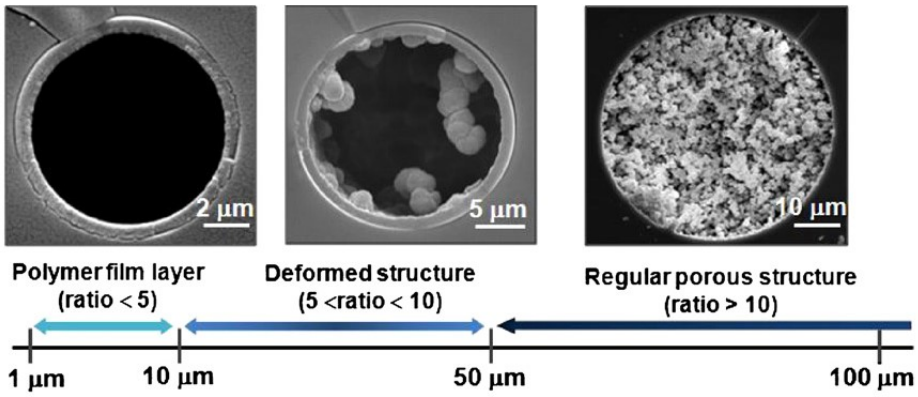

Figure 2-6. The morphological evolution of porous polymer monoliths within conduit controlled by scaling limits. As a ratio of spatial scaling to bulk monolithic pore size decreases, the material becomes more porous and sparse. At the ratio of less than 5, a uniform polymer coating with thickness in the range of hundreds of nanometers is obtained. (Reprinted from M. He et al. [83] Copyright (2012), with permission from Elsevier).

A 2-hydroxyethyl methacrylate (HEMA) monomer was employed for entrapment. This is due to its biocompatibility, and its excellent stability against hydrolysis in alkaline solution [138,139]. Figure 2-7a show the schematic procedure of the entrapment method. The monomer solution was prepared using various amounts of HEMA, along with EDMA

and the free radical photoinitiator, benzoin, and the porogenic solvent, methanol. The function of the progenic solvent is (1) to dissolve all monomers and the initiator to form a homogeneous solution and (2) to control the phase separation process during polymerization in order to achieve the desired pore structure [140]. Methanol was found to be suitable for the stabilization of the CSA bed, due to producing a large pore size polymer network [140] . An optimized monomer solution was comprised of 0.5% (v/v) of a mixture of HEMA and EDMA (30%:70%, v:v), the free radical initiator benzoin (1 wt% benzoin per weight of monomer) in 99.5% of the porogenic solvent, methanol. We used HEMA and EDMA (30%:70%, v:v) given the high reproducibility obtained with this composition ratio, as reported in previous work [138]. Other compositions tested included 0.01%, 0.05%, 5% and 10% (v/v) monomer mixture in methanol. The mixtures were purged with nitrogen for 5 min to remove dissolved oxygen prior to introduction into microchannels. In addition, free radical based polymerization in the PDMS device has been problematic due to the oxygen permeability of the PDMS substrate. To address this issue a 6 mm thick PDMS layer was used. A PDMS layer thickness ≤ 3 mm did not result in stable polymerized CSA beds. The monomer solution was then pipetted into all reservoirs and voltage was applied to the reservoirs to drive the monomer solution through the channels, with the advancement of the monomer followed by monitoring the fluorescence of BODIPY added in the monomer solution. The time and voltages needed for the monomer solution to fill all the channels were optimized for different particle sizes and are listed in Table 2-2.

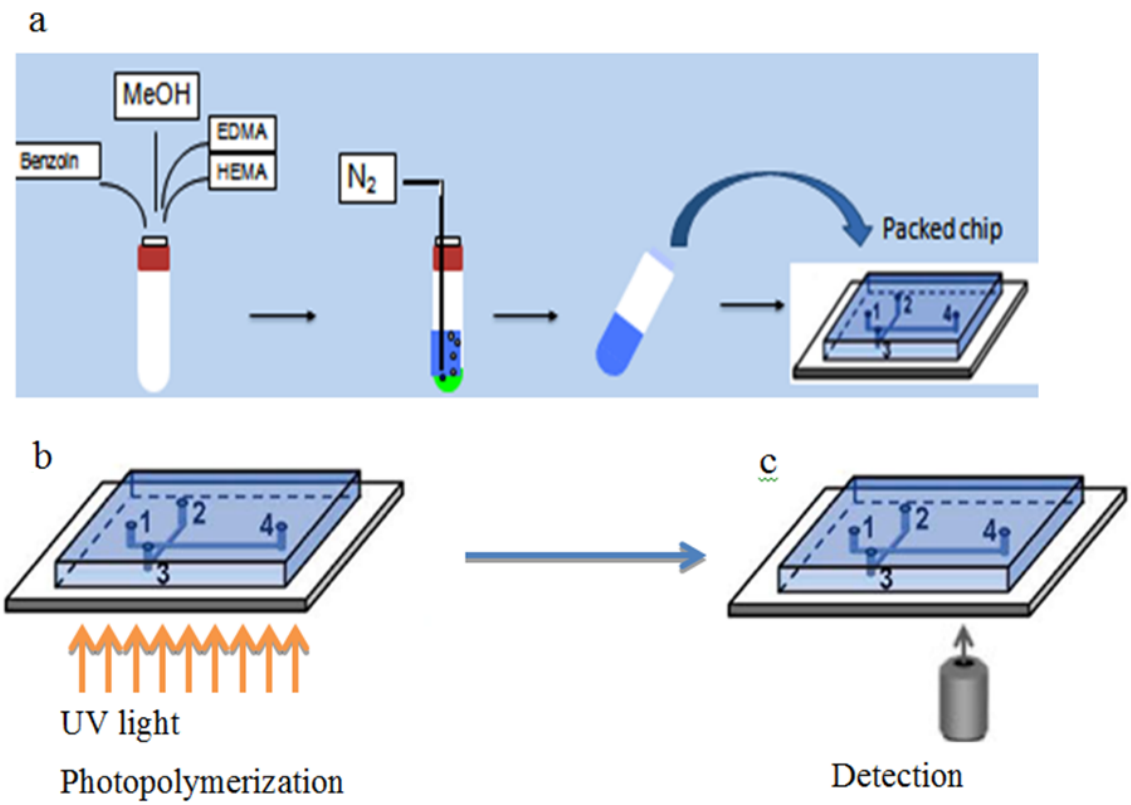

Figure 2-7. Schematic illustration of a) monomer solution preparation, b) photopolymarization, and c) detection of colloidal self-assembly silica nano-particles in one- dimensional separation microchip.

Table 2-2. Optimized voltage and time for loading the monomer solution into the microchannels.

Particle size	Voltage (V/cm)	Time (min)
690 nm	76.5	6.6
540 nm	61.5	8.2
310 nm	53.8	10.4
150 nm	23	25

Once the monomer mixture reached all reservoirs, the device was placed on a UV Transilluminator equipped with six 15-W 312-nm tubes (model TS-312R, Spectroline, Spectronics corp., Westbury, NY) for 5-30 min for photopolymerization, as shown in Figure 2-7b. The polymer entrapped particles were then flushed with methanol/water (1:1 v/v) to remove un-reacted reagents. The methanol/water mixture in the reservoirs was replaced with the running buffer and the device was left to equilibrate for 20 min prior to use. Finally, the HEMA-EDMA polymer (Figure 2-8a) [141] coated the surface of the silica particles and glued the particles in the contact point without blockage the pores (Figure 2-8b). Using these steps, pores were available for protein separation.

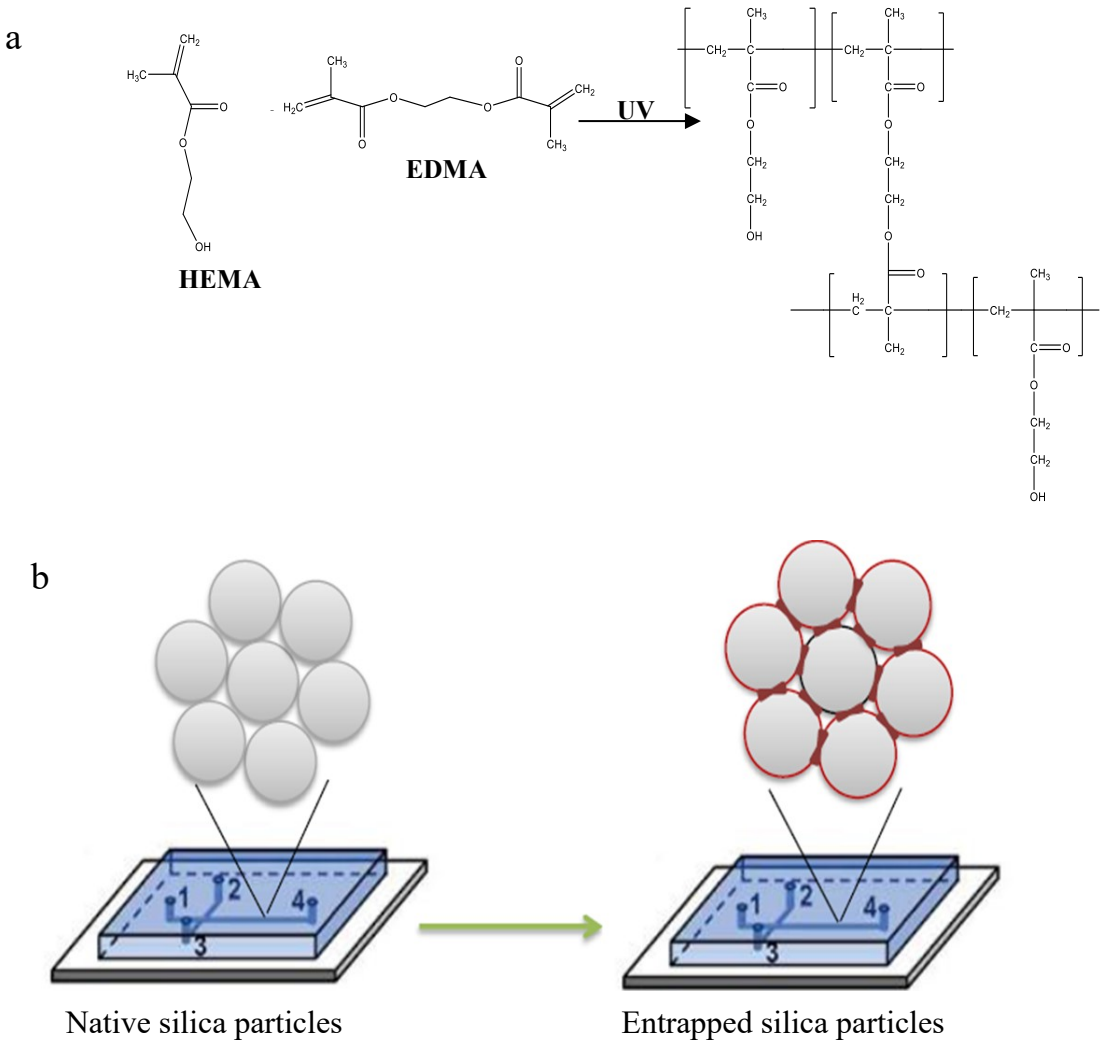

Figure 2-8. Schematic illustration of entrapment colloidal self-assembly in a one- dimension separation microchip, a) photopolymerization reaction [141], and b) native entrapped silica particles

2.3.2 Characterization of polymerization steps

2.3.2.1 Effect of monomer concentration and polymerization time

We optimized the coverage of the CSA structure with the HEMA/EDMA polymer layer within the device illustrated in Figure 2-2, by varying the concentration of monomer solution and the polymerization time. It has been shown that these two parameters are

important in fine tuning the thickness of a polymer coating for on-chip separation [83]. For a fixed amount of monomer solution, the photopolymerization time was increased from 5 to 30 min, in 5 min increments. The SEM image shown in Figure 2-9a shows that polymer "webs" form at the particle-particle contact points, holding the nanoparticles together. No obvious change is seen at the particle surface for polymerization times up to 15 min. Further increasing the polymerization time (>15 min) did not increase the stability of the bed, as characterized by the electric field. Thus, 15 min UV illumination time was used to prepare polymer entrapped, ordered, colloidal nanoparticle beds.

High resolution scanning electron microscopy (SEM) images were taken at the National Institute for Nanotechnology using a Hitachi S-5500 scanning electron microscope. Figure 2-9 shows SEM images of silica CSA beds entrapped with varying amounts of monomer. As the concentration of the monomer was increased from 0.01% to 10% (v/v) voids were observed in the ordered structure, probably due to the higher thickness of the coating on the particles that pushed them further apart. A monomer composition of less than 0.5% resulted in a polymer that formed only at the nanoparticle surfaces in the form of webbing. This polymerization glues the particles together without disturbing the ordered colloidal self-assembly, so it was used for the following experiments.

The impact of the monomer solution concentration on the crystalline structure was also studied by calculating the average orientational order parameter (ψ) from SEM images of HEMA-entrapped particles collected from different areas of the beds. The degree of order varied with the polymer concentration, as quantified by ψ, which is given by [142] as:

$$\psi = \frac{1}{N_p}\sum_{N_p}\frac{\exp(6i\beta)}{6} \qquad 2\text{-}4$$

Where N_p is the total number of particles, β is the angle between a line joining nearest neighboring particles and an arbitrary reference axis, and i is the imaginary unit. Figure 2-10 shows a plot of the average ψ as a function of the logarithm of monomer concentration. ψ approaches unity for a perfect hexagonal order and approaches zero for fully random configurations [142]. The self-assembled bed of 310 nm native silica nanoparticles is highly ordered with ψ = 0.93 and the lattice order of the beds were not disturbed with monomer concentrations of ≤ 0.5% (Figure 2-10). The pores in the lattice structure also remained open. However, when the monomer concentration was increased to 5% and 10%, the lattice structure was less ordered.

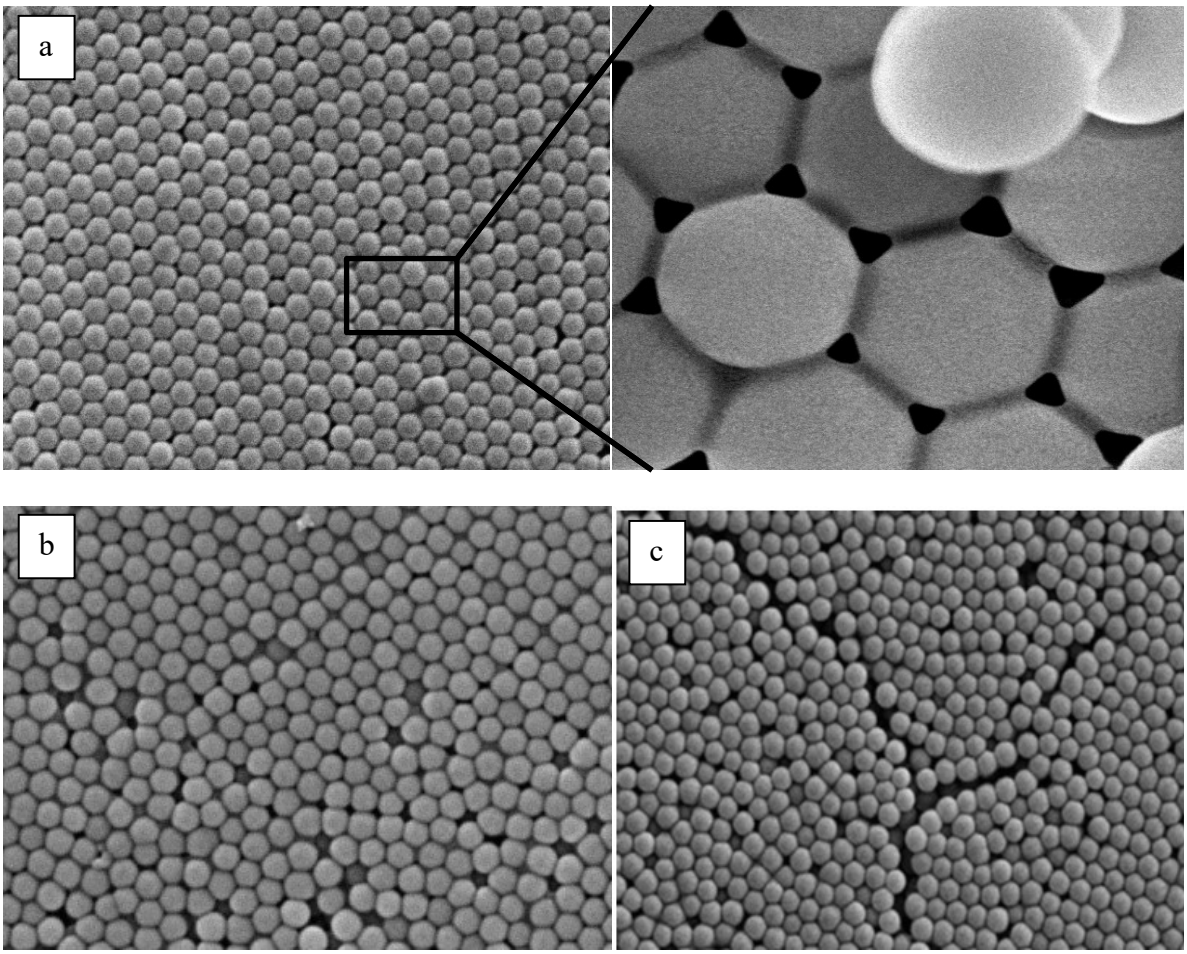

Figure 2-9. SEM images of 310 nm silica particle beds formed by colloidal self-assembly entrapped with photopolymerized methacrylates present at a) 0.5% monomer solution, b)5% monomer solution, and c) 10% monomer solution. Images were taken by peeling off the PDMS following photopolymerization.

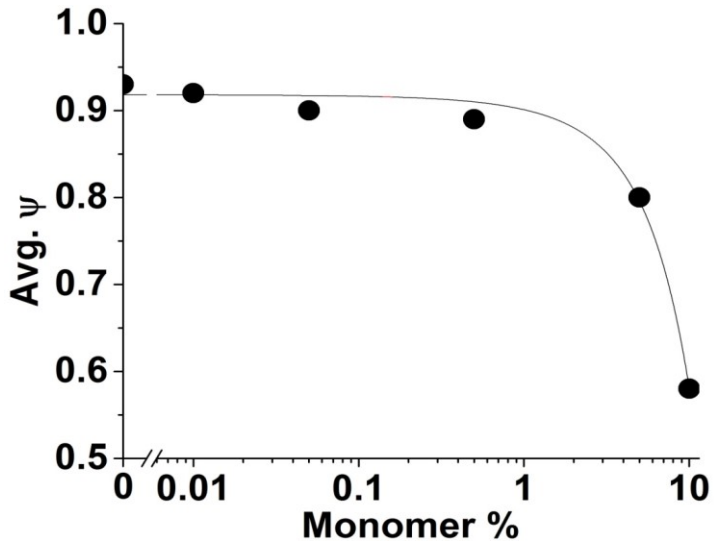

Figure 2-10. Plot of the average orientational order parameter (Ψ) observed for beds vs logarithm of monomer solution concentration% during photopolymerization, error bars were smaller than the plot symbols.

2.3.2.2 Effect of monomer concentration on electric field stability of packed beds

Figure 2-11 shows that cracks form in a nature silica bed when the electric field was raised to about 300 V/cm. Five chips were prepared and stabilized with 0.01%, 0.05%, 0.5%, and 5% of monomer solution, using the same reaction conditions. Figure 2-12 shows the effect of monomer concentration on the electric field stability of native and entrapped silica nanoparticles. Cracks formed only at much higher voltages when using polymer entrapment in the bed. It was observed that increasing the monomer concentration from 0% to 0.5% resulted in increasing the electric field stability of the bed. However, at 5% concentration the stability dropped, probably due to increased disorder in the bed encouraging its fragmentation.

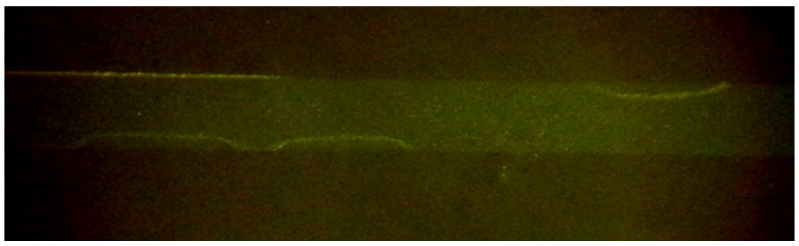

Figure 2-11. Image of cracks forming in 310nm native silica particles CSA bed in separation channel at about 320V/cm.

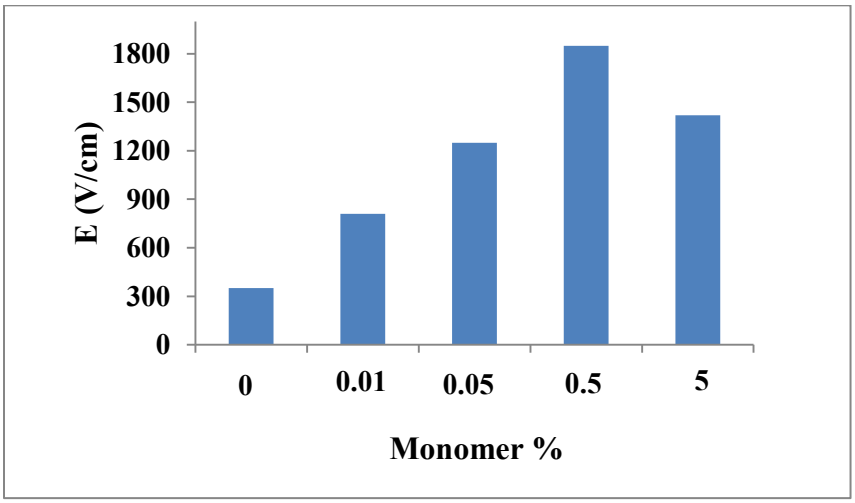

Figure 2-12. The monomer% vs. Electric field stability.

2.3.3 Characterization techniques of entrapped self-assembled colloidal array

The entrapped CSA bed was assessed based on imaging and non-imaging techniques. The imaging techniques include scanning electron microscope (SEM) imaging, energy dispersive X-Ray analysis (EDX) analysis, time-of-flight secondary ion mass spectrometry (TOF-SIMS), and transmission electron microscopy (TEM) imaging. Electroosmotic flow (EOF) measurements, joule heating measurement and florescence dye electrophoresis are non-imaging techniques that were used for characterization.

2.3.4 Imaging techniques

2.3.4.1 SEM imaging

Monodisperse suspensions of 310 nm silica particles were used to fabricate ordered packed structures inside the separation channel in the microfluidic device. The packed bed was then entrapped with photopolymerized monomer solution (0.5%). SEM images of these structures revealed homogenous, ordered, packed structures where the pore size is around 15% of the particle size, which is the radius of the narrowest tunnel surrounded by three adjacent spherical particles. For SEM observation, packed chips were dried completely and the PDMS layer was peeled off before sputtering with an Au metal layer. The bed was then coated with Au to improve the SEM resolution. It was found that the Au coating did not affect the crystalline structure of particles, based on some runs performed on high quality SEM instrumentation that do not require Au coating. Using the self-assembly approach and monodisperse particle suspensions, uniform ordered structures were fabricated. The top view and side view of the stabilized beads in a channel are shown in Figure 2-13 as an example, resembling the extreme order of micro-fabricated arrays that are made by nano-lithography.

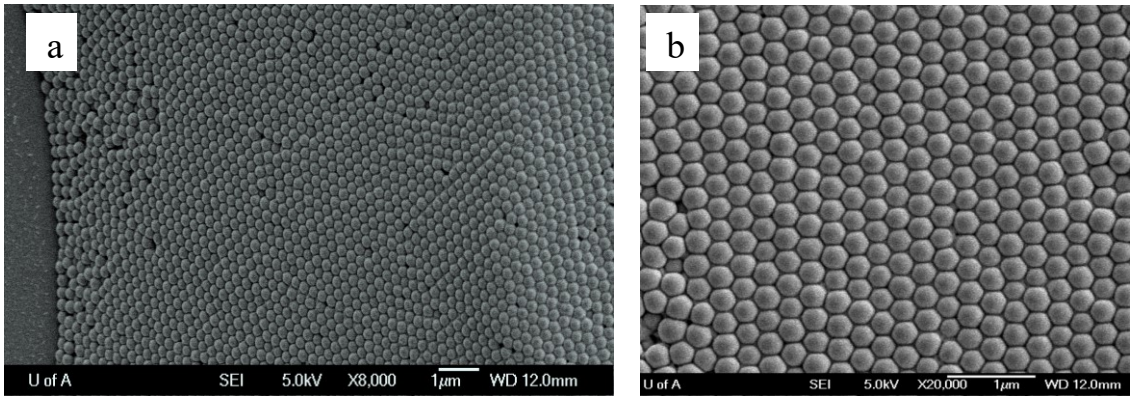

Figure 2-13. SEM images of 310 nm silica particle beds formed by colloidal self-assembly entrapped with photopolymerized methacrylate present at 0.5% monomer solution, gold coated, a) side view and b) top view.

2.3.4.2 Energy Dispersive X-ray spectroscopy (EDX) analysis

Energy Dispersive X-ray spectroscopy (EDX) is an analytical technique for elemental analysis or chemical characterization of a sample [143]. It relies on interaction of some source of X-ray excitation from a sample, and an energy analyzer. For EDXS analysis, a Zeiss EVO SEM with LaB6 electron source, equipped with a Bruker energy dispersive X-ray spectroscopy system was used. This system has a resolution of ~100 nm. Data was obtained from the CSA bed when a specific region of a channel was scanned by SEM without any sputtering with Au metal. The EDX analysis was achieved from a native silica CSA bed and an entrapped silica bed to evaluate polymerization within the CSA beds. The PDMS layer was peeled off right before analysis and the data was obtained from three different portions of the bed.

From the EDX data, the presence of carbon atoms in the polymer entrapped beds (Figure 2-14a) was observed, but not in the native silica beds (Figure 2-14b) consistent with polymerization between the nanoparticles.

a) Polymer entrapped CSA bed

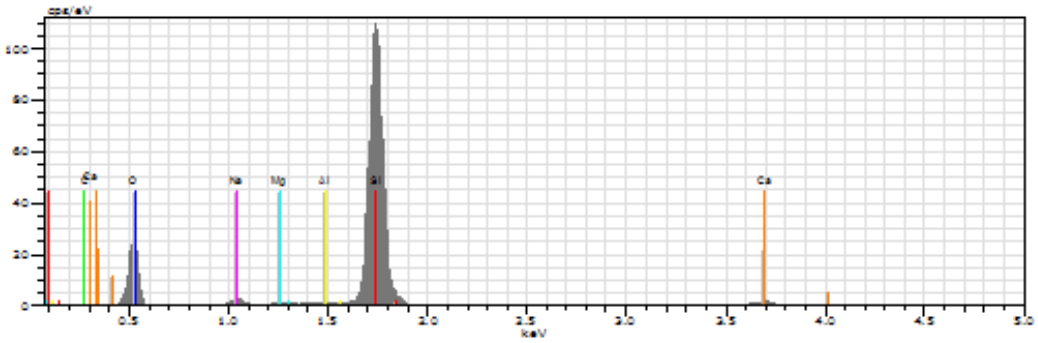

			[wt.%]	[wt.%]	[at.%]	[wt.%]
O	8	K-series	34.90	48.72	60.62	4.43
Si	14	K-series	31.08	43.39	30.76	1.38
C	6	K-series	2.23	3.12	5.16	0.73
Na	11	K-series	1.67	2.33	2.02	0.15
Ca	20	K-series	1.19	1.66	0.82	0.07
Mg	12	K-series	0.33	0.46	0.37	0.05
Al	13	K-series	0.23	0.33	0.24	0.04

Native silica CSA bed

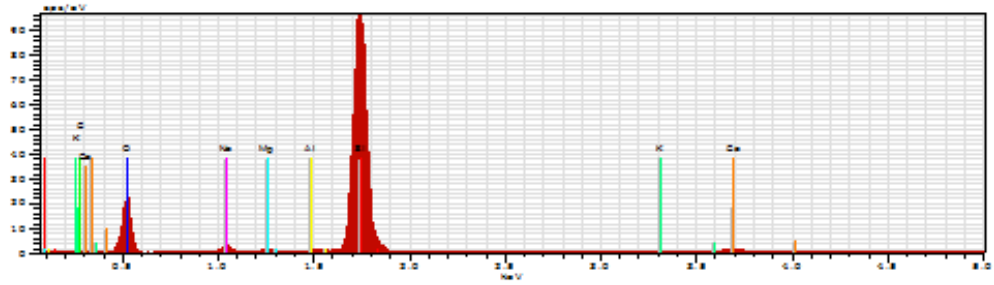

			[wt.%]	[wt.%]	[at.%]	[wt.%]
O	8	K-series	35.31	48.90	62.71	4.48
Si	14	K-series	32.07	44.42	32.46	1.43
Na	11	K-series	2.06	2.85	2.55	0.17
Ca	20	K-series	1.71	2.36	1.21	0.08
Mg	12	K-series	0.47	0.66	0.56	0.06
Al	13	K-series	0.29	0.40	0.30	0.04
K	19	K-series	0.30	0.41	0.22	0.04
C	6	K-series	0.00	0.00	0.00	0.00

Figure 2-14. Electron diffraction x-ray spectroscopy (EDXS) data of polymer entrapped on-chip CSA particles (a) and native silica on-chip CSA particles (b); particle diameter 310nm, monomer solution 0.5%

2.3.4.3 Secondary Ion Mass Spectroscopy (SIMS) analysis

TOF-SIMS is an acronym for the combination of the analytical technique SIMS (Secondary Ion Mass Spectrometry) with Time-of-Flight mass analysis (TOF), (TOF-SIMS) is a very sensitive surface analytical technique, well established for many industrial and research applications [144,145]. The technique provides detailed elemental and molecular information about the surface, thin layers, and interfaces of the sample [144]. The SIMS data indicated that the C_2H_5O functional group of HEMA is present for up to 90 min of sputtering time on HEMA entrapped particle beds. Under the SIMS conditions, the milling rate was 10 nm/min and thus a depth of 900 nm (equivalent to three particles deep) was etched, confirming that the entrapped beds are robust and deeply permeated by HEMA. In contrast, the native silica particles were removed under the milling beam within minutes, due to the accumulation of electrostatic charge overwhelming the weak adhesive forces of the native silica structure (Figure 2-15).

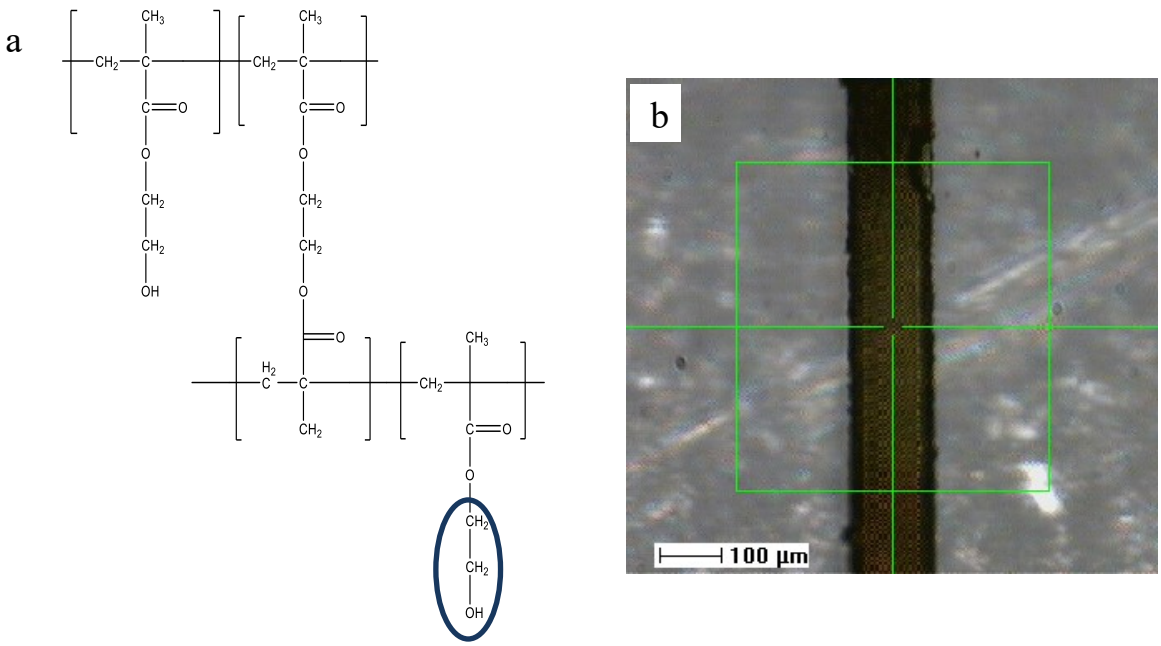

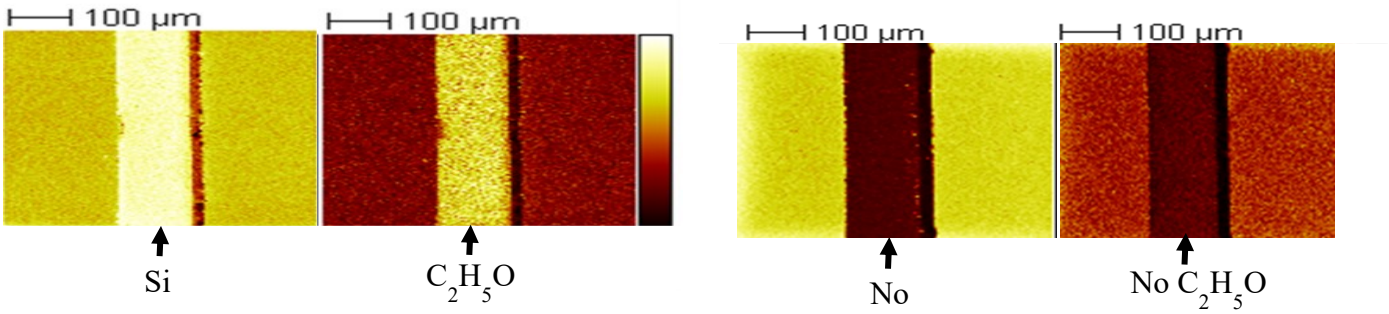

(a) Polymer entrapped CSA bed **(b) Native silica CSA bed**

Figure 2-15. a) photopolymerization network and C_2H_5O functional group, b) the analyzed area, Secondary ion microscopy (SIMS) data of (a) on-chip polymer entrapped CSA silica particles following 90 min of sputtering. Clearly Si and C_2H_5O functional groups from the entrapping polymer are visible. (b) on-chip native Si CSA particles following 30min of sputtering. The Si particles were disrupted and removed from the microchannel after 30 min of sputtering.

2.3.4.4 Transmission Electron Microscopy (TEM) analysis

A Transmission Electron Microscope (TEM) utilizes energetic electrons to provide morphologic, compositional and crystallographic information on samples [146]. TEM produces a high-resolution, black and white image from the interaction that takes place between prepared samples and energetic electrons in the vacuum chamber [147]. TEM only works with samples made thin enough to be transparent to electrons, at a distance of the order of 50-70 nm. To be able to view the native and entrapped particle bed by electron microscopy, the first stage in preparing was fixation, which is one of the most important and most critical stages. The CSA bed was air dried, the PDMS layer was peeled of and, embedded in an epoxy resin and kept in an oven for 4 hours.

After embedding the resin, block was then thin sectioned by a process known as ultramicrotomy. Sections of 50-70 nm thickness were collected on metal mesh "grids" and observed in the TEM. Sectioning the sample allows looking at cross-sections through samples to view internal (ultra)structure.

The TEM images obtained from native and entrapped silica nanoparticles shown in Figure 2-16.

The native silica nanoparticles were not stable during sectioning, and very few particles are seen. While the entrapped silica nanoparticles were stable enough to give TEM images, the sectioning process appears damage to the badly crystalline structure. As a result, we conclude the monomer solution penetrated deeply into the under layer of silica nanoparticle in the form of webbing, gluing the particles together. However, the structural damage means good quality/lattice images could not be obtained.

(a) Native silica CSA bed **(b) Polymer entrapped CSA bed**

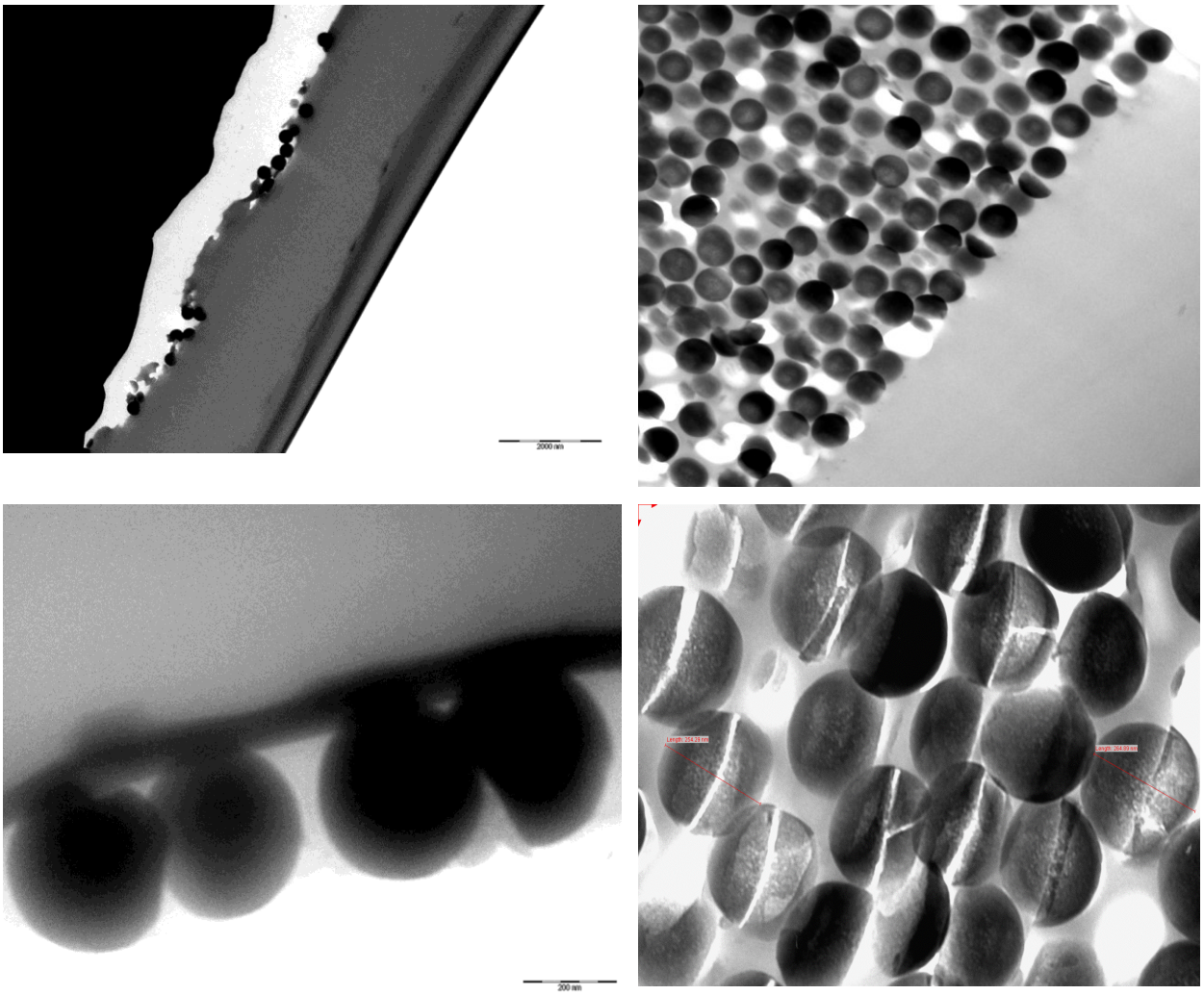

Figure 2-16. Transmission Electron Microscopy (TEM) data of (a) on-chip native Si CSA particles, 310nm, (b) on-chip polymer entrapped CSA silica particles, 0.5% monomer solution, 310nm.

2.3.5 Non-Imaging techniques

2.3.5.1 Electroosmotic flow (EOF) measurement

Electroosmotic flow (EOF) is the bulk flow of liquid in the microchannel and is a consequence of the surface charge on the silica nanoparticles [148]. The -OH groups of

silica nanoparticles can be deprotonated and cause EOF in a CSA bed. The EOF results from the effect of the applied electric field on the solution double-layer formed in solution at the surface of the particles. EOF can have numerous disadvantages with regard to analysis time, efficiency, and resolution. One way to circumvent this issue and quench the EOF in size-based separation of biopolymers is to use a high ionic strength buffer [33,34,149]. Also, EOF can be controlled by modification of the silica particle surface by means of dynamic coatings (that is, buffer additives) or by polymer coatings [150,151]. Coatings can increase, decrease, or reverse the surface charge and thus change the EOF [148,149]. The neutral hydrophilic HEMA entrapping polymer film should suppress the EOF in a CSA bed [83]. In this research EOF was measured by using migration time of a neutral dye (BODIPY) in three chips. Figure 2-17 shows a plot of electroosmotic flow mobility vs different concentrations of TBE buffer. The EOF mobility decreased along with increasing buffer concentration, because higher concentration and ionic strength confers a lower zeta potential and compresses the electrical double layer. The figure indicates that the EOF generated from polymer entrapped silica CSA beds is $\sim 2\times10^{-5}$ cm^2 v^{-1} sec^{-1} (RSD=4.1%, n=3 beds) when using 4× and 5× TBE toward cathode. This EOF is relatively small and not sufficient to maintain stable electrokinetic flow for many applications, for which $>10^{-4}$ cm^2 v^{-1} sec^{-1} is preferred. Thus, 4× TBE was used for protein separation in our systems. Figure 2-17 also shows a three times reduction in EOF when the CSA was entrapped with the polymer web compared to native beds. This is consistent with burying the charged functional groups in a polymer coating.

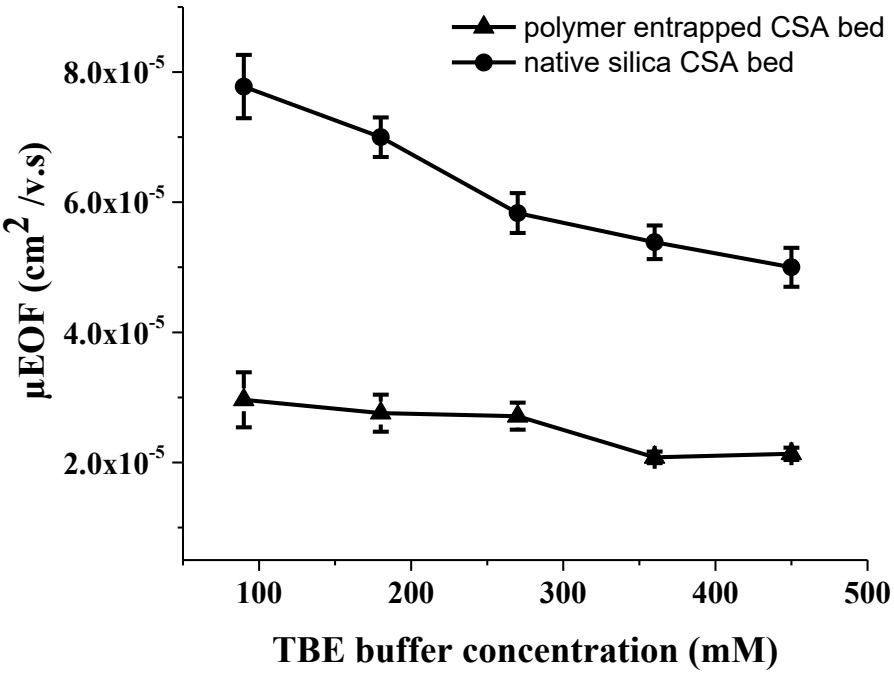

Figure 2-17. Electroosmotic flow (EOF) of polymer entrapped and native silica CSA beds as a function of buffer concentration, pH = 8.3, measured from observed mobility of BODIPY; 310nm silica particles in 10mm long bed, entrapped with photopolymerized 0.5% monomer solution, E = 100V/cm.

2.3.5.2 Joule heating measurement

The heat generated by the passage of electrical current is called Joule heat. The temperature increase depends on the power generated and is determined by conductivity of the buffer, the capillary dimensions, and the applied voltage. Significantly elevated temperatures occur when the power generation exceeds the dissipation rate [152]. The main advantage of performing electrophoresis in a narrow-bore microchannel is a reduction in the effect of Joule heating, which has traditionally limited electrophoretic techniques [153].

Heating is problematic since it can cause nonuniform temperature gradients, local changes in viscosity, and subsequent zone broadening. While the theoretical equations for efficiency and resolution advocate the use of as high an electric field as possible, Joule heating ultimately limits the benefit of this approach, regardless of capillary dimensions and temperature control.

Joule heating was measured in a single microchannel, by increasing voltage while the current was measured. The same running buffer (4×TBE) which was used for protein separation was employed here to measure for a Joule heating effect. A plot of electric field vs current shows a linear relationship for up to a tested electric field of 1,800 V/cm (Figure 2-18). This result indicates high performance can be expected in these columns without the risk of Joule heating, so no significant band broadening should arise from Joule heating effects.

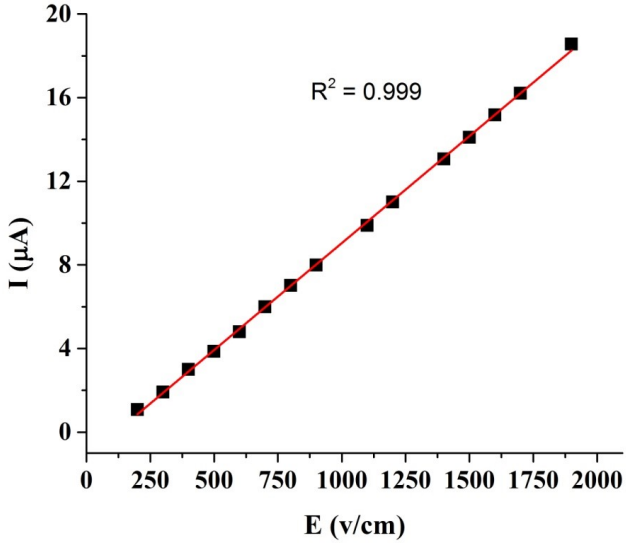

Figure 2-18. Plot of current vs electric field, with photopolymerized 0.5% monomer solution, using 4x TBE buffer (pH 8.3).

2.3.6 Characterization of injection time and separation voltage

2.3.6.1 Injection optimization

The injection system on a microfluidic chip is an important factor in the sample handling process, and its characteristics help determine the efficiency and quality of the separation. Also, a difference in conductivity of sample and running buffer can result in sample stacking or electromigration dispersion. This will affect the peak shapes and height. Therefore, the running buffer was always used to dilute the sample.

Here, the injection quality in devices entrapped with HEMA polymer and the effect of injection voltage and time were studied on a fluorescein dye peak. From the fluorescein dye peak, it was clear that the injection is indeed geometrically defined (Figure 2-19). The fluorescein dye sample was injected to the separation channel by keeping the constant field of 140 V/cm and changing the time (Figure 2-19a). Also, the dye was injected with constant time 10 sec and different voltages as can be seen in Figure 2-19b. Optimized injection time and voltage were 15 sec and 140 V/cm, respectively.

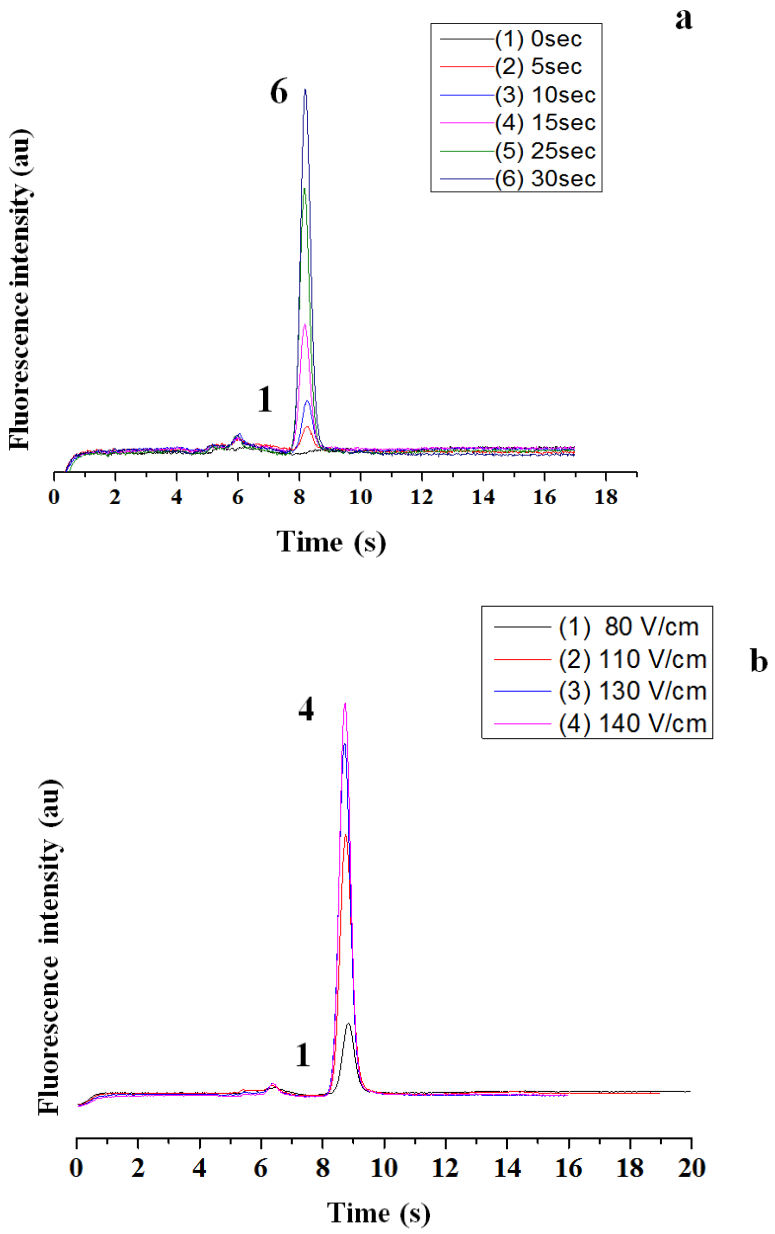

Figure 2-19. Electropherogram of fluorescein dye at different injection time and electric field, E= 1150V/cm, with a packed bed length (Ld) 5mm with photopolymerized 0.5% monomer solution, using 4×TBE buffer (pH 8.3).

The fluorescein dye peak obtained at different detection lengths along the separation channel was used to confirm that the entrapment technique is homogeneous along the microchannel. Figure 2-20a, b, and c show the fluorescein peaks at detection lengths of 5, 8, and 12 mm. It can be seen that the migration time increases as the detection length increases. The migration time increased from 8.7 sec to 20.05 sec when the detection length increased from 5 to 12 mm. A plot of detection length vs migration time is shown in Figure 2-21. The plot demonstrates a good linearity (R^2 = 0.997) between detection length and migration time. As a result, the CSA bed was stabilized along the entire bed and any desired length can be used for separation.

a

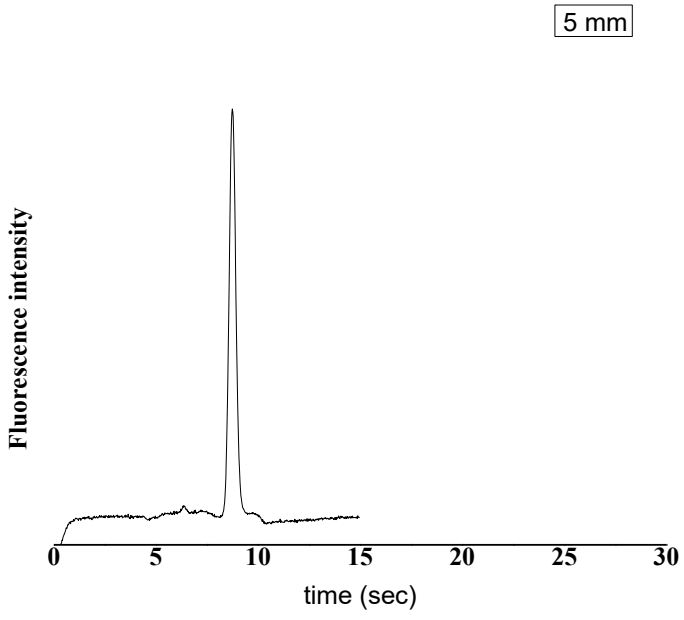

b

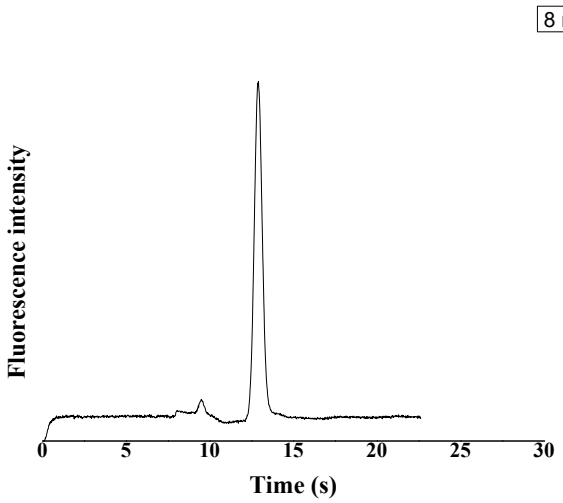

c

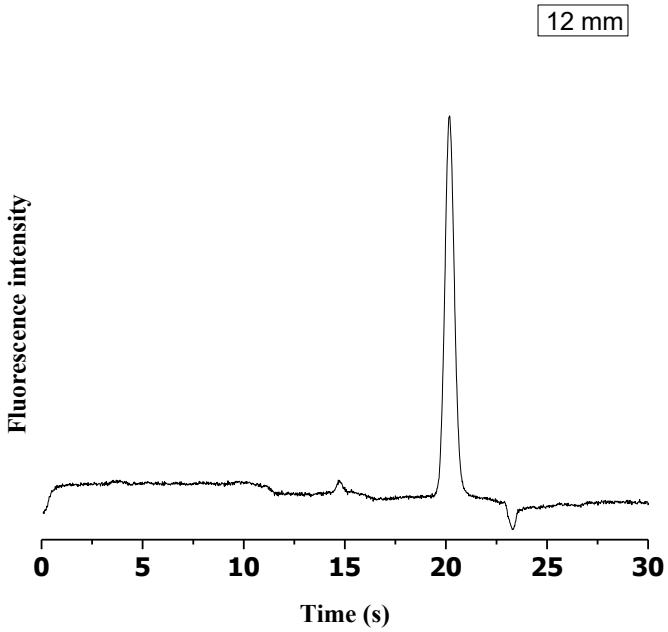

Figure 2-20. Electropherogram of fluorescein dye at E= 1095 V/cm, with a packed bed length (Ld) of a) 5, b) 8, and c)12mm with photopolymerized 0.5% monomer solution, using 4× TBE buffer (pH 8.3).

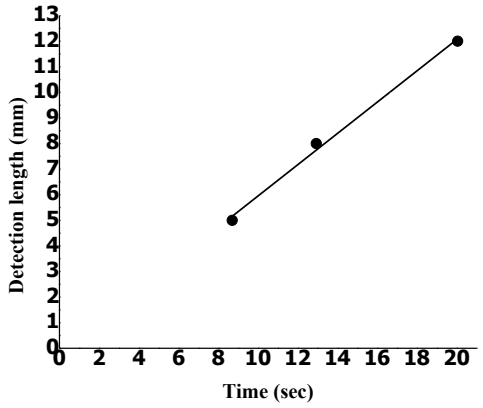

Figure 2-21. Plot of detection length vs migration time for fluorescein dye device used: R^2=0.9919 310 nm silica particle CSA in 18mm long bed entrapped with photopolymerized 0.5% monomer solution, using 4× TBE buffer (pH 8.3).

Figure 2-22 shows electropherograms of fluorescein dye at a detection length (Ld) of 13 mm, using different electric field strengths. The fluorescein dye peaks became sharper as the electric field increased, because there was less time to diffuse and the migration time decreased. The figure also shows that the polymer entrapped column can withstand electric fields up to 1,800V/cm, which is significantly high compare to native silica beds with no entrapment, for which ~320 V/cm is the limit.

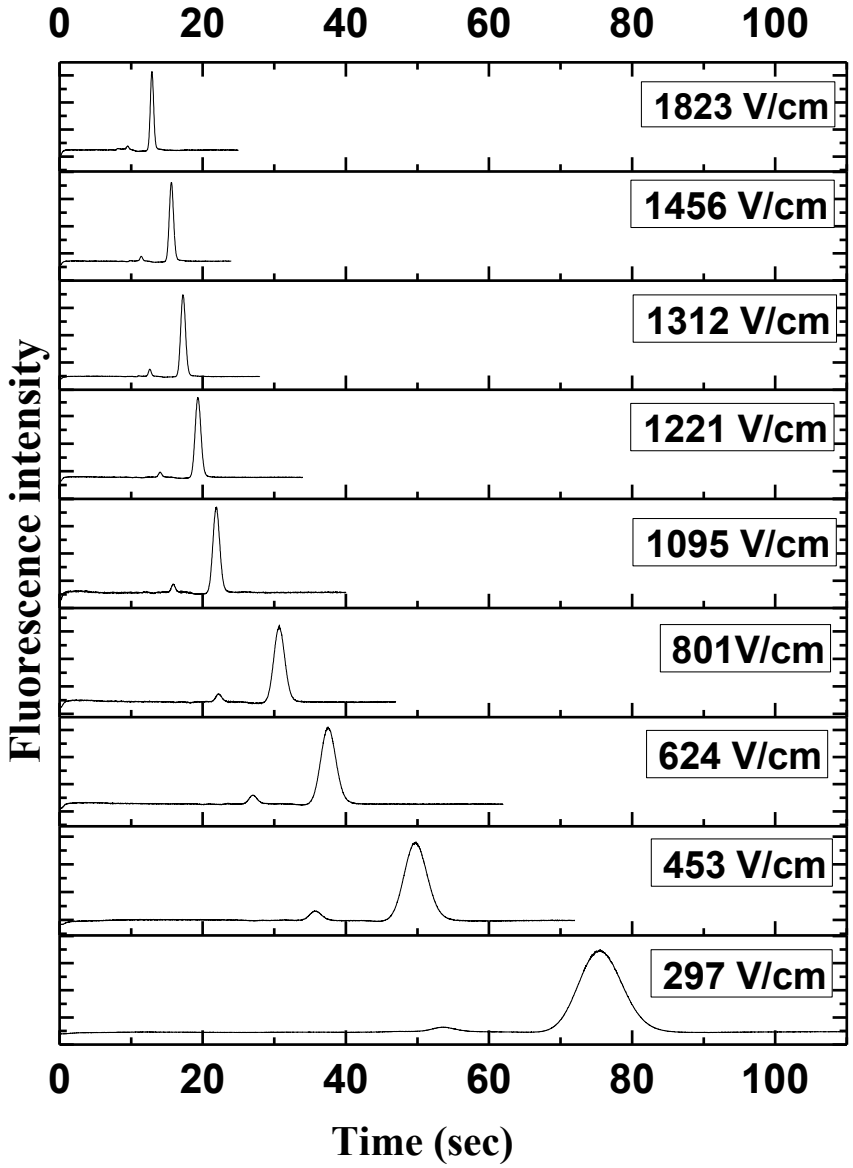

Figure 2-22. Electropherogram of fluorescein dye at increasing field strength, 310nm silica particle CSA in 18mm long bed entrapped with photopolymerized 0.5% monomer solution, using 4× TBE buffer (pH 8.3), (Ld) of 13 mm.

Figure 2-23 illustrates the apparent mobility obtained for fluorescein dye at a separation length (L_d) of 13 mm, using different electric field strengths. The apparent mobility is constant in an elevated electric field, which confirms that the bed was stable and useful at high voltages up to 1800V/cm.

Also the %RSD was 0.4% for the fluorescein migration times calculated from five replicate runs at E= 956 V/cm and detection length (L_d) of 5 mm, as shown in Figure 2-24. This RSD shows the entrapped bed has good reproducibility for the next step in our study, which is protein separation.

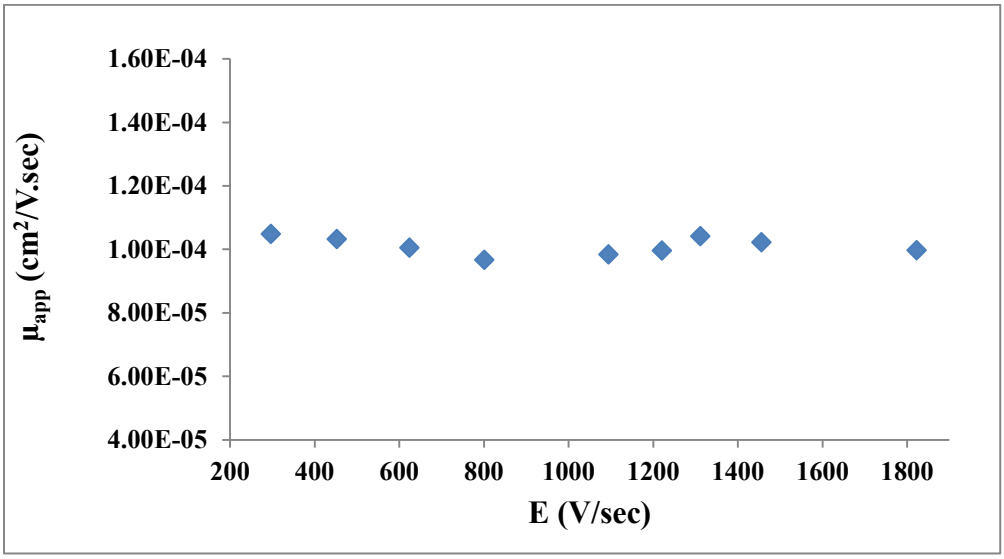

Figure 2-23. Plot of apparent mobility (μ_{app}) vs electric field for fluorescein dye device used: 310nm silica particles CSA in 13mm long bed entrapped with photopolymerized 0.5% monomer solution, using 4× TBE buffer (pH 8.3).

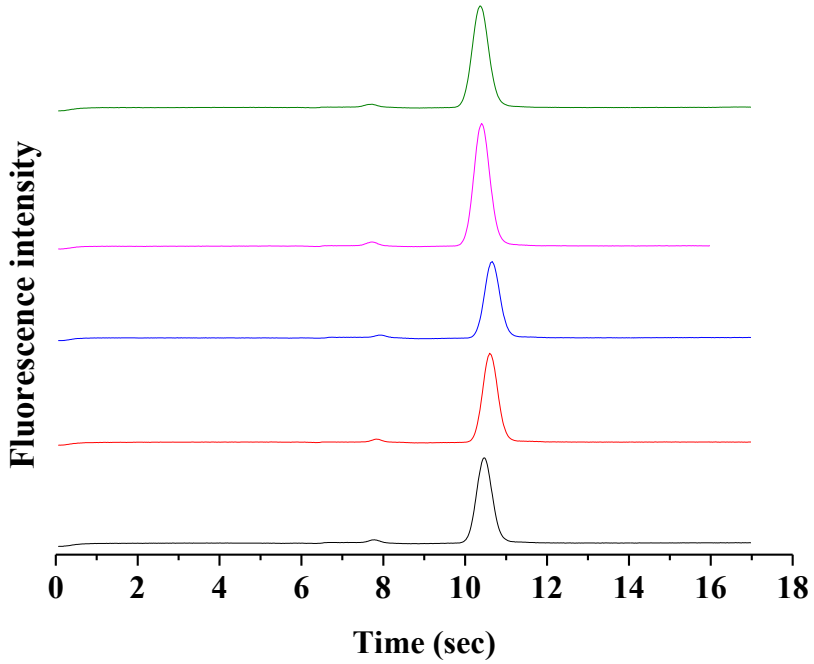

Figure 2-24. Reproducibility of fluorescein dye peak at multiple run, E= 956V/cm, with a packed bed length (Ld) 5mm with photopolymerized 0.5% monomer solution, using 4× TBE buffer (pH 8.3)

2.4 Conclusion

The CSA bed was stabilized using photopolymerization of methacrylates and the entrapped bed was assessed with different techniques of imaging and non-imaging. The results show that the entrapment of CSA silica nanoparticles in microfluidic devices results in a highly stable crystalline structure. These structures are fused together with minimal amounts of organic polymer in a web-like formation. Photopolymerization of methacrylates is a rapid, facile fabrication method for the stabilization of sub-micron scale CSA particle beds, retaining a high degree of order and packing quality upon polymerization. This polymer entrapment technique improved the stability of the CSA structure at high electric fields (up to at least 1,800 V/cm) allowing fast and highly efficient separation performance.

CHAPTER 3: ENTRAPPED SELF – ASSEMBLED COLLOIDAL ARRAY NANOPARTICLE FOR SIZE BASED PROTEIN SEPARATION[2]

3.1 Introduction

Sodium dodecyl sulfate-polyacrylamide gel electrophoresis (SDS-PAGE) has traditionally been used as the primary method for size-based protein separations under denaturing conditions [66]. SDS binds to polypeptide chains (1.4 g of SDS/1 g of protein), resulting in similar charge densities and constant mass-to-charge ratios. Hence, an electrophoretic separation of these SDS-protein complexes can be achieved in a sieving medium based on the size [154,155].

In this chapter, we focus on the performance of polymer entrapped, ordered, colloidal nanoparticle beds as a sieving medium for purpose of size based protein separation. The effect of electric field, particle size, detection length, and mass resolution are discussed. High molecular weight separation, molecular weight determination and reproducibility of entrapped CSA bed are also explained.

[2] A version of this chapter is in-press in *Electrophoresis*, 2016.

3.2 Materials and methods

3.2.1 Reagents

Uniform silica nanoparticles 310 and 540 nm in diameter were obtained from Bangs Laboratories (Fishers, IN). Benzoin, methanol, 2-hydroxyethyl methacrylate (HEMA), and ethylene dimethacrylate (EDMA), aprotinin (6.5 kDa), ribonuclease A (13.7 kDa), lysozyme (14 kDa), trypsin inhibitor (soybean, 20.1 kDa), ovalbumin (chicken egg, 45 kDa), and bovine serum albumin (BSA) (66 kDa) were purchased from Sigma-Aldrich Canada (Oakville, ON). (4× Tris ((hydroxymethyl)aminomethane), Borate, EDTA (Ethylenediaminetetraacetic acid) (TBE), 0.1% w/v SDS), pH 8.3, used as a running buffer. Deionized water with a resistivity of 18 MΩ (Milli-Q UV Plus Ultra-Pure Millipore System, Milford, MA) was used to prepare all reagents and samples. Solutions were passed through a 0.22 μm pore size filter before use. BODIPY 493/503 (4,4-difluro-1,3,5,7,8-penta methyl-4-bora-3a,4a-diaza-s-indecene) was from Molecular Probes (Eugene, OR).

3.2.2 Sample preparation

All proteins (Table 3-1) were individually conjugated with fluorescein isothiocyanate (FITC) following the Sigma-Aldrich labelling protocol [156,157]. A solution of at least 2 mg/ml of protein in 0.1 M sodium carbonate buffer, pH 9 was prepared. For each 1 ml of protein solution 50 μl of FITC solution (dissolved 1 mg in 1 ml DMSO) was added very slowly, in 5 ml aliquots, while gently and continuously the stirring protein solution. After all the required amount of FITC solution was added, the solutions were

incubated in the dark for 8 hours at 4 °C. The labelled proteins were passed through a Sephadex G25 column to remove the free FITC. The filtered FITC-labelled protein solutions were stored in the dark at -20 °C until use.

In order to denature the proteins, aliquots of FITC-labelled protein solutions were mixed with the same volume of buffer (4× TBE buffer, 4% w/v SDS, 8% v/v 2-mercaptoethanol), then incubated at 85 °C for 5 min. Before separation, denatured proteins were diluted with running buffer (4× TBE, 0.1% w/v SDS) to a final concentration of 10^{-8}-10^{-7} M. Deionized water having a resistivity of 18 MΩ (Milli-Q UV Plus Ultra-Pure Millipore System, Milford, MA) was used to prepare all reagents and samples. Solutions were passed through a 0.22 μm pore size filter before use.

Table 3-1. Proteins and their molecular weights used for separation.

Protein	Molecular weight (kDa)
Aprotinin	6.5
Ribonuclease A	13.7
Lysozyme	14
Trypsin Inhibitor	20
Ovalbumin	45
BSA	67
ß-galactosidase	116
Myosin	223
Thyroglobulin	330, 660

3.2.3 Stabilization of the CSA structure

Briefly, an optimized monomer solution was comprised of 0.5% (v/v) of a mixture of HEMA and EDMA (30%:70%, v:v) the free radical initiator benzoin (1 wt% benzoin per weight of monomer) in 99.5% of the porogenic solvent, methanol. More details have been discussed in section 2.3.1. Other compositions tested included 0.01%, 0.05%, 5% and 10% (v/v) monomer mixture in methanol. The device was photopolymerized with a UV lamp. The polymer entrapped particles were then flushed with methanol/water (1:1 v/v) to remove un-reacted reagents. Finally, the methanol/water mixture in the reservoirs was replaced with the running buffer and the device was left to equilibrate for 20 min prior to use.

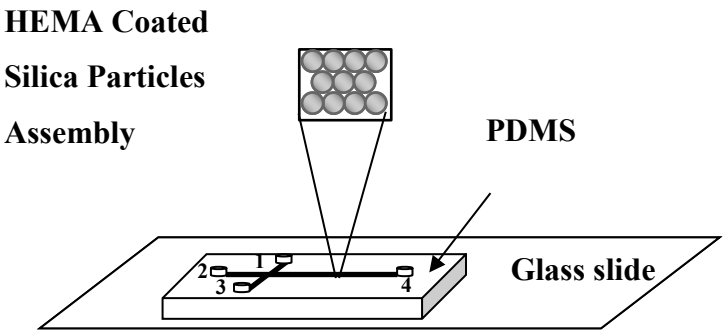

Figure 3-1. Schematic of the microfluidic chip with double T-injector for one-dimensional separation, utilizing a porous separation media formed by colloidal self-assembly of 310 nm diameter silica particles. Channels are 10 µm deep and 100 µm wide, in PDMS, mounted on a glass microscope slide.

3.2.4 Separation and fluorescence detection

4×TBE buffer (pH 8.3), with 0.1% v/v SDS, was used as a running buffer. The running buffer was always used to dilute the sample to prevent electromigration dispersion. The polymer entrapped CSA beds were first equilibrated by applying 100 V/cm until the current through the channels became static. A schematic of the microfluidic chip is shown in Figure 3-1. Samples were loaded from reservoir 2 by applying an electric field of 180 V/cm for 30 s to reservoir 3, with other reservoirs grounded to form a shaped injection plug. Separation was performed under different electric fields with a "pull-back" voltage applied to reservoirs 2 and 3 to prevent sample leakage from the sample reservoir. A previously (section 2.2.3) described laser induced epifluorescence detection system with a 488 nm Ar+ laser [158] was used to monitor analyte signal 0.8 cm - 1.3 cm away from the injection point.

3.3 Results and Discussion

The polymer entrapped CSA bed was evaluated in terms of plate height (H) vs migration rate of trypsin inhibitor, by varying the applied electric field. The protein peaks narrowed quickly as E was increased (Figure 3-2a). The small peak migrating prior to trypsin inhibitor is an impurity. A plot of the migration rates of the protein as a function of applied electric field showed a linear relationship (Figure 3-2b). Figure 3-2c shows a plot of plate height vs analyte migration rate, after subtracting the band broadening contribution from the injector [159]. Data was fitted to the classical Van Deemter equation (equation 3-1).

$$H = A + \frac{B}{U} + CU \qquad 3\text{-}1$$

where A depends on the quality of the column packing, B accounts for longitudinal diffusion, and C expresses the effect of mass-transfer resistance in both the stagnant and stationary phases. The *H–U* curve therefore features a minimum, corresponding to the optimum plate height.

The most significant component is the inverse dependence on velocity, indicating diffusion driven dispersion is dominant. A minimum value of H is seen at ~ 0.3 mm/s migration rate, which corresponds to 670 V/cm. This point was taken as the starting point for high performance separation, yielding H ~200 nm (5 x 10^6 plates/m) for trypsin inhibitor. When data points corresponding to migration rates of 0.087 to 0.425 mm/s were fitted to a B/Ucurve, it gave 0.106/υ with an R^2 = 0.96, where U is the analyte migration rate. At the highest fields evaluated (>1,600 v/cm), H increases with field and migration rate. This effect may arise from Joule heating, although the data in Figure 3-2a and the current plot indicate the thermal contribution to dispersion is very minor. Resistance to mass transfer, arising from non-specific adsorption induced band broadening, offers a more likely explanation for the linear rise in plate height at higher migration rates. A fit to the classical Van Deemter equation [160] is not ideal, even with the highest migration rate data omitted from the fit, but the results show an electric field dependence similar to that reported in the literature [42,93,161,162].

A fit of equation 3-1 up to 0.425 mm/s gives a value for the A term that is nearly zero and a negligible value for C. However, a fit to the full data set gives a negative value

for A and a value for C of 0.83. This behavior has been reported previously, but not discussed in detail [42]. It implies a CU term in which C has an onset velocity.

When the colloids are not close-packed (i.e., if there is a crack), then the proteins tends to migrate along the crack rather than through the interior of the crystal [38–40,163]. This destroys the separation as it introduces significant radial heterogeneity in the mobility, creating catastrophic band broadening as well as providing a sieve-free path. On the other hand lattice defects and structural disorder cause band broadening, and contribute to the terms in the Van Deemter equation.

(a)

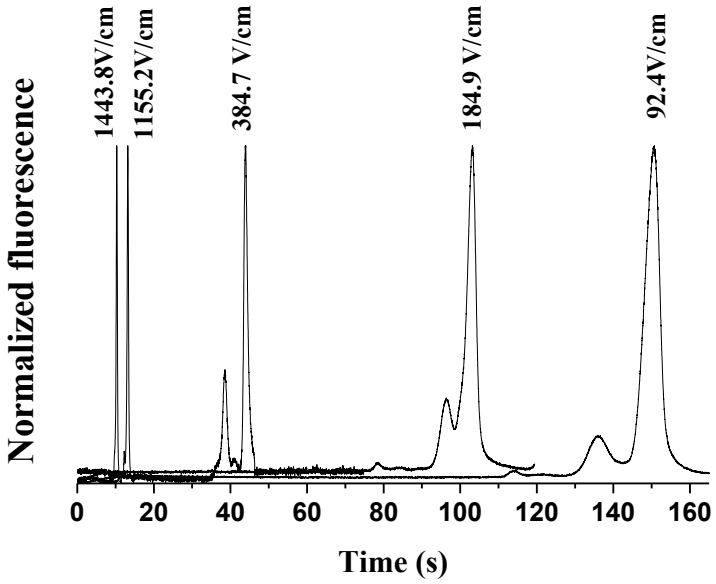
Normalized fluorescence
1443.8V/cm
1155.2V/cm
384.7 V/cm
184.9 V/cm
92.4V/cm
0
20
40
60
80
100
120
140
160
Time (s)

(b)

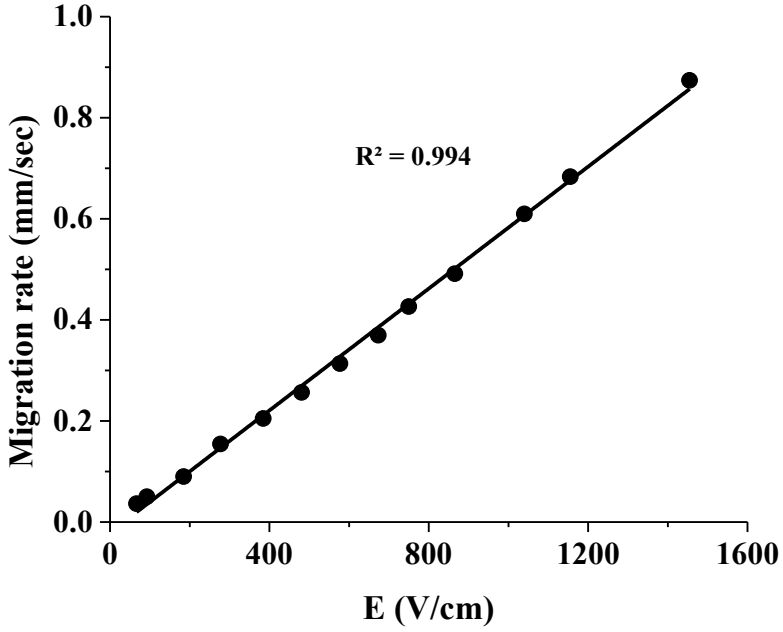
Migration rate (mm/sec)
1.0
0.8
0.6
0.4
0.2
0.0
R² = 0.994
0
400
800
1200
1600
E (V/cm)

(c)

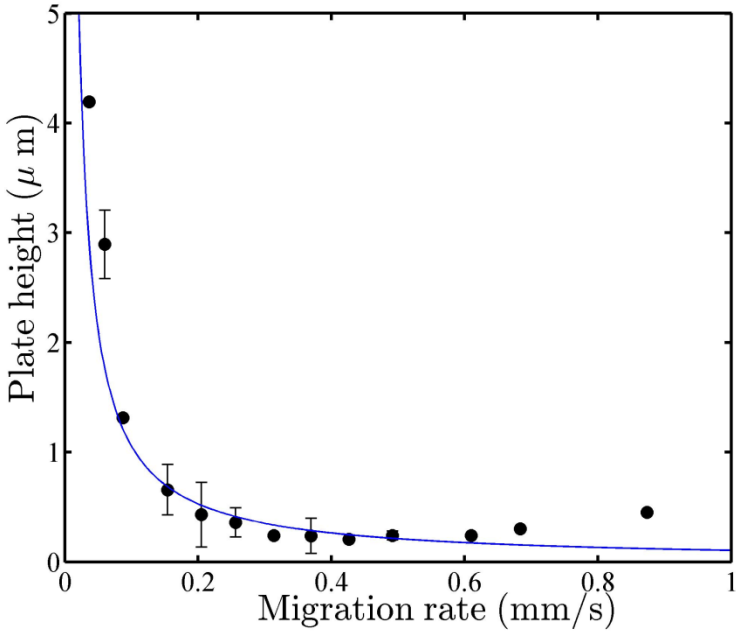

Figure 3-2. a) Migration rate (u) of trypsin inhibitor vs electric field, packed bed length (Ld) = 9 mm. b) Electropherogram of trypsin inhibitor at electric fields of 110, 220, 440, 1330, and 1600 v/cm, L_d = 9 mm. The small peak eluted before trypsin inhibitor is an impurity peak. c) Plot of plate height vs trypsin inhibitor migration rate (●) fitted to a B/u curve (solid line) resulted in a B value of 0.106, R^2 = 0.96 fit to data from υ = 0.087 to 0.425 mm/s.

3.3.1 Effect of electric field on separation

Figure 3-3 shows electropherograms of a mixture of four FITC-labeled SDS denatured proteins: aprotinin (MW 6.5 kDa), trypsin inhibitor (MW 20.1 kDa), ovalbumin (MW 45 kDa), and bovine serum albumin (BSA) (MW 66 kDa) detected at a separation length (Ld) of 13 mm, using different electric field strengths (345, 488, 963, 1081, 1199, and 1436 V/cm). The four proteins migrate through from the 310 nm CSA

bed with a migration time that increases with molecular weight; aprotinin was detected first and BSA was detected last, as determined by injecting each protein separately.

Baseline separation of all species was accomplished, as shown in Figure 3-3. As the electric field increased, the peaks were sharper, and the separation time decreased to 32 s, while the resolution improved. Figure 3-3 shows that the polymer entrapped column can withstand electric fields up to 1,450 V/cm, which is significant compared to native 310 nm silica particle beds with no entrapment, for which ~300 V/cm is the limit before the bed is disassembled.

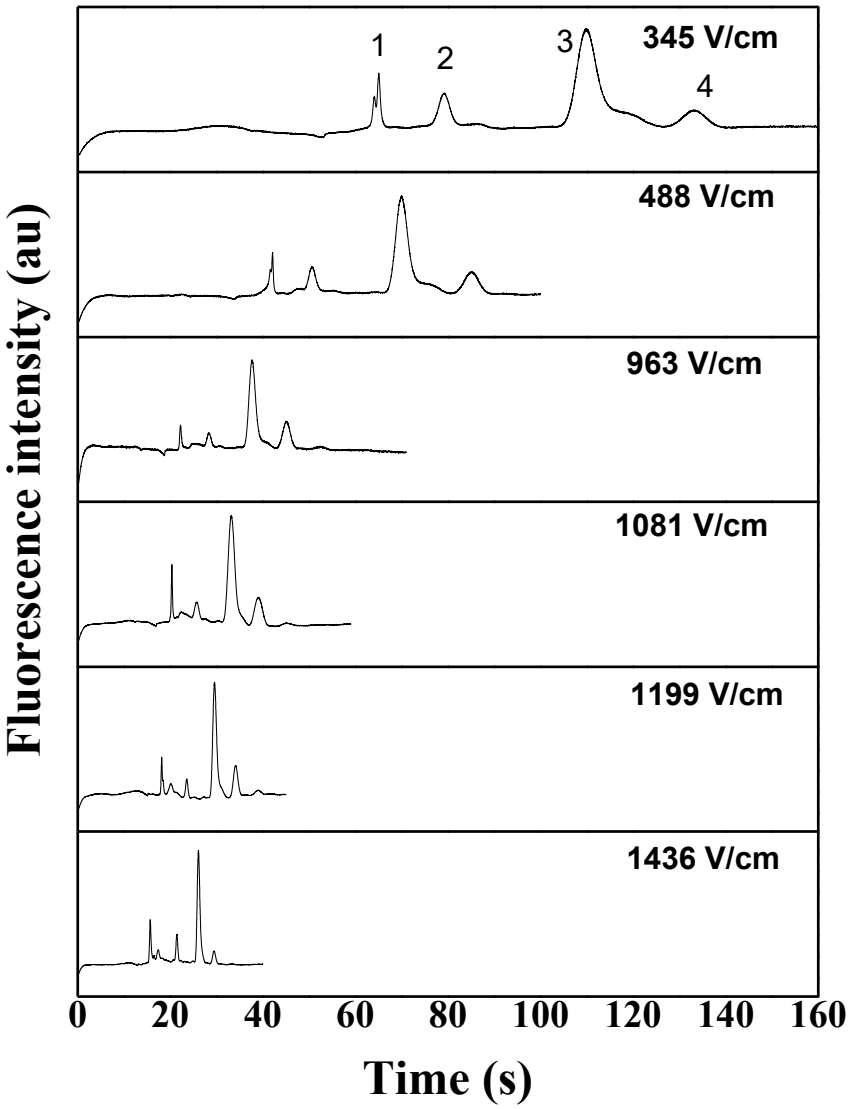

Figure 3-3. Electropherogram of (a) 1-aprotinin (6.5 kDa), 2-trypsin Inhibitor (20 kDa), 3-ovalbumin (45 kDa), and 4-BSA (66 kDa) at increasing field strength, with a packed bed length (L_d) of 13 mm.

The resolution between aprotinin (6.5 kDa) and trypsin inhibitor (20 kDa) improved two times when the voltage increased about four times, consistent with the equation 1-15.

Figure 3-4 shows apparent mobility (μ_{app}) vs electric field intensity for aprotinin (6.5 kDa), trypsin inhibitor (20 kDa), ovalbumin (45 kDa), and bovine serum albumin (BSA, 67 kDa). The apparent mobility is constant at elevated electric field for four proteins, which confirms that the CSA bed was stabilized properly.

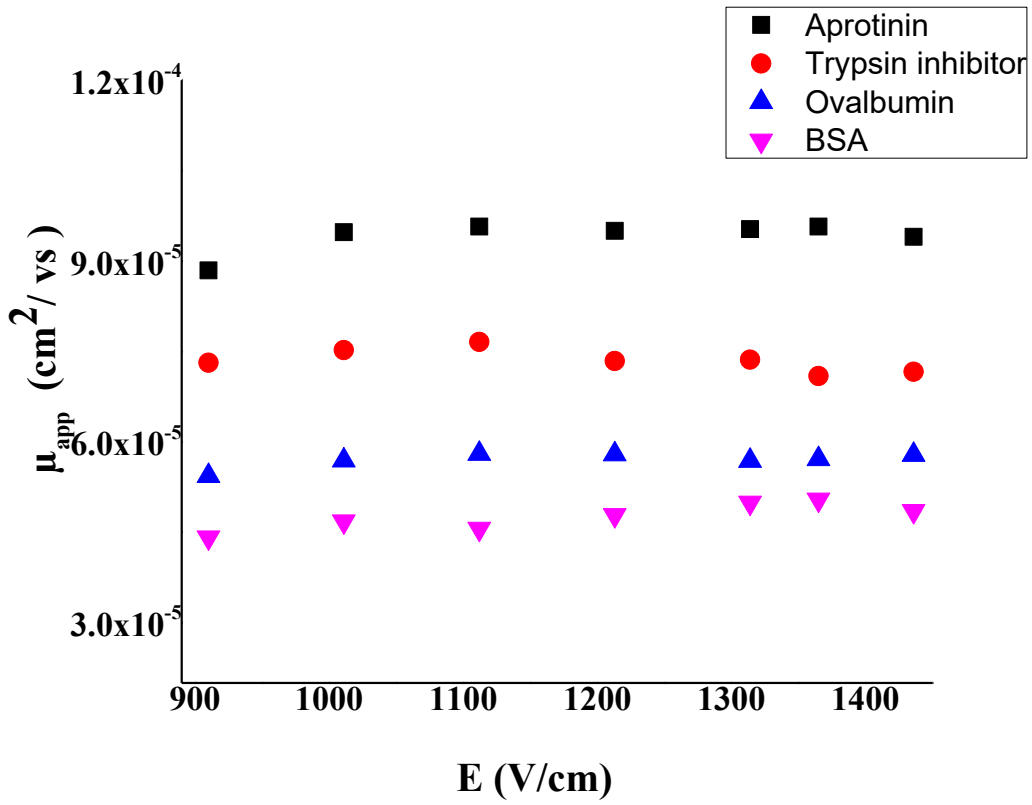

Figure 3-4. Plot of apparent mobility (μapp) vs electric field for aprotinin (6.5kDa), trypsin inhibitor (20kDa), ovalbumin (45kDa), and bovine serum albumin (BSA, 66kDa); device used: 310 nm silica particles CSA in 13 mm long bed entrapped with photopolymerized 0.5% monomer solution, using 4x TBE buffer (pH 8.3).

3.3.2 Molecular weight determination

Based on the Ogston sieving model, the logarithm of the electrophoretic mobility of the SDS-protein complexes are proportional to their molecular size i.e. $\log \mu \alpha -M$ [119]. Fitting results to this data identifies the separation mechanism, and can be used to identify molecular weights with appropriate standards. Figure 3-6 shows the plot of the logarithmic electrophoretic mobility of four proteins as a function of their molecular weight. A linear least squares fit to the data shows good linearity (R^2=0.986), indicating that the separation mechanism resolves proteins upon the basis of size [50]. This result is consistent with Ogsten theory, and it can be used for molecular weight determination of unknown proteins.

As an example, the peak of ribonuclease A with molecular weight of 13.7 kDa at E= 810 V/cm, and L_d = 12 mm was obtained (Figure 3-6). The log mobility of the peak was calculated and the molecular weight interpolated based on the plot in Figure 3-5a. The plot predicts a molecular weight of 14.2±0.3 kDa which differs by 0.5 kDa from 13.7 kDa.

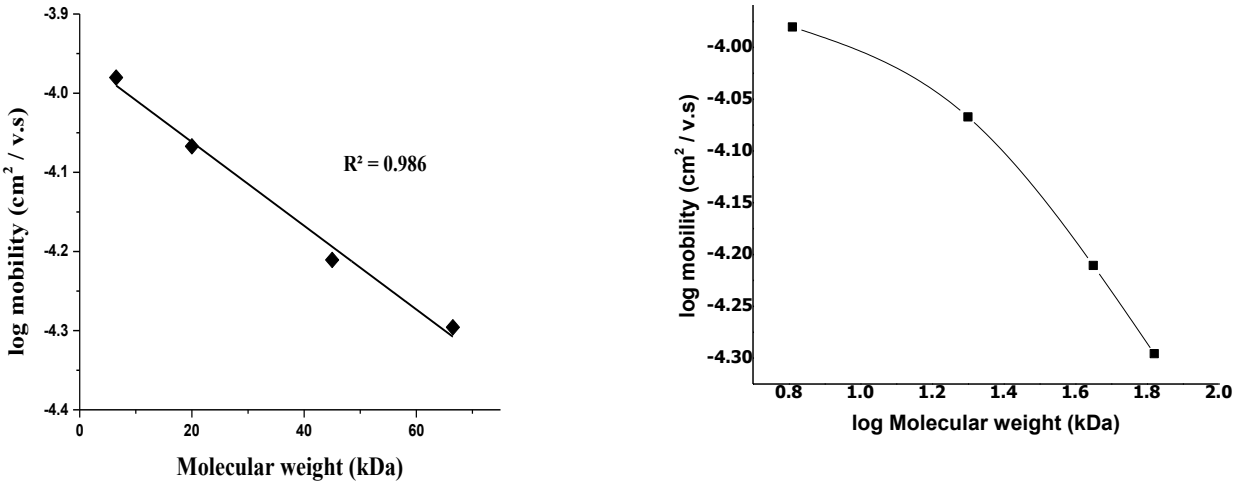

Figure 3-5. Mobility vs (a) molecular weight of aprotinin (6.5 kDa), trypsin inhibitor (20 kDa), ovalbumin (45 kDa), and BSA (67 kDa) and (b) log molecular weight of aprotinin (6.5 kDa), trypsin inhibitor (20 kDa), ovalbumin (45 kDa), and BSA (66 kDa) in a 310 nm particle polymer entrapped CSA bed, error bars are smaller than the plot symbols.

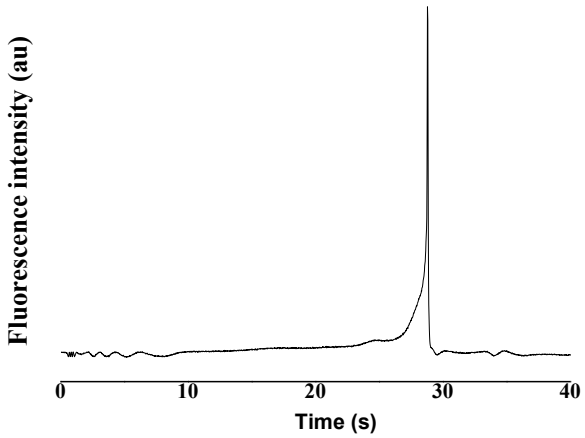

Figure 3-6. Electropherogram of ribonuclease A (13.7 kDa), in a 310 nm particles polymer entrapped CSA bed, at E= 810 V/cm, L_d = 12 mm.

3.3.3 High molecular weight proteins separation

Many high molecular mass proteins (MW>100 kDa) are known to be involved in transcription related to cytoskeleton, defense, and immunity in higher eukaryotic organism [164]. Since these high molecular weight proteins would be targets for genomic therapeutics, efficient separation and purification techniques are required [165]. Protein biomarkers are a measurable indicator of a specific biological state, particularly one with relevant to the risk of contracting a disease, or the presence and stage of a disease [166]. Some high molecular weight proteins such as myosin heavy chain (200 kDa), dystrophin (400 kDa), or thyroglobulin (330 kDa) are responsible for diseases and represent good targets for proteins cannot be separated properly by SDS-PAGE [167–169]. In the past 20 years, there have been many attempts to optimize the composition of protein separation matrices to enhance the electrophoretic resolution of high molecular weight proteins using polyacrylamide or agarose polymers [170–173]. Gel electrophoresis is a useful tool for protein separation. However, using this method with large proteins in not easy, because protein migration is very limited even in large porosity gels, which are also mechanically unstable and require long separation times [174].

A gel with low percentage of acrylamide is typically used to separate large proteins, but the gel becomes extremely weak and difficult to handle [167]. We examined the stabilized CSA bed to separate some high molecular weight proteins. Such proteins are also separated in the same entrapped beds, although longer injection times are required to obtain good peak sizes, resulting in some loss of separation efficiency.

Separation of a mixture of four high molecular weight FITC-labeled SDS denatured proteins is shown in Figure 3-7. Protein mixtures consisting of ovalbumin

(MW 45 kDa), BSA (MW 67 kDa), ß-galactosidase (MW 116 kDa), and myosin (MW 223 kDa), were separated at 1,450 V/cm, using a 50 s sample injection at 180 V/cm. These four proteins were separated based on their sizes in less than 60 s. Figure 3-8 demonstrates separation of another high molecular weight protein mixture, comprised of BSA (MW 67 kDa), myosin (MW 223 kDa), and thyroglobulin (330 and 660 kDa), using a polymer entrapped 310 nm CSA silica bed length of 13 mm at an applied electric field intensity of 1300 V/cm. The results demonstrate separation of high molecular weight SDS denatured proteins in the entrapped beds.

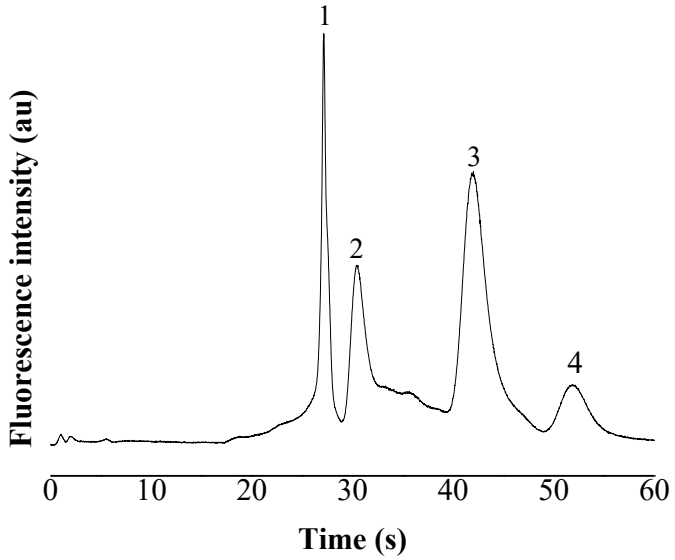

Figure 3-7. Electropherogram of SDS denatured (1) ovalbumin (MW 45 kDa), (2) BSA (MW 66 kDa), (3) ß-galactosidase (MW 116 kDa), and (4) myosin (MW 223 kDa), obtained with a polymer entrapped 310 nm CSA silica bed length of 13 mm at an applied E of 1450 V/cm. Sample was injected for 50 s at 180 V/cm.

Table 3-2. Peak resolution of SDS denatured ovalbumin (MW 45 kDa), BSA (MW 66 kDa), ß-galactosidase (MW 116 kDa) and myosin (MW 223 kDa).

Molecular weight (kDa)	45-66	67-116	116-223
Peak resolution	0.97±0.02	3.08±0.03	2.75±0.02

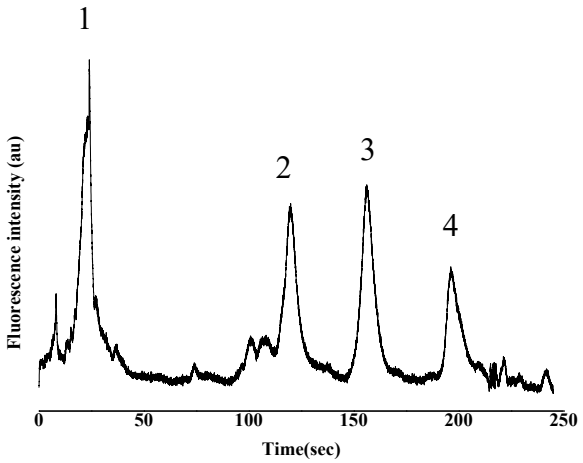

Figure 3-8. Electropherogram of SDS denatured (1) BSA (MW 67 kDa), (2) myosin (MW 223 kDa), (3,and 4) thyroglobulin (330 and 660 kDa) obtained with a polymer entrapped 310 nm CSA silica bed length of 13 mm at an applied E of 1300 V/cm. Sample was injected for 70 s at 180 V/cm.

3.3.4 Mass resolution

Resolution of sample components is the ultimate goal in separation science. Peak resolution can be calculated by equation 1-14. The use of the high electrical field results in short analysis times, high efficiency, and improved resolution, as the shorter separation

time gives narrower peaks. To characterize the resolving power of the polymer entrapped CSA beds, the minimum resolvable molecular weight difference (R) was estimated using R= ΔM/Rs, where ΔM is the mass difference and Rs is the resolution between two peaks. Figure 3-9 shows a near baseline separation of two proteins whose ΔM is 0.6 kDa, ribonuclease A (MW 13.7 kDa), and lysozyme (MW 14.3 kDa) over 8 mm separation length at an electric field strength of 1,380 V/cm. A plate height was obtained for ribonuclease A of 56 nm. From the Figure, R is estimated as 1-2 kDa, which is superior to what has been reported in the literature for size based separation of SDS denatured proteins using on-chip CSA (R = 9 kDa) [38] and using on-chip gel/polymer matrix (R = 4.1 and 5.8 kDa) [50,175].

Peak resolution, efficiency and speed of analysis are greatly improved for the polymer entrapped beds compared to literature values reported for on-chip analysis of similar proteins using native CSA beds [38]. The greatly improved speed of analysis (~ 30 sec) vs ~16 min required to separate four similar proteins by Zeng and Harrison [38] using the same 310 nm silica particles, is due to the high electric field applied on the polymer entrapped CSA bed.

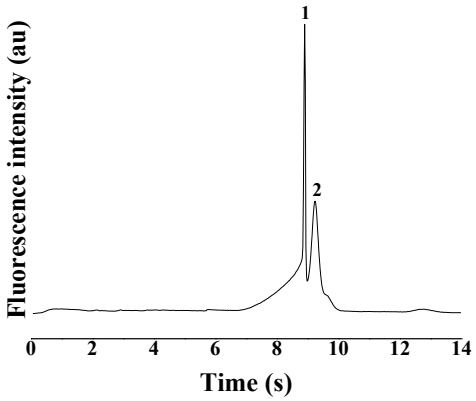

Figure 3-9. Electropherogram of 1- ribonuclease A (13.7 kDa), and lysozyme (14 kDa), in a 310 nm particle polymer entrapped CSA bed at E= 1255 V/cm, L_d = 8 mm.

3.3.5 Effect of Particle Size on Resolution Efficiency

Efficient sieving- based protein separation in the CSA bed requires small pore size. The pore size of the packed particles is 15% of the particle sizes. Smaller pore sizes should provide higher quality in separation of proteins, as initially demonstrated by Zeng et al. [38]. Figure 3-10a,b demonstrate separation of four SDS-denatured proteins using two different particle sizes. Four proteins of 14-67 kDa were separated in a matrix of 540 nm silica particles (81 nm pore size) with E=1440V/cm, and a detection length of 13 mm. The resolution was 2.3 between the 6.5 and 20 kDa proteins and 1.5 between the 20 and 45 kDa, proteins respectively.

Figure 3-10b exhibits the greatly improved separation efficiency using 310 nm silica particle array with pore size of 46 nm. Four proteins were baseline resolved. The resolution between 6.5 kDa and 20 kDa improved to 5.6, also the resolution between 20

kDa and 45 kDa improved to 2.7. Employing smaller particles packed bed produces smaller pore size as a sieving matrix, so the efficiency of the separations is improved as a result.

a

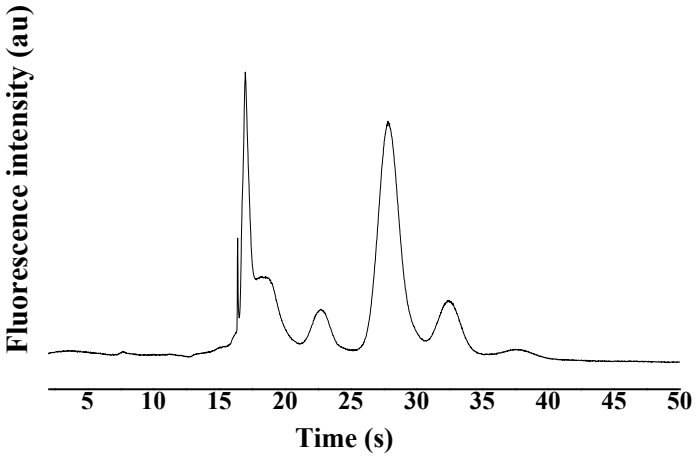

b

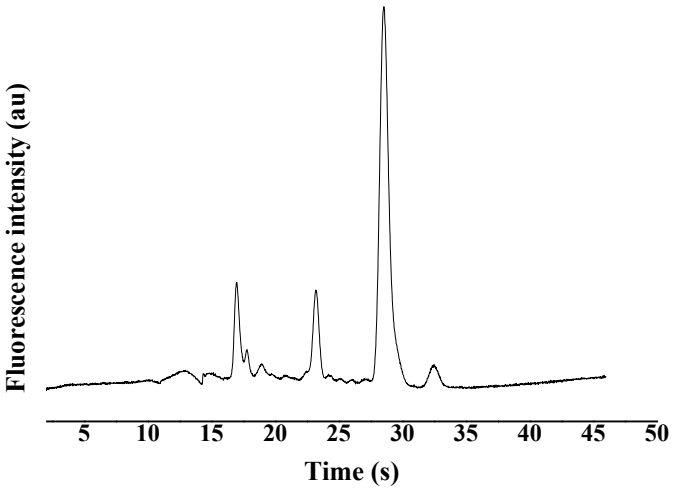

Figure 3-10. Electropherogram of (a) aprotinin (6.5 kDa), trypsin Inhibitor (20 kDa), ovalbumin (45 kDa), and BSA (66 kDa, E=1440 v/cm, L= 13 mm. a) 540nm, b) 310nm particles.

3.3.6 Effect of detection length on resolution efficiency

Figure 3-11 demonstrates separation of four SDS-denatured proteins using 6 and 13 mm detection lengths. Four proteins of 6.5-67 kDa were separated in matrix of 310 nm silica particles with E=1440 V/cm and a detection length of 9 and 13 mm. The resolution between trypsin inhibitor (20 kDa) and ovalbumin (45 kDa) improved from 1.2 to 2.8. Therefore, increasing the detection length results improved resolution (equation 1-17). A plate height as low as 93 nm obtained for lysozyme.

a

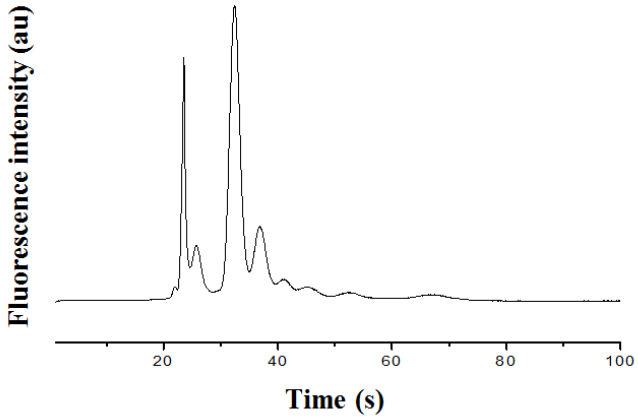

b

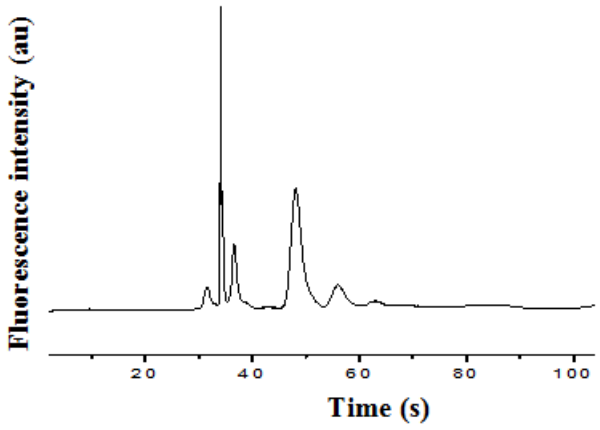

Figure 3-11. Electropherogram of (a) lysozyme (6.5 kDa), trypsin Inhibitor (20 kDa), ovalbumin (45 kDa), and BSA (66 kDa), E= 920 V/cm, 310 nm particles (L_d) of (A) 6mm (B) 13mm.

3.3.7 Reproducibility of CSA bed fabrication

Reproducibility of bed fabrication and performance is critical for routine analytical use, and can also provide a diagnostic of the bed condition. The fabrication and

polymer entrapment of the CSA structures was monitored by visual inspection for cracks and by electrokinetic injection of a single FITC-labeled protein multiple times, monitoring migration time changes. This was done for over 35 devices. Devices were deemed functional when visually free from cracks and the migration time of the protein was within 11% of average. The device yield when applying these criteria was 87%. The reproducibility of the polymer entrapped CSA bed performance was assessed through the %RSD of the migration times of the four proteins separated (Figure 3-12). A polymer entrapped CSA bed was readily used for a week to separate four proteins, multiple times a day using E =1,100 V/cm. In contrast, the native silica particle CSA bed was not stable for even one day, due to the movement of particles in electric field. The %RSD of the protein migration times varied from 0.3% to 0.5% (n=4) in one day and < 0.83% over a period of 7 days (n=28). The apparent mobility of the proteins in a given polymer entrapped CSA bed remained constant (Figure 3-4), with %RSD in the range of 2.2 - 4.7%, demonstrating the stability of the entrapped bed. The overall %RSD of migration time from chip-to-chip within a single fabrication run was 4.3% (n=3 beds), demonstrating reproducible packing and entrapment behavior.

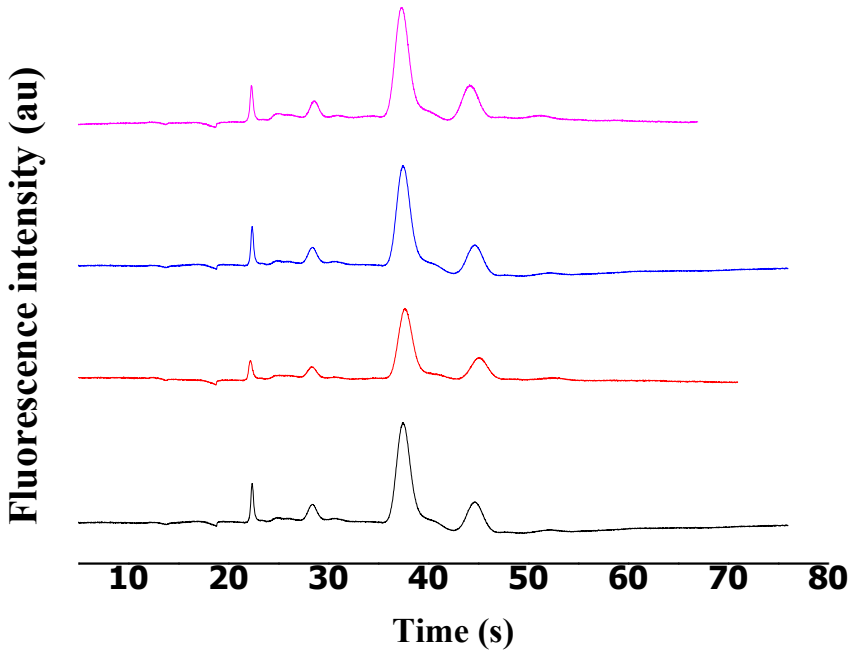

Figure 3-12. Electropherogram of (a) aprotinin (6.5 kDa), trypsin Inhibitor (20 kDa), ovalbumin (45 kDa), and BSA (66 kDa) at four replicate runs, E=1100 V/cm, (L_d) of 13 mm.

3.3.8 Performance comparison

The 56 nm plate height (Table 3-3) observed for SDS denatured protein is 35 times better than that previously reported for size based separation of SDS-denatured proteins in an on-chip CSA bed or polymer/gel matrix [3850], 120 times better than using microparticle packed on-chip columns for acetonitrile denatured proteins [135], 200 times better than for CEC of native proteins in polymer monolith columns [176], 35 times better than SDS denatured proteins in gel-filled microchannels [177] and 10 times better than highly optimized SDS capillary gel electrophoresis [178]. The efficiency is 8.5 times better than the reported value for much smaller and less complex amino acids and peptides

using thermally immobilized CSA on-chip [93], and 7 times better than other polymer stabilized CSA beds for SDS denatured proteins [43].

Table 3-3. Plate height calculated for separated proteins.

Proteins	**Aprotinin**	**Lysozyme**	**Ribonuclease A**	**Trypsin inhibitor**	**Ovalbumin**	**BSA**
H	250 nm	93 nm	56 nm	200 nm	600 nm	1 μm

3.4 Conclusion

The entrapment of CSA silica nanoparticles in microfluidic devices as presented here results in a highly stable crystalline structure fused together with minimal amounts of organic polymer in a web-like formation. Photoplymerization of methacrylates is a rapid, facile fabrication method for the stabilization of sub-micron scale CSA particle beds, retaining a high degree of order and packing quality upon polymerization. This polymer entrapment technique improved the stability of the CSA structure at high electric fields (up to at least 1,800 V/cm) allowing fast and highly efficient separation performances. For a separation length equals 13 mm, plate numbers of more than 106/m, with associated plate heights around 56 nm were observed for SDS denatured proteins. The study demonstrates the potential of CSA nanoparticles beds in microchips for ultra-fast separations, and the ability to separate close molecular weight proteins (ΔM = 0.6 kDa) in such short separation lengths will be valuable for biomolecular separations in microfluidic devices.

CHAPTER 4: PHOTOGRAFTING OF CHARGED MONOMERS ON HEMA COATED NANOPARTICLE BEDS FOR NATIVE PROTEIN SEPARATION

4.1 Introduction

Three-dimensional colloidal crystals fabricated via a colloidal self-assembly (CSA) [38] method provide nanoporous structures that offer a novel approach for separation of the biomolecules, i.e. DNA and proteins, under an external electrical field as a driving force [39,43,45,158,179–183]. The development of microfluidic devices for analytical and bioanalytical chemistry has, in the last there decades, led to ground breaking advances in terms of the speed of analyses, the resolution of separations and the automation of procedures [184–187].

However, nonspecific protein adsorption to the silica surface is a major concern in protein separation and causes lower efficiencies [107,188,189]. Even a small amount of protein adsorption on a surface can lead to unwanted fouling [107]. Figure 4-1 demonstrates the surface of a protein is not homogeneous. It may have hydrophobic, hydrophilic, cationic, and anionic patches at the same time. Furthermore, the distribution of these different patches on the protein surface and even in the protein structure are greatly affected by environmental factors such as pH, ionic strength, temperature, interaction with small

organic molecules, and so on. Protein adsorption can be the result of electrostatic, hydrogen bonding, charge-transfer, and/or hydrophobic interactions [190].

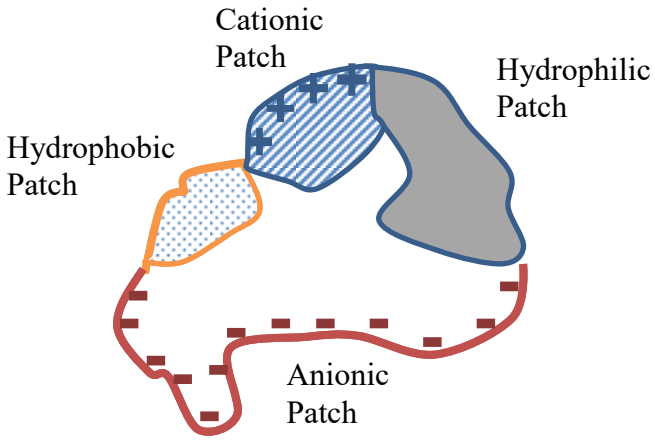

Figure 4-1. Schematic diagram of a model protein with heterogeneous surface.

Protein adsorption is largely due to negatively charged deprotonated silanol groups of the native silica surface. Sorption of proteins onto the surface of silica particles can cause poor reproducibility, band broadening, and reduced efficiency. Variation in EOF caused by adsorption is severe problem. In order to minimize protein adsorption, numerous approaches have been studied, including the use of extreme pH [191], neutral or charged polymer coating such as [2-(methacryloyloxy) ethyl] trimethylammonium chloride (META) [83], polyethylene glycol (PEG) [192–194], zwitterionic [195,196], and high ionic strength additives [197]. Photografting onto synthetic polymers as a means of changing polymer properties was pioneered by Oster and Shibata in the late 1950s [198]. Later a rapid and efficient photografting technique using benzophenone as a hydrogen abstracting photoinitiator was developed by Ranby [199,200].

The strategy of further modifying a polymer coating by photografting is fast and efficient, requiring less time and less complication than the atom transfer radical polymerization method [83], enabling the immobilization of various surface functional group. Here we used META monomer, which is positively charged, and sulfobetaine methacrylate (SBMA) as a zwitterionic monomer for photografting to 2-hydroxyethyl methacrylate (HEMA) coated silica nanoparticles. An important characteristic of SBMA is the fact that it has both positively and negatively charged units within the same monomer side chain. SBMA maintains overall charge neutrality, and because of the hydrophilic surface, possesses excellent anti fouling properties. As a result, SBMA reduces nonspecific adsorption of proteins.

This chapter describes the experimental processes of surface photografting, characterization, and application of surface grafted HEMA coated silica nanoparticles by META and SBMA monomers.

4.2 Materials and methods

4.2.1 Samples and reagents

The initiation, 4-(dimethylamino) benzophenone, SBMA, and META were purchased from Sigma-Aldrich Canada (Oakville, ON). The other reagents were previously listed in section 3.2.

4.2.2 Sample preparation

Proteins (Table 4-1) were individually conjugated with fluorescein isothiocyanate (FITC) (section 3.2.2, chapter 3). Before separation, intact proteins were diluted with running buffer (4× TBE) to a final concentration of 10^{-8}-10^{-7} M. Deionized water having a resistivity of 18 MΩ (Milli-Q UV Plus Ultra-Pure Millipore System, Milford, MA) was used to prepare all reagents and samples. In some cases, acetonitrile was added to the running buffer, while to change the buffer pH 0.1 M HCl or 0.1 M NaOH were added. Solutions were passed through a 0.22 μm pore size filter before use.

Table 4-1. Proteins and their molecular weights, and pIs used in this chapter.

Proteins	Molecular weight (kDa)	pI
cytochrome c	12	10.2
Ribonuclease A	13.7	9.3
Lysozyme	14	11
Trypsin Inhibitor	20	4.6
α-chymotrypsinogen	25.6	7
BSA	67	4.9

4.2.3 Chip preparation

Briefly, an optimized monomer solution was comprised of 0.5% (v/v) of a mixture of HEMA and EDMA (30%:70%, v:v) the free radical initiator benzoin (1 wt%

benzoin per weight of monomer) in 99.5% of the porogenic solvent, methanol. The photopolymerization steps are explained in detail previously (section 2.2.2).

4.2.4 HEMA coated META photografting silica nanoparticles procedure

For photografting of positively charged monomer on the surface of HEMA coated silica particles the optimized monomer solution of META 1% v/v, methanol 66% v/v, water 33%, and 4-(dimethylamino) benzonphenone 0.2 wt% was prepared. Once all the channels were filled with the monomer solution, the chip placed on a UV Transilluminator equipped with six 15-W 312-nm tubes (model TS-312R, Spectroline, Spectronics corp., Westbury, NY) for 5 min for photografting. The photografted particle bed was then flushed with methanol/water (1:1 v/v) to remove un-reacted reagents.

4.2.5 HEMA coated SBMA photografting silica nanoparticles procedure

In this thesis for photografting of SBMA on the surface of HEMA coated silica particles the optimized solution, consisting of SBMA 0.5% v/v, methanol 36.8% v/v, water 62.6%, and 4-(dimethylamino) benzonphenone 0.2 wt% was prepared. Once all the channels were filled with the SBMA monomer solution the chip was placed on a UV Transilluminator equipped with six 15-W 312-nm tubes (model TS-312R, Spectroline, Spectronics corp., Westbury, NY) for 5 min for photografting. The photografted particles were then flushed with methanol/water (1:1 v/v) to remove un-reacted reagents.

4.2.6 Separation and Fluorescence Detection

The methodology of separation and fluorescence detection is similar to what explained in section 3.2.4.

4.3 Results and discussion

4.3.1 Electrochromatography of native proteins on HEMA coated CSA bed

The applicability of neutral, hydrophilic HEMA coating for the separation of native protein was investigated. Separation of two native proteins, trypsin inhibitor and α-chymotrypsinogen, negatively charged in 4×TBE, 40% ACN (acetonitrile), pH=9.0 was performed. ACN was added to the running buffer to reduce nonspecific adsorption of proteins on HEMA surface.

Figure 4-2 shows electrochromatograms of two separated proteins at two different electric field strengths. An RSD of 0.41% in migration time was obtained for 3 runs. Runs in native silica particle beds gave broad, poorly reproducible peaks. The results indicate that the coating is quite effective in reducing protein adsorption compared to a native silica particle packed bed. However, proteins are denatured in the presence of acetonitrile [201]. To avoid the use of organic solvents and reduce non-specific adsorption on HEMA we have examined surface grafting to adjust the surface chemistry. Surface grafting may allow us to separate native proteins in CSA packed beds without denaturing the proteins.

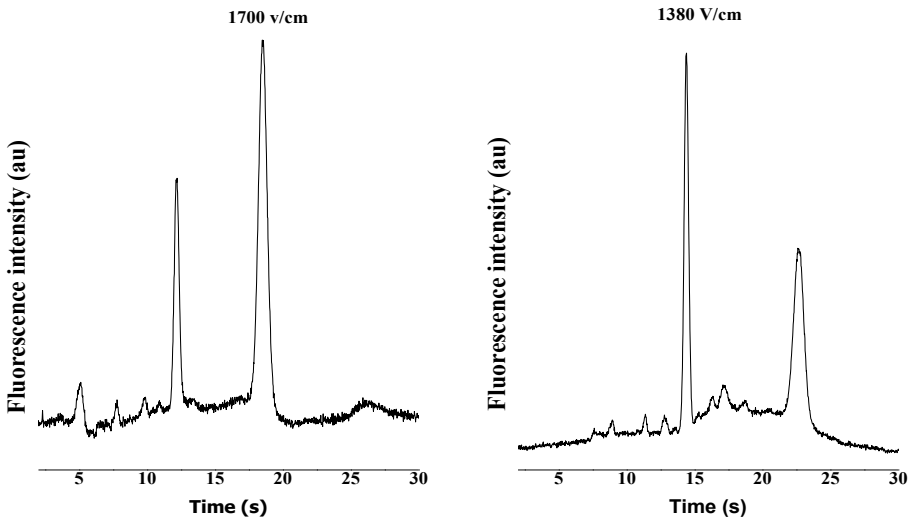

Figure 4-2. Electro-chromatogram of trypsin inhibitor and α-chymotrypsinogen, E=1700 V/cm, and 1350 V/cm, 4×TBE, 40% ACN, pH=9.0, L=7 mm, 310 nm particles, 0.5% HEMA.

4.3.2 META monomer solution composition characterization

The chip was prepared and the bed was stabilized and coated with HEMA based on the developed method (Figure 4-3a). Usually, benzophenone has been used as a photoinitiator for photografting, combined with the functional monomer and solvent. Benzophenone absorbs UV light, forms free radicals and abstracts hydrogen from the substrate surface. The radical formed on the surface adds to monomer in solution, leading to grafted chains (Figure 4-3b). The composition of monomer mixture and their performance quality are listed in Table 4-2. Solutions consisting of META 1% v/v,

methanol 66% v/v, water 33%, and 4-(dimethylamino) benzonphenone 0.2 wt% were used as the optimized mixture for photografting.

Table 4-2. Monomer solution compositions used for META grafting HEMA coated 310 nm CSA bed.

META%	Methanol%	Water%	Performance
0.2	66.54	33.26	×
1	66	33	✓
5	63.4	31.6	×
10	60	30	×

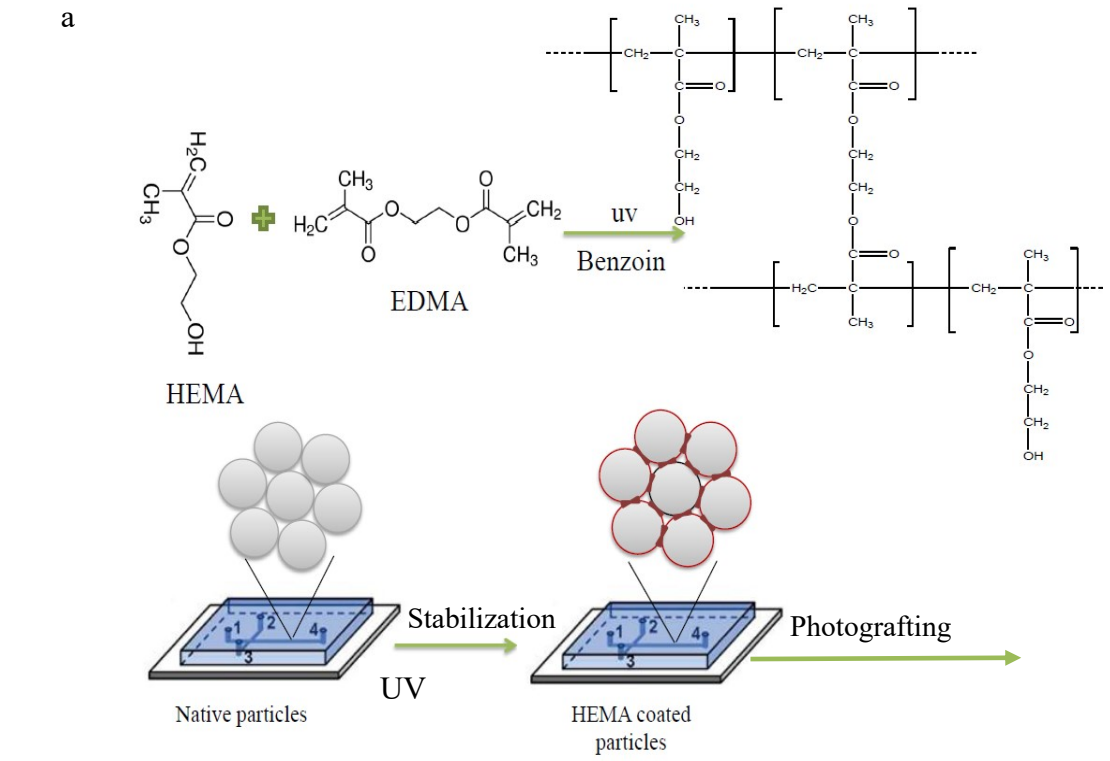

Figure 4-3. Schematic illustration of (a) HEMA coating of colloidal self-assembly in a one dimension separation microchip and (b) photografting of META on HEMA coated particle.

4.3.3 Characterization of META photografted Particles

4.3.3.1 X-ray Photoelectron Spectroscopy (XPS) Characterization of Photografted META Silica particles

Figure 4-4 shows the XPS spectra for HEMA coated silica particles and META grafted HEMA coated silica particles. The PDMS layer was peeled off before the analysis and the glass slides were cut to the smaller size to fit the sample holder. The XPS N 1s spectrum (Figure 4-4b) consists of one noisy peak component between 397 and 401 eV, associated with the amine quaternary ammonium cations ($N(CH_3)_3^+$) in the side chains of META [107] . Some photoreactions that can make other species of N, local environment differences and surface charging might be reasons for observing a broad peak. This peak was not observed in HEMA coated particles. We conclude the HEMA coated particles were grafted successfully with positively charged META polymer.

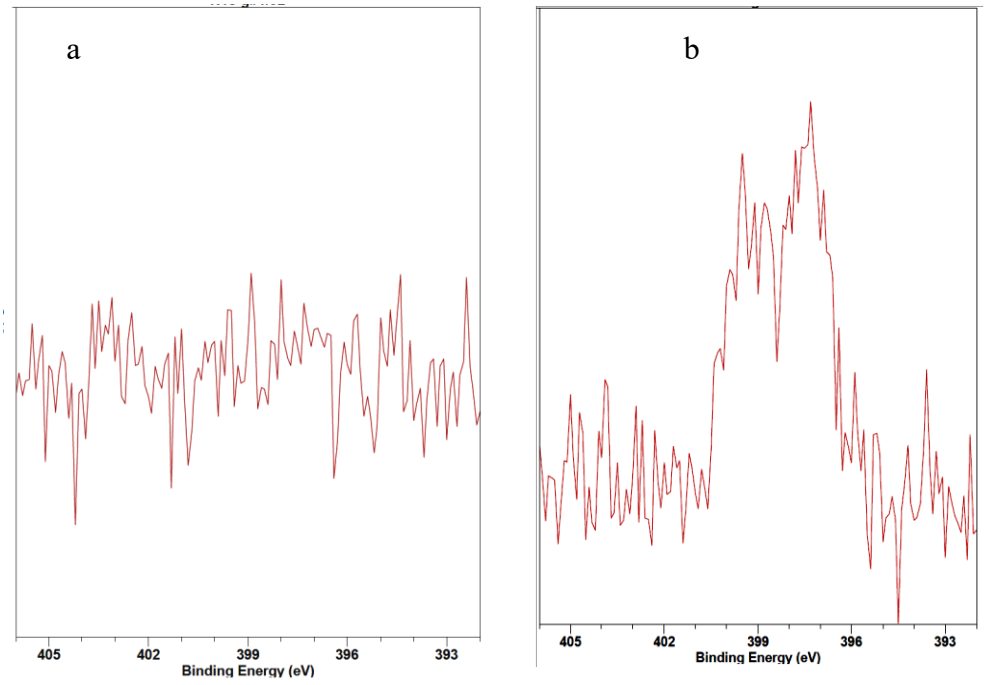

Figure 4-4. XPS N1s high resolution scan of (a) HEMA coated silica particles (b) 1% META grafted 0.5% HEMA coated silica particles.

4.3.3.2 Fourier transform infrared spectroscopy (FTIR) Characterization of Photografted META silica particles

We used surface infrared spectroscopy to characterize the META photograted HEMA coated silica particles. The FTIR spectra of HEMA and META grafted HEMA are shown in Figure 4-5. The chips were prepared using the same conditions except for the photografting step. The first spectrum shows the functional groups of HEMA coated silica particles and the second shows the functional groups of META grafted HEMA coated silica particles. All the functional groups of the polymer are assigned [202]. The bands around 3017 cm^{-1} and 1431 cm^{-1} are assigned to CH_3 stretching and bending vibration in $N(CH_3)^+_3$, which confirms META is grafted on to the HEMA coated silica particles.

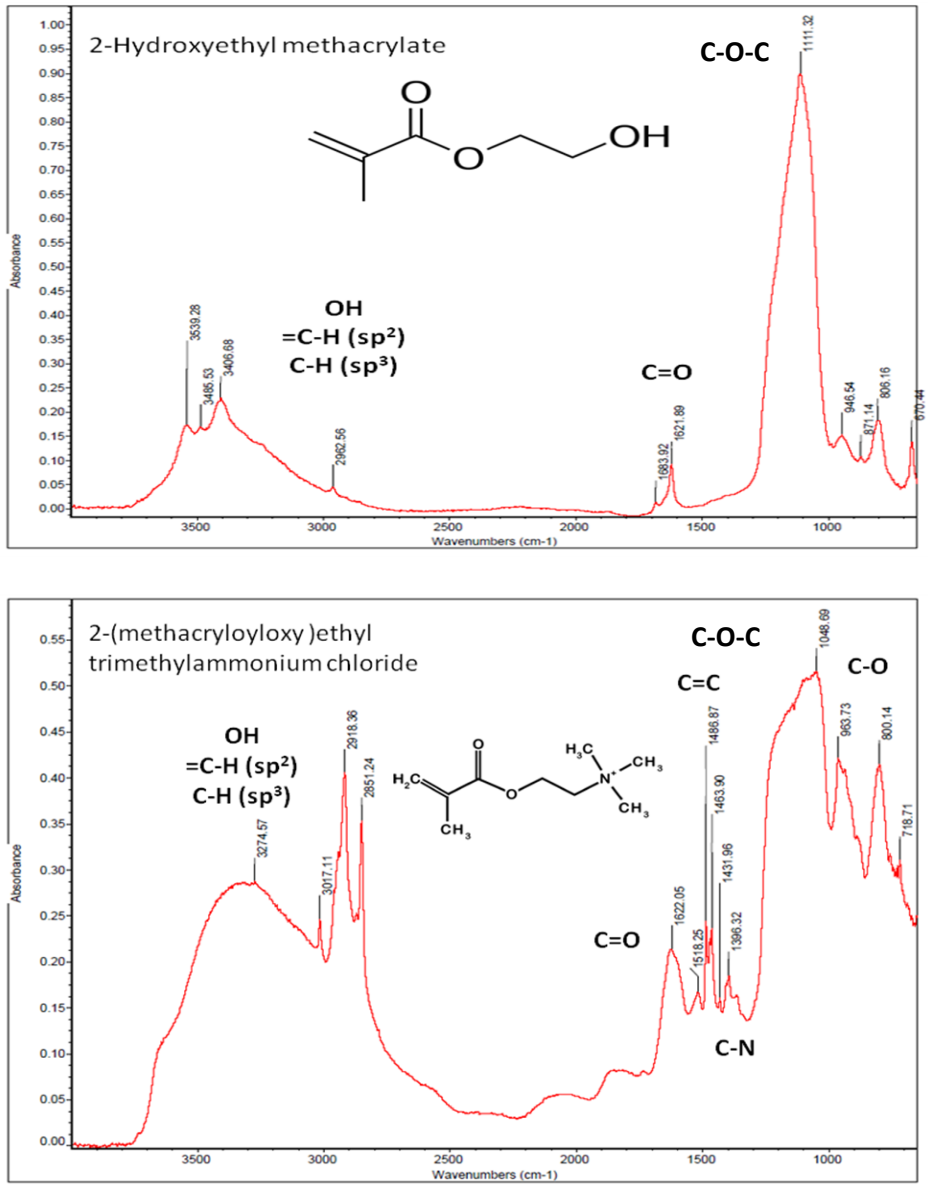

Figure 4-5. Infrared spectroscopy of (a) HEMA coated silica particles, and (b) HEMA-META coated silica particles.

4.3.3.3 Electroosmotic flow (EOF) measurement

The negative charge that the native silica capillary surface expresses over a wide pH range is also problematic in the separation of positive charged molecules such as

basic proteins, owing to electrostatic interaction. Therefore, the EOF must be suppressed or even reversed by shielding or altering the surface functionality to improve separation efficiency. The EOF caused by surface charge is mainly controlled by adjusting the pH of the running buffer or the additive's concentrations. Because these changes of the running buffer conditions significantly affect the conformation or charges of the protein analytes or the viscosity of the running buffer, it can be difficult to independently control the separation behavior and EOF mobility [189]. Therefore, when dynamic coatings (that is, buffer additives) impact the analytes being studied it may necessary to use covalent coatings. These coatings can increase, decrease, or reverse the surface charge and thus the EOF [83 203]. The neutral hydrophilic HEMA entrapping polymer film should also suppress the EOF in the CSA bed [83].

The EOF was measured by using neutral (BODIPY) dye's migration time in three chips. The EOF mobility was determined according to the following formula:

$$\mu_{EOF} = \frac{L_d L_t}{t_m V} \qquad 4\text{-}1$$

where L_d is the effective microchannel length L_t is the total microchannel length, t_m is the migration time of a neutral marker, and V is the applied electric field. Figure 4-6 shows that the EOF generated from polymer entrapped silica CSA beds is ~ 2×10^{-5} cm^2 v^{-1} sec^{-1} (RSD=4.1%, n=3 beds) toward cathode when using 4x and 5x TBE. Because META monomer is positively charged we expect to see a reverse EOF (toward anode) [83]. The results indicate that not all of the silicate groups on the particles are shielded after HEMA coating, and that the META additive is just enough to neutralize the surface, but not revers flow.

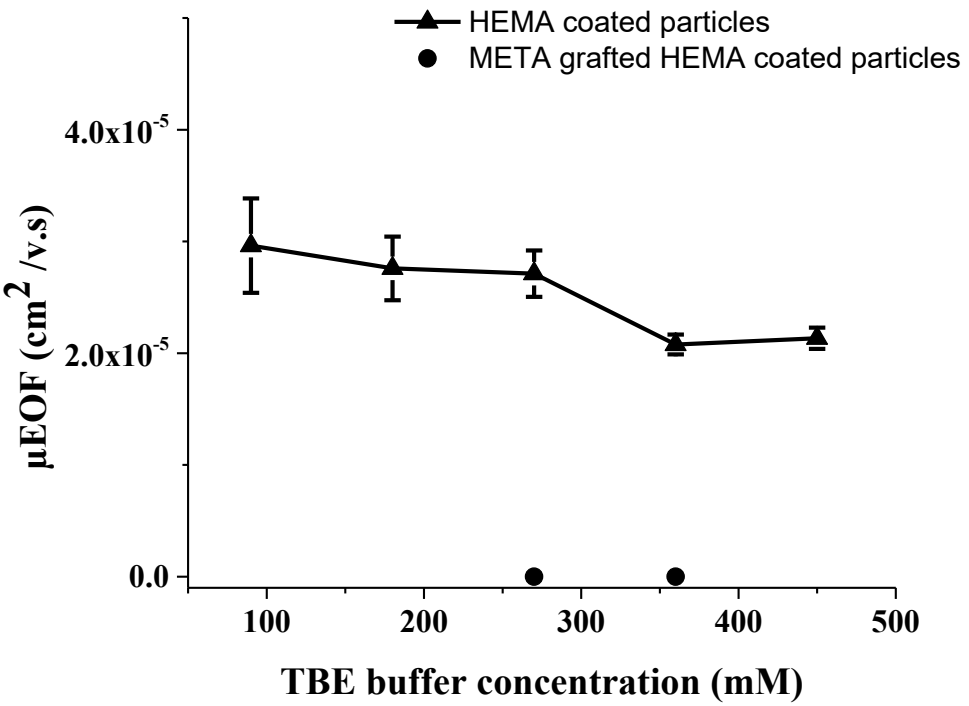

Figure 4-6. Electroosmotic flow (EOF) of HEMA coated silica CSA and META grafted silica CSA beds as a function of buffer concentration, pH = 8.3, measured from observed mobility of BODIPY; 310 nm silica particles in 10 mm long bed, entrapped with photopolymerized 0.5% HEMA and photografted with 1% META monomer solution, E = 100 V/cm.

4.3.4 Native Proteins Separation by META grafted HEMA coated silica CSA

We realized that the META monomer grafted on the surface of HEMA coated silica particles should give better separation for positively charged, native proteins. The separation of two different positively charged protein mixtures was attempted. Figure 4-7 shows electropherograms of a mixture of two FITC-labeled native proteins: cytochrome c (pka= 10.2), and ribonuclease a (pka=9.3) detected at a separation length (L_d) of 8 mm, using HEMA coated particles and META grafted HEMA coated particles.

The META gave positively charged sites on the polymer branches and both proteins were positively charged at the separation pH of 8. Buffers with pH of 6 and 4 were also tested, but photobleaching of the FITC was substantial, therefore the intensity and sensitivity of the protein peaks significantly dropped. The two proteins migrate through the CSA bed based on their charge and size; ribonuclease was detected first and cytochrome c was detected second, as determined by injecting each protein separately. Figure 4-7 shows that the resolution of the two proteins improved compared to a HEMA coated particle bed. The separation efficiency of these proteins was not good with the HEMA coated surface, presumably due to nonspecific adsorption. But when the surface was grafted by META the adsorption of positively charged proteins to the surface was apparently reduced. Also, the migration time of proteins changed when the META grafted particles were used for separation, due to the reduced EOF. The plate heights given for the native proteins are given for both HEMA coated and META grafted silica particle beds in Table 4-3.

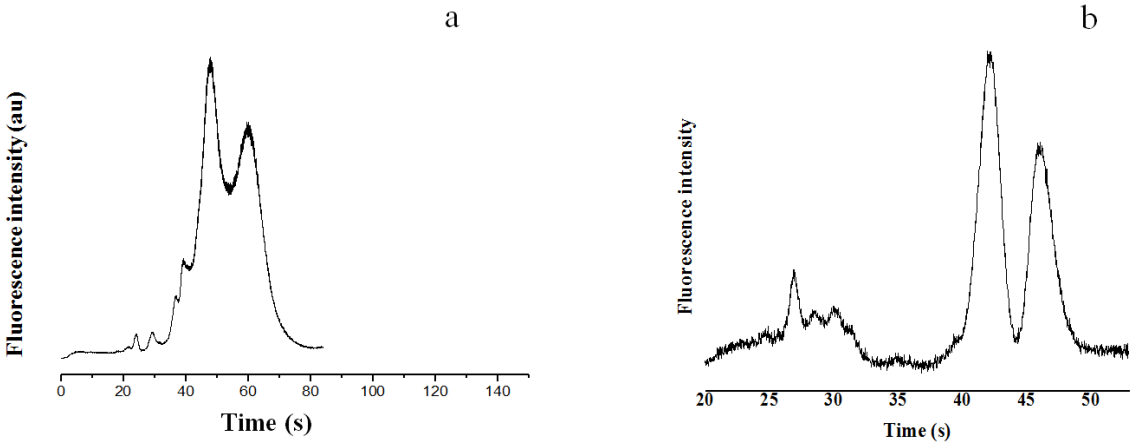

Figure 4-7. Electrchromatogram of cytochrome c (pka=10.2), and ribonuclease A (pka=9.3), E= 480 V/cm, L= 8mm HEMA coated 310 nm particles (a), HEMA -1%META grafted 310 nm particles (b).

Table 4-3. Plate heights calculated for separated native proteins on HEMA coated and META grafted surface.

	HEMA	HEMA/META
Cytochrome c	154 µm	0.9 µm
Ribonuclease A	307 µm	3.6 µm

Electropherograms of a mixture of two FITC-labeled native proteins, cytochrome c (pka= 10.2), and ribonuclease a (pka=9.3) detected at a separation length (L_d) of 13 mm, using different electric field strengths is shown in Figure 4-8. The proteins were separated in less than 15 s, at high field. The peaks get sharper and the resolution improved from 0.79 to 1.1 when the electric field increased from 840 to 1820 V/cm. Figure 4-8 shows that the META grafted HEMA column can withstand electric fields up to about 1820 V/cm.

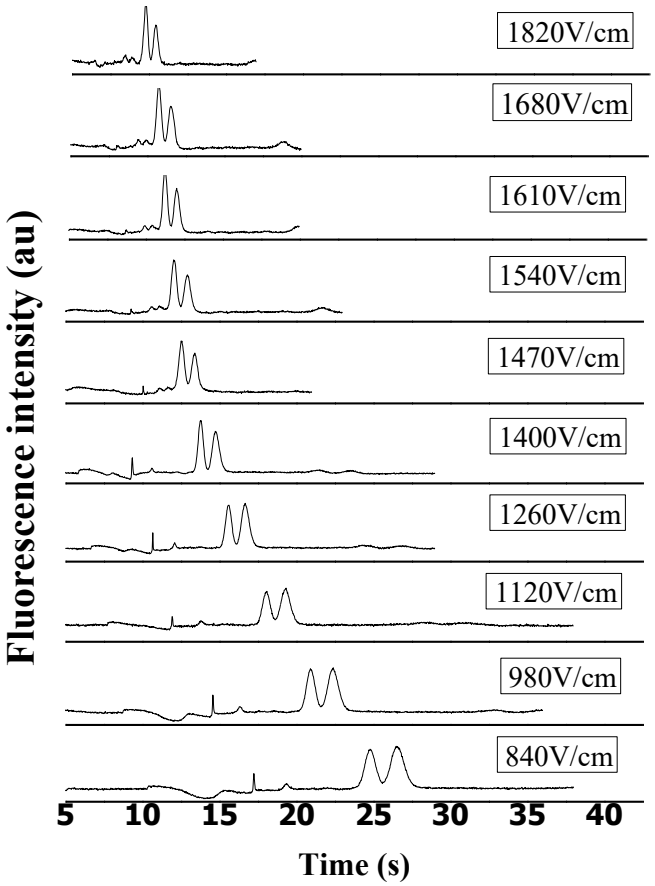

Figure 4-8. Effect of electric field (HEMA-1%META), E= 840– 1820 v/cm.

Figure 4-9 indicates the migration rate versus elevated electric field for cytochrome c (pka=10.2), and ribonuclease a (pka=9.3). There is a good linearity relationship between migration time and electric field, which indicates the stability of the column at high voltages.

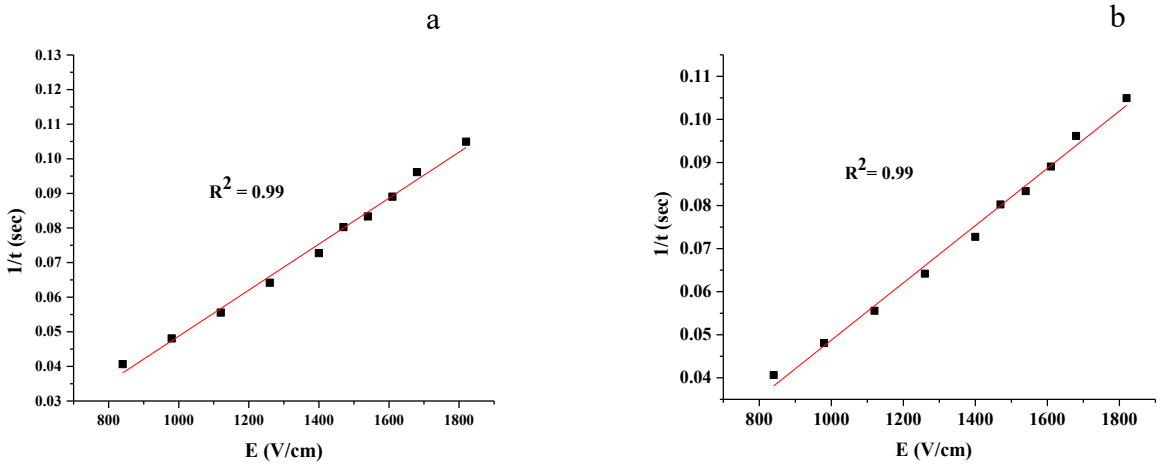

Figure 4-9. Electric field versus migration time, a) cytochrome c (pka= 10.2), and b) ribonuclease A (pka=9.3).

The peak resolution can be improved by increasing detection length. Figure 4-10 shows the effect of separation length on peak resolution of two basic separated proteins cytochrome c (pka= 10.2), and ribonuclease a (pka=9.3), L= 8 mm, 13 mm. The peak resolution improved from 0.9 to 1.05 when the detection length increased from 8 to 13 mm, although the diffusion of these two proteins increased and caused broader peaks. No significant improvement on plate heights was observed.

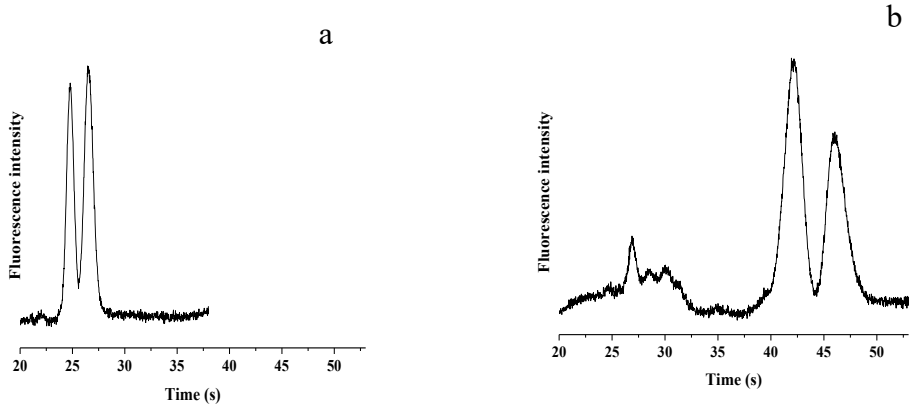

Figure 4-10. Effect of separation length, electropheromatogram of cytochrome c (pka= 10.2), and ribonuclease A (pka=9.3), E= 480V/cm, a) L= 8mm, b) L=13mm.

The reproducibility of the META entrapped HEMA- CSA bed performance was assessed through the percent relative deviation (%RSD) of the migration times of the two proteins (Figure 4-11). A RSD of 0.5% was obtained for 8 replicate runs. The best plate height of 550 nm was achieved for cytochrome c.

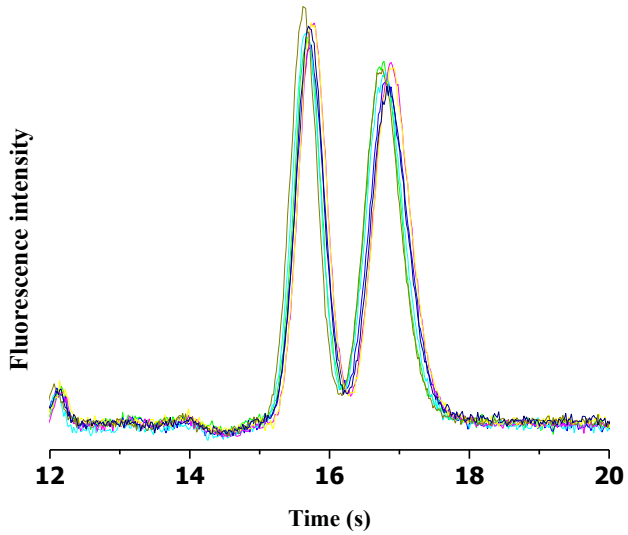

Figure 4-11. Electropheromatogram of cytochrome c (pka= 10.2), and α ribonuclease (pka=9.3), E= 1400 V/cm, L= 8mm, 8 runs. H= 550 nm, 0.5% RSD.

4.3.5 SBMA monomer solution composition characterization

Many hydrophilic surfaces can reduce protein adsorption. However, these surfaces are often not sufficient to prevent the undesirable adhesion of cells, bacteria, or other microorganisms [204]. One of the classes of materials that have been widely investigated for their nonfouling properties are zwitterionic polymers. Zwitterionic polymers are distinguished by the presence of both a negatively and positively charged

moiety within their pendant groups. This characteristic has been shown to contribute to protein adsorption resistance. A number of zwitterionic polymers have been investigated for their nonfouling properties including phosphorylcholine [205,206], carboxybetaine [207–209], and sulfobetaine [107,210,211]. This resistance to nonspecific protein adsorption makes the polymer a candidate for separation applications where irreversible fouling is problematic.

The focus of this investigation is on poly (sulfobetaine methacrylate) (polySBMA), whose monomer structure is shown in Figure 4-12. Surfaces coated with SBMA have been shown to have excellent resistance to nonspecific protein adsorption [196]. The chip was prepared and the bed was stabilized and coated with HEMA based on the developed method. To photograft SBMA on the surface of HEMA coated silica particles, different compositions of monomer solution were tested (Table 4-4). The optimized solution, consisting of SBMA 0.5%v, methanol 36.8%v, water 62.6%, and 4-(dimethylamino) benzonphenone 0.2 wt% was used as a monomer solution mixture.

Table 4-4. Monomer solution compositions used for SBMA grafting HEMA coated 310 nm CSA bed.

SBMA%	Methanol%	Water%	Performance
0.2	37	62.8	×
0.5	36.8	62.6	✓
5	35	60	×

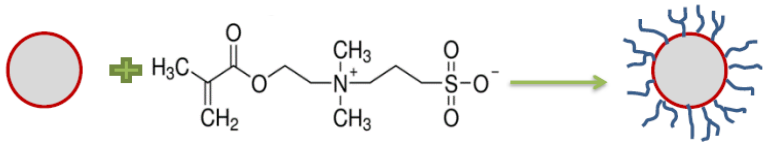

Figure 4-12. Schematic illustration of photografting of SBMA on HEMA coated particle.

4.3.6 Characterization of SBMA photografted Particles

4.3.6.1 EDX analysis of SBMA photografted surface

Since we could not detect the sulfonyl functional group by FTIR analysis, EDX analysis was employed. For EDX analysis, a Zeiss EVO SEM with LaB6 electron source, equipped with a Bruker energy dispersive X-ray spectroscopy system was used. This system has a spatial resolution of ~100 nm. SEM imaging was used to identify the bed region studied. We also evaluated HEMA coated silica CSA beds and beds following SBMA photografting using EDX analysis, to confirm the photografting of SBMA on HEMA coated particles. From the EDX data, the presence of the sulfur atom on the SBMA grafted HEMA particles, but not in the HEMA coated particles (Figure 4-13), confirms SBMA was grafted on the HEMA coated nanoparticles. To confirm that the sulfur signal is from the grafted surface a control was done. The SBMA monomer was introduced without any subsequent photopolymerisation, and then flushed with methanol and water. The EDX signal for S on the non-grafted bed was much lower than for the photografted bed, demonstrating that the surface was successfully grafted with SBMA.

(a) HEMA coated CSA bed

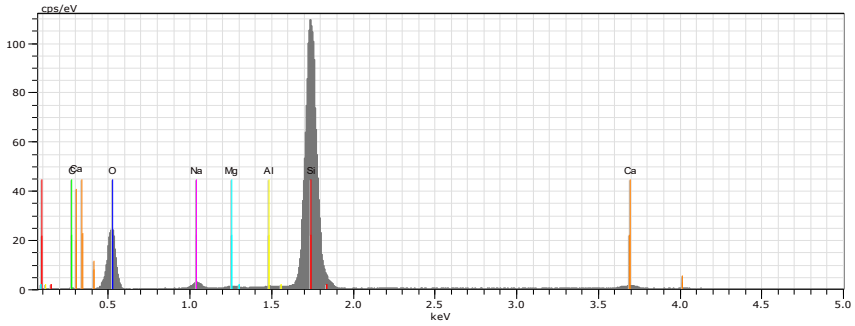

			[wt.%]	[wt.%]	[at.%]	[wt.%]
O	8	K-series	34.90	48.72	60.62	4.43
Si	14	K-series	31.08	43.39	30.76	1.38
C	6	K-series	2.23	3.12	5.16	0.73
Na	11	K-series	1.67	2.33	2.02	0.15
Ca	20	K-series	1.19	1.66	0.82	0.07
Mg	12	K-series	0.33	0.46	0.37	0.05

(b) SBMA/HEMA silica CSA bed

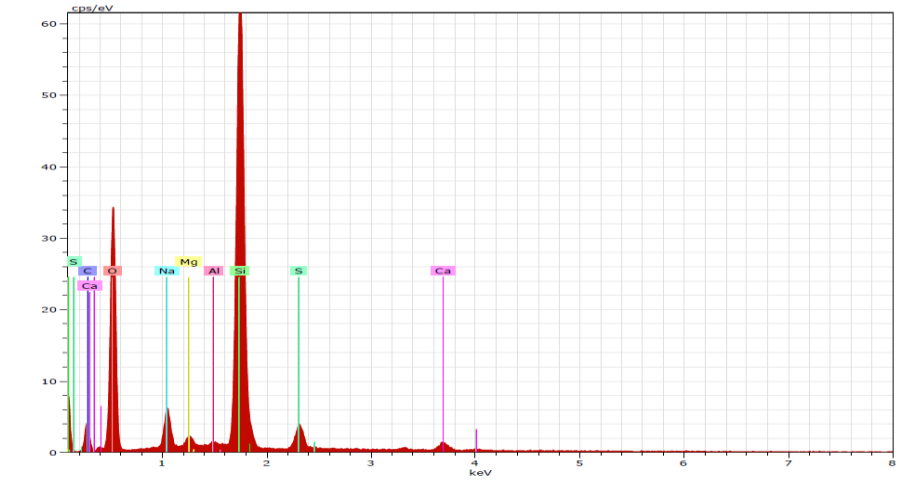

2_ 2 Date:9/24/2015 11:26:16 AM HV:15.0kV Puls th.:14.71kcps

El	AN	Series	unn. C [wt.%]	norm. C [wt.%]	Atom. C [at.%]	Error (1 Sigma) [wt.%]
O	8	K-series	42.08	45.19	51.63	5.31
Si	14	K-series	29.82	32.02	20.84	1.27
C	6	K-series	13.48	14.48	22.03	2.47
Na	11	K-series	3.10	3.33	2.65	0.23
S	16	K-series	2.28	2.44	1.39	0.12
Ca	20	K-series	1.35	1.45	0.66	0.08
Mg	12	K-series	0.71	0.77	0.58	0.07
Al	13	K-series	0.30	0.32	0.22	0.05
		Total:	93.11	100.00	100.00	

Figure 4-13. Electron diffraction x-ray spectroscopy (EDX) data of HEMA coated on-chip CSA particles (a) and SBMA/HEMA silica on-chip CSA particles (b); particle diameter 310 nm, monomer solution 0.5%.

4.3.7 Protein Separation by SBMA grafted HEMA coated silica CSA

Figure 4-14 shows two proteins injected individually to the SBMA grafted CSA bed, to determine the order of migration. Figure 4-15 shows two proteins separated on HEMA and on SBMA grafted beds. The SBMA grafted beds gave longer retention times and better peak resolution for trypsin inhibitor and BSA under the same conditions. The higher efficiency for trypsin inhibitor, in particular, sharpens the peak substantially, and causes peak height reversal for the two components compared to the HEMA surface. The EOF of 3.5×10^{-5} cm^2/Vs at pH 8.3 was measured by using neutral dye (BODIPY) migration time. The zwitterionic functional group of SBMA, and the higher EOF, may contribute to longer separation time. A plate height of 170 nm was obtained for trypsin inhibitor and 484 nm for BSA on SBMA surface, which shows the significant efficiency improvement compared to HEMA surface (Table 4-5).

Jiang et al. covalently bonded a sulfobetaine-type zwitterionic polymer onto the surface of fused silica capillary with a detection length of 40 cm and achieved an efficiency of 4.3×10^5 plate/m in 30 min [203]. Also an average plate height of 2.5 μm is reported by Mei [83]. In other work a plate height of 0.6 μm was obtained for native protein separation on a capillary coated with SBMA [196]. Our results give a plate height of 170 nm, which demonstrates the feasibility and versatility of the HEMA coating strategy SBMA photografting for microfluidic based protein separation.

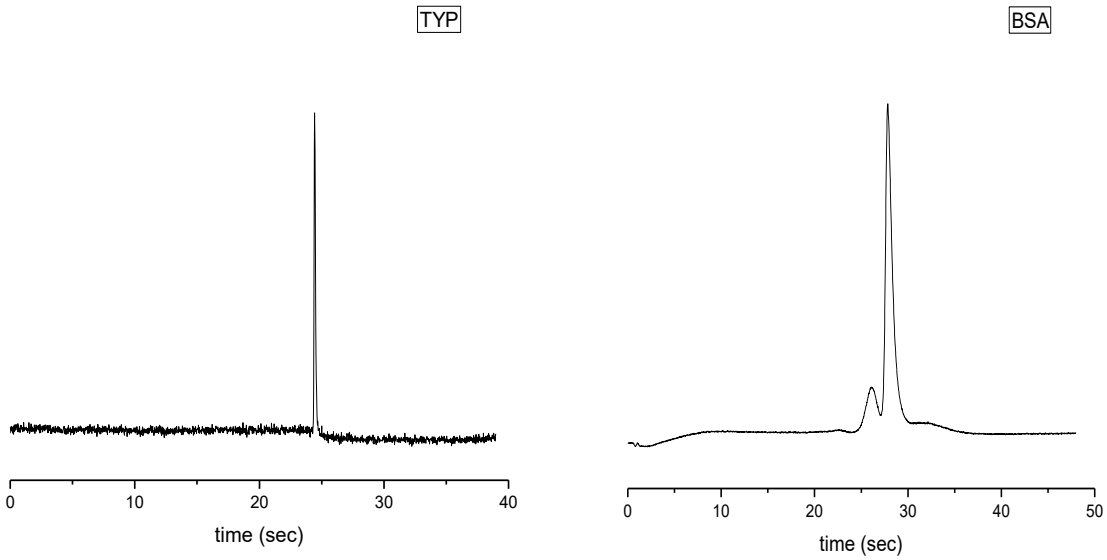

Figure 4-14. Electropheromatograms of trypsin inhibitor, and BSA, L=4mm.

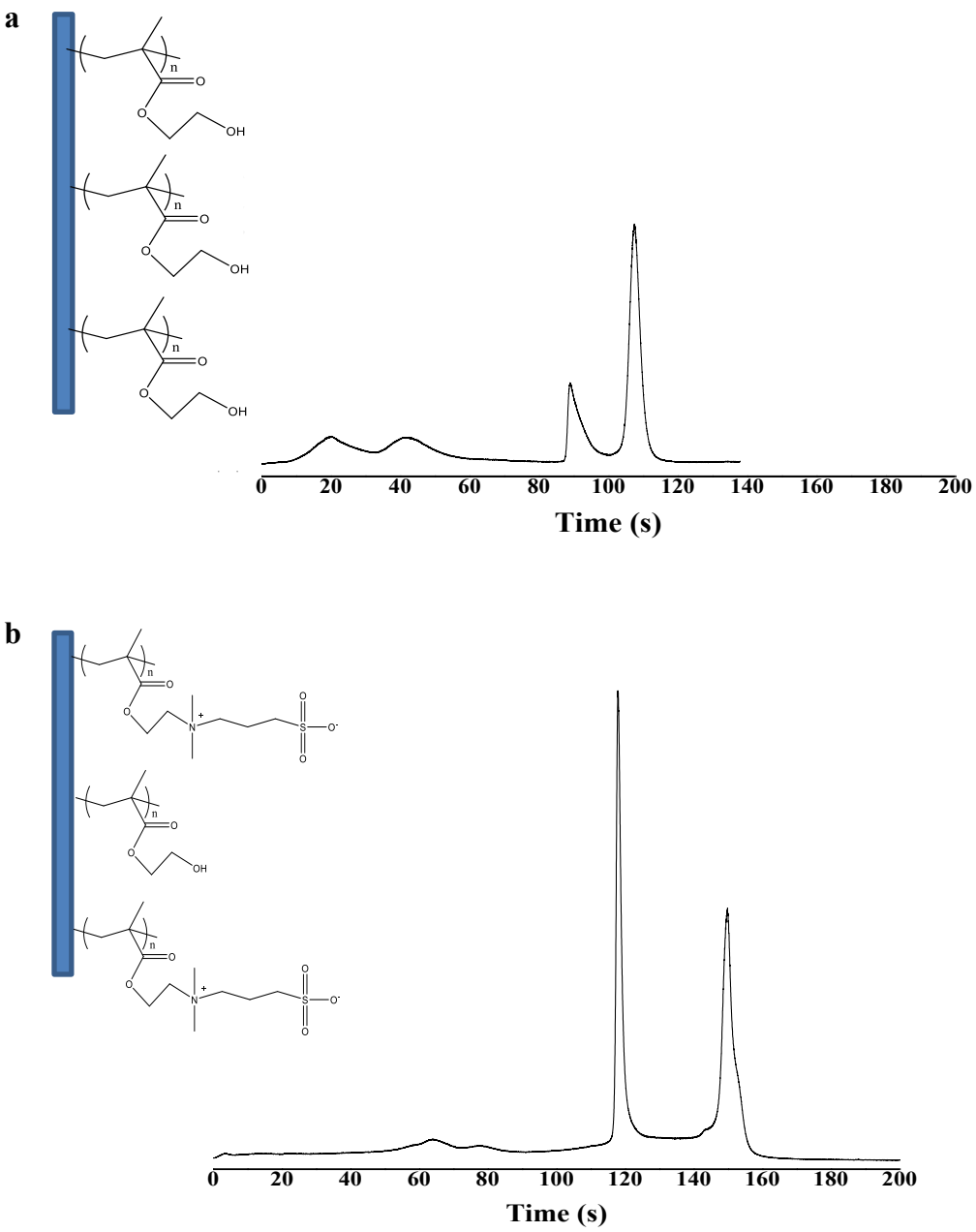

Figure 4-15. Electropheromatograms of FITC-labeled trypsin inhibitor and BSA separated with (a) HEMA coated and (b) SBMA grafted on HEMA coated silica particles. Conditions: 4×TBE buffer (pH 8.3). Separation voltage is 700 V/cm and detection was made at 7 mm.

Table 4-5. Plate heights calculated for separated native proteins on HEMA coated and SBMA grafted surface.

	HEMA	HEMA/SBMA
Trypsin inhibitor	3.3 µm	170 nm
BSA	1.1 µm	484 nm

4.4 Conclusion

This chapter describes the methods required to photograft HEMA coated CSA beds by META and SBMA functional polymers. Photo-initiated polymerization enabled coating the nanoparticles in microfluidic devices, and the surface chemistry was then tailored to fit the specific application by subsequent photografting of the surface. This coating strategy allows a fast and robust wall coating with controlled surface chemistry and surface biocompatibility. In both acidic and basic protein separations, appropriate polymer coating and grafting layers showed a good efficiency and reproducibility.

CHAPTER 5: ENTRAPPED 50 NM SILICA PARTICLE SELF ASSEMBLED COLLOIDAL ARRAY, CHARACTERIZATION, AND SEPARATION

Numerous studies describe successful self-assembly of particles <200 nm [35,164,212,213], but relatively few reports describe self-assembly of three-dimensional colloidal arrays of silica particles [214]. Cracks occurring in the colloidal packing of small particles <150 nm process typically divide a colloidal crystal film into single crystalline domains of several micrometers size. The best efficiency for protein separation based on a sieving mechanism is obtained when the size of the proteins is close to the pore size of the media [38]. The pore size small as 25 nm made by CSA on a microfluidic chip fabricated from monodisperse silica particles of 160 nm, in diameter, in work done by Zeng and Harrison [38]. Based on their studies of proteins, ranging in molecular weight from 20.1 kDa to 116 kDa, Ogston sieving was diagnosed to be the governing separation mechanism in a 1-D, DC external field strength of 30.9 V/cm. Also, a bidisperse structure with 10.5 nm pores (7% of the size of the larger particles) has been used for protein separation [215]. In that study, colloidal crystals with an average pore size ranging from 7 to 48 nm were fabricated on a microfluidic chip having a double-T configuration for the injection and separation stages [41]. Two proteins, trypsin inhibitor (20 kDa), and bovine serum albumin (BSA) (66 kDa), were separated by electrophoresis in a field of 30 V/cm. But the separation efficiency was limited in both studies [38,41] because of electric field strength limited by bed stability.

In this chapter, we report an in situ observation of crack formation with 50 nm silica nanoparticles in the packing process. The packing procedure was optimized and crack free CSA beds were obtained. Then the bed was stabilized with an optimized entrapment method. Finally, highly efficient separations were obtained for protein separation. We selected aprotinin, lysozyme, and insulin as model proteins to evaluate electrophoretic separation in a maximum external field of 1250 V/cm.

5.1 Materials and methods

5.1.1 Reagents

Uniform silica nanoparticles 50 nm in diameter (5% w/v, 10% dispersion) were obtained from Bangs Laboratories (Fishers, IN). Benzoin, methanol, 2-hydroxyethyl methacrylate (HEMA), and ethylene dimethacrylate (EDMA), aprotinin (6.5 kDa), ribonuclease A (13.7 kDa), insulin (5.8 kDa), and lysozyme (14 kDa) were purchased from Sigma-Aldrich Canada (Oakville, ON). (4× TBE, 0.1% w/v SDS) used as a running buffer. Deionized water having a resistivity of 18 MΩ (Milli-Q UV Plus Ultra-Pure Millipore System, Milford, MA) was used to prepare all reagents and samples. Solutions were passed through a 0.22 μm pore size filter before use.

5.1.2 Sample preparation

Proteins (Table 5-1) were individually conjugated with fluorescein isothiocyanate (FITC) following the Sigma-Aldrich labelling protocol, and stored at 4 ^{o}C in the dark until use. In order to denature the proteins, aliquots of FITC-labelled protein solutions were mixed with the same volume of buffer (4× (tris borate EDTA) TBE buffer, 4% w/v SDS, 8% v/v 2-mercaptoethanol), then incubated at 85 °C for 5 min. Before separation, denatured proteins were diluted with running buffer (4× TBE, 0.1% w/v SDS) to a final concentration of 10^{-8}-10^{-7} M. Deionized water having a resistivity of 18 MΩ (Milli-Q UV Plus Ultra-Pure Millipore System, Milford, MA) was used to prepare all reagents and samples. Solutions were passed through a 0.22 μm pore size filter before use.

Table 5-1. Proteins and their molecular weights used in this chapter.

Protein	Molecular weight (kDa)
Insulin	5.8
Aprotinin	6.5
Lysozyme	14
Trypsin inhibitor	20.1
Ovalbumin	45
BSA	67

5.1.3 Separation and Fluorescence Detection

4×TBE buffer (pH 8.3), with 0.1% v/v 2-mercaptoethanol and 0.1% w/v SDS, was used as a running buffer. The polymer entrapped CSA beds were pre-run by applying 100 V/cm until the current through the channels became static. Samples were loaded from reservoir 2 by applying an electric field of 180 V/cm for 30 s to reservoir 3, with other reservoirs grounded, to form a shaped injection plug. Separation was performed under different electric fields with a "pull-back" voltage of zero applied to reservoirs 2 and 3, to prevent sample leakage from the sample reservoir. A previously described laser induced epifluorescence detection system with a 488 nm Ar+ laser was used to monitor analyte signal 0.8 cm - 1.3 cm away from the injection point.

5.1.4 Chip preparation

Aqueous suspensions of 50 nm silica nanoparticles (5% w/v) were centrifuged for 13 min, different amounts of methanol were added, and then suspensions were ultrasonicated for 20 min prior to use. The on-chip colloidal self-assembly was performed following the protocol described by Zeng and Harrison [38]. Briefly, a 10 - 15 μL colloidal suspension was injected into reservoirs 1, 2, and 3 (Figure 5-1). The aqueous solution fills the channels spontaneously, forming a liquid meniscus at the outlet of the channel in reservoir 4. Once all channels were filled, reservoirs 1, 2, and 3 were covered with a PDMS piece to prevent solvent evaporation. Reservoir 4 was left open so that evaporation induced colloidal growth within the channels (Figure 5-1).

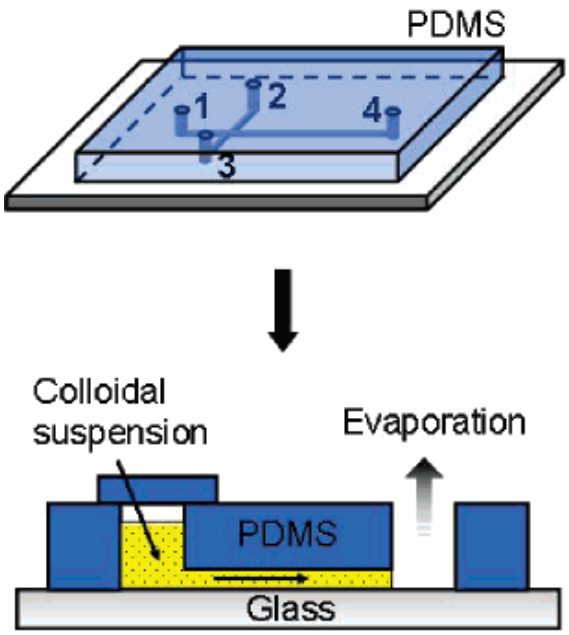

Figure 5-1. Schematic illustration of colloidal self-assembly in a one-dimension separation microchip, (Reprinted with permission from Y. Zheng et al. [38] Copyright 2007, ©American Chemical Society).

5.1.5 Stabilization of the CSA structure

Briefly, the monomer solution was prepared using various amounts of HEMA, along with EDMA and the free radical photoinitiator, benzoin, and the porogenic solvent, methanol. An optimized monomer solution was comprised of 0.09% (v/v) of a mixture of HEMA and EDMA (30%:70%, v:v) the free radical initiator benzoin (1 wt% benzoin per weight of monomer) in 99.9% of the porogenic solvent, methanol. Other compositions tested included use of 0.01%, and 0.2% (v/v) monomer mixture in methanol. Once the monomer mixture reached all reservoirs, the device was placed on a UV for 5-30 min for photopolymerization.

5.2 Results and discussion

With small particles the crack formation problem is severe. To understand the issue, we first review the CSA process within a microchannel. Figure 5-2 shows that as water evaporates at the drying edge it induces a macroscopic flow of liquid phase, resulting in migrating particles that consolidate at the compaction front. If they form ideal closed-packed structures, their spatially averaged volume fraction will be 74% [90]. Beyond the compaction front the particle volume fraction reduces to its initial volume fraction in the dispersion phase. The crystalline region advances smoothly as the flowing fluid brings particles at a specific flux, dependent on the local particle volume fraction [216], and delivers them to the compaction front. The carrying fluid itself flows through the growing nanoporous lattice, which has a length of y. At the fluid reaches the drying edge, it evaporates at a specific rate based on the water partial pressure gradient and mass transfer coefficient arising from the local atmospheric conditions.

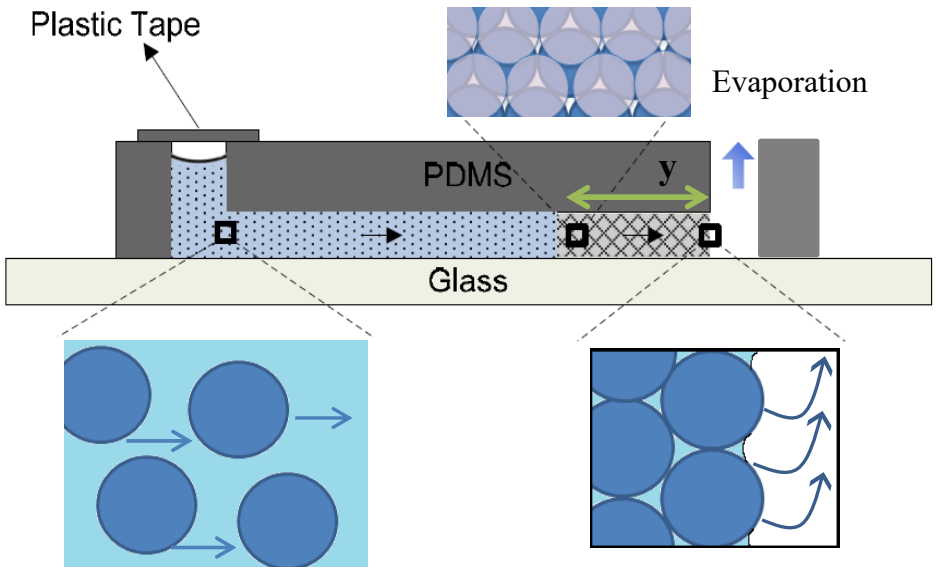

Figure 5-2. On-chip bimodal colloidal crystal self-assembly.

During evaporation, strong particle wetting prevents the intrusion of air into the colloidal crystal bed. Evaporation at the drying edge and fluid flow through the compact region are the two mechanisms that determine the overall fluid transport. Initially the compact region presents negligible resistance to flow. Thus, the evaporation rate is constant and limited by diffusion of vapor from the drying surface [217]. As the compact region grows, the increasing resistance limits the supply of water and thus the evaporation rate [217]. This increasing resistance effect is much larger for smaller particles to flow because of the smaller pore size [218]. Air penetrates into the bed due to slower water flow which dries the bed and introduces stress in the bed that results in crack generation.

When 5% aqueous suspensions of 50 nm silica particles were used for packing, the cracks began to form in the separation channel close to reservoir 4, which was left open to induce the packing as illustrated in Figure 5-3a. The time needed for smaller particles to pack is much longer than for larger particles. As a result the bed dries while the packing occurs. Organic solvents can accelerate the evaporation rate and as a result cause a faster transport and faster packing rate. In this way, cracks may not have enough time to form. To address the issue, methanol solvent was added to the colloidal suspension to accelerate the packing. To further control the drying the chip was kept in a humidity chamber during packing (Figure 5-4).

a

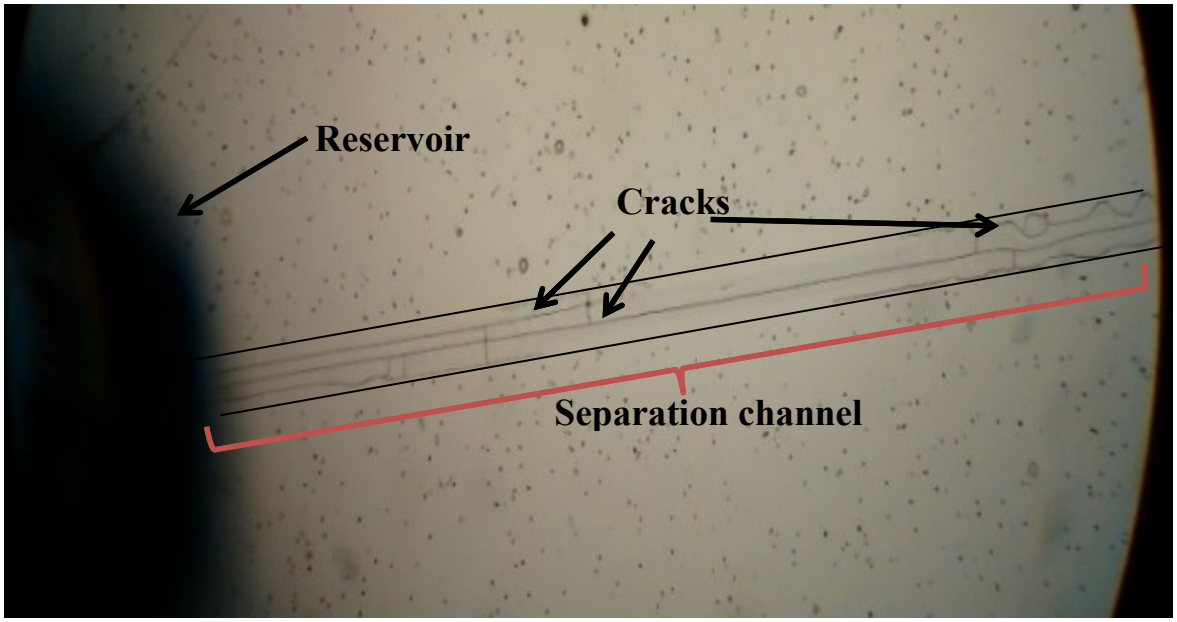

b

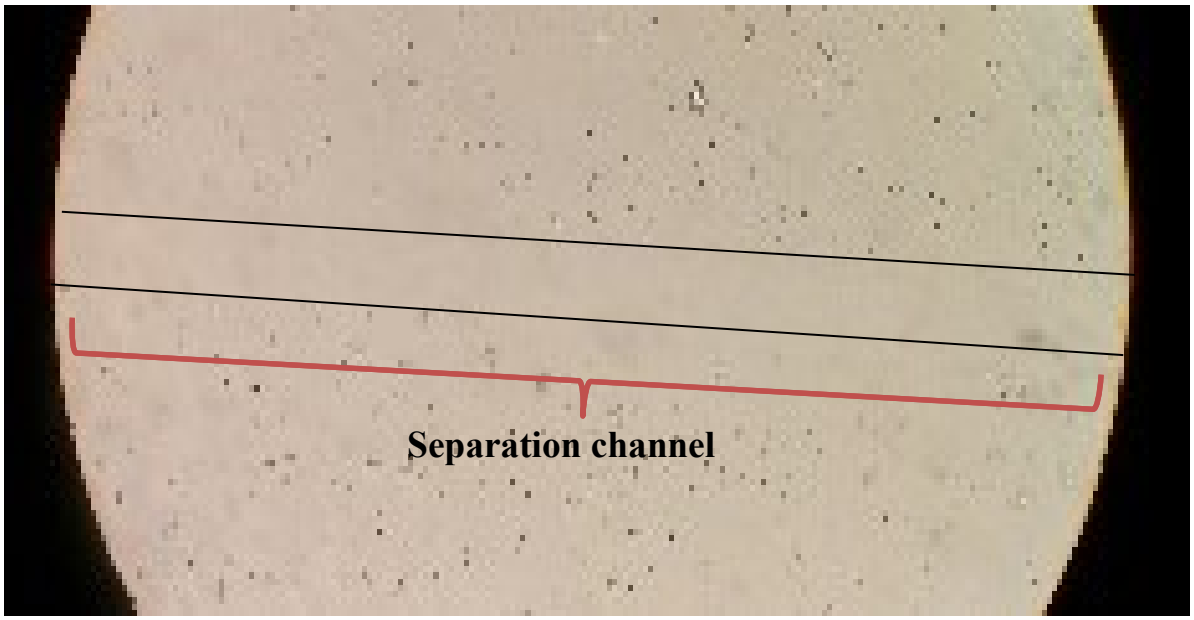

Figure 5-3. Micrograph of a PDMS microchannel and the CSA of a 50 nm silica particles growing with micro-cracks a) 5% colloidal suspension used for packing b) 25% methanol added to colloidal suspension.

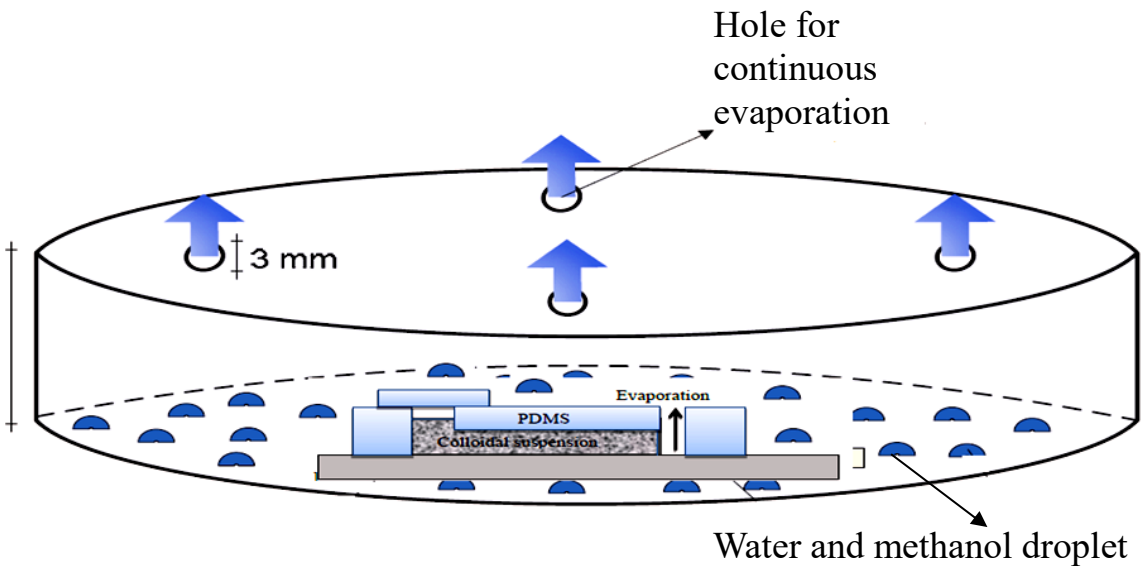

Figure 5-4. Schematic diagram of the microfluidic approach for the fabrication of the 50 nm silica particles.

Figure 5-3b demonstrates that when 25% v:v methanol was added to the aqueous suspensions of 50 nm silica nanoparticles (%5 w/v) the organic solvent helped produces a crack free packing.

Although we used methanol to accelerate colloidal crystal growth and avoid crack formation, the growth stopped at the double-T intersection on the chip, and it took a long time reach the intersection. Hence the colloidal suspension was removed from the reservoirs 1, 2, and 3 and replaced by aqueous suspensions of 150 nm silica nanoparticles (5% w/v). This approach allowed packing of all the channels in a faster, more effective way, producing the structure shown by cartoon in Figure 5-5. The larger pore size has the benefit of fastest protein transport during sample loading, as well.

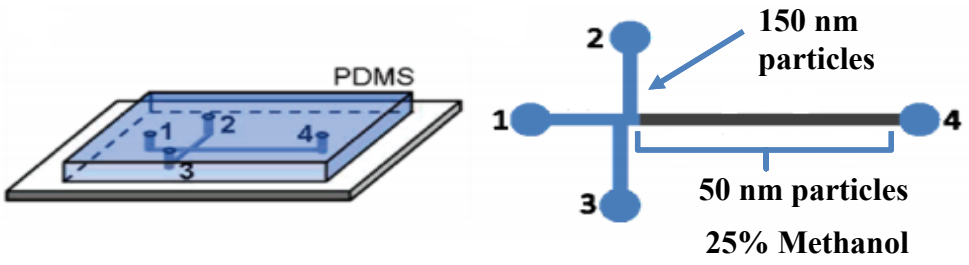

Figure 5-5. Schematic presentation of the microfluidic chip. Colloidal gradient along the microchannel. Schematic of the microfluidic chip and crystal along with two different particle sizes.

A more detailed study of the effect of adding methanol to the particle suspension was then performed. Microfluidic colloidal crystal growth was initiated via injection of 10 µL of the colloidal dispersion in a reservoir and microfluidic 10 µm channel. The advance of the compaction front was observed via the inherent difference between the indices of refraction of the regions with high volume fraction of packed particles compared to the dispersion regimes which have lower particle volume fraction, as depicted in Figure 5-6. The results in Figure 5-7 show that as the length of the nanoporous media increases with time, a decrease in the rate of growth is observed. On the basis of the Dufresne et al. [217] model, the dynamic growth of the structure can be correlated with two parameters, the length, y, and time, t. The length, y, represents the crystal length at which the rate of transport of water through the compacted region now controls the rate of evaporation and hence the rate of crystal growth. Using the analysis of Dufresne et al., [217] a curve-fit of the growth−time curve to a power law, $y \sim t^{a}$, shows a decrease in the exponential power as a result of methanol% (Figure 5-7). Data shown in Figure 5-7 were fitted to a $y \sim t^{a}$ function. When the methanol percentage increased the rate of packing increased and the function increased. For example, when 0% methanol

was added to the colloidal suspension the function was 0.62 which is comparable to previous work [41] and increased to 0.76 for 25% methanol. Figure 5-7 makes it very clear methanol substantially speeds up growth of the particle beds.

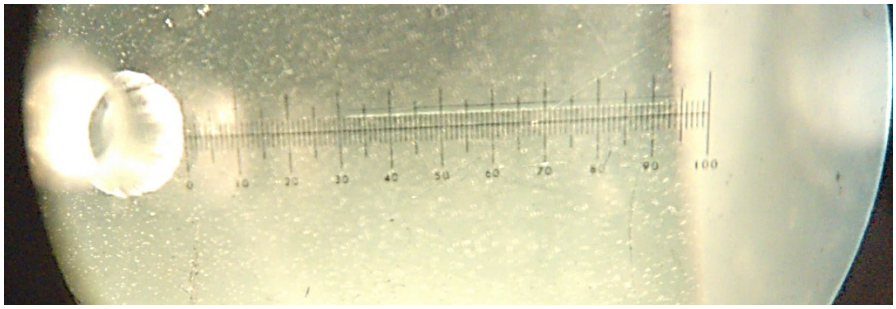

Figure 5-6. Optical micrograph of crystal growth of 50 nm silica particles in microchannel.

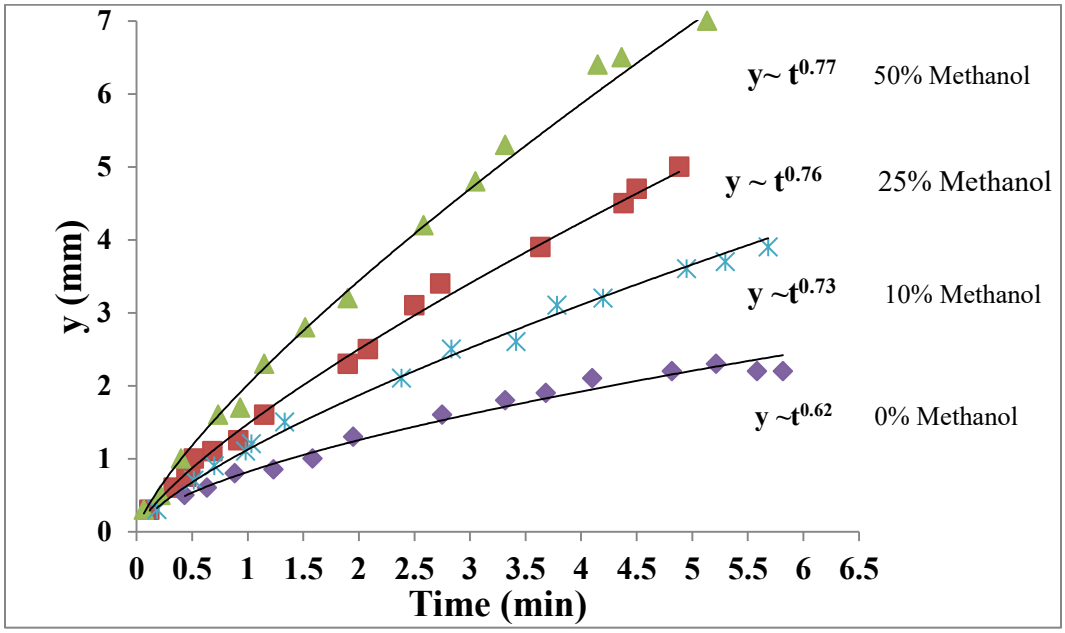

Figure 5-7. Microfluidic crystal growth behavior of silica naoparticles. a) Solid lines are $y \sim t^{a}$ functions.

5.2.1 Characterization of stabilized 50 nm particles CSA structure

A HEMA/EDMA polymer mixture was photopolymerized in the 50 nm particle beds to stabilize the structure at high voltage. Table 5-2 illustrate the voltages that could be achieved at different monomer concentration. It was observed that increasing the monomer concentration from 0% to 0.09% resulted in increasing the electric field stability of the bed. The stability decreased for 0.2%, presumably due to the increasing coating thickness, which disrupted the lattice and made it easier for particles to be mobilized by the field.

Table 5-2. The monomer% vs. and Electric field stability.

Monomer%	Electric field stability
0	30 V/cm
0.01	520 V/cm
0.09	1250 V/cm
0.2	1080 V/cm

5.3 Characterization of Colloidal Crystals of 50nm Silica Particles

Suspensions of 50 nm silica particles with 0, 10, 25, and 50% methanol were used to fabricate ordered packed structures inside the separation channel in the microfluidic device. The packed bed was then entrapped with monomer solution (0.09%). SEM images of these structures revealed they were not highly ordered. For SEM observation,

packed chips were dried completely and the PDMS layer was peeled off before sputtering with an Au metal layer. Using the self-assembly approach and monodisperse particle suspensions, uniform ordered structures are fabricated for particles ≥ 150 nm. The structures of top view of the separation channels are shown in Figure 5-8 as an example. Adding 25% methanol to the colloidal suspension did not appear to significantly change the order of the structure, compared to 0% methanol [215] (Figure 5-8a,b). The SEM image of 0% methanol was captured from the crack free area of the bed and the chip kept in the humidity chamber and packed for longer time than 25% methanol.

Figure 5-8c,d shows the stabilized 50 nm particle packed bed after stabilization with a 0.09 monomer solution. The images show no obvious changes in crystalline structure. It was feasible to obtain images from a wide area of the chip compared to a native packed bed. During SEM imaging we found that the native silica particles move and it was hard to focus the ion beam, but after stabilization we did not see this issue. As a result of these observations we settled on using 25% methanol added to the colloidal suspension to accelerate the packing and avoid visible cracks formation, followed by stabilization of bed by 0.09% HEMA/EDMA monomer solution.

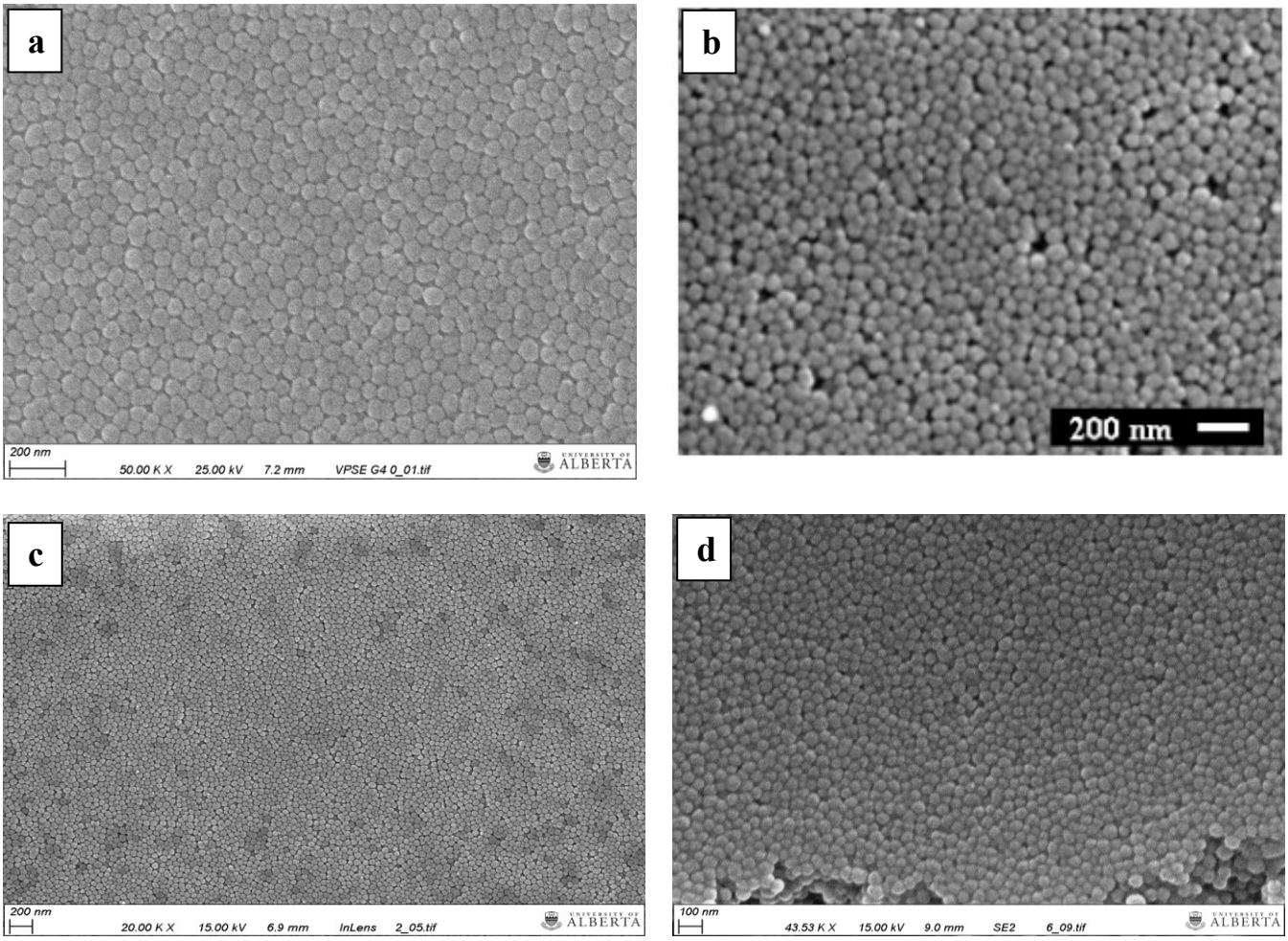

Figure 5-8. SEM images of self-assembled structures of 50 nm silica particles a) 50 nm, 25% methanol. b) 50 nm, 0% methanol from [215], and c,d) stabilized 50 nm, 25% methanol, 0.09% HEMA/EDMA monomer.

Ali et al. [215] calculated the radial distribution function (RDF) based on the image analysis of the top-down SEM images of the nanoporous media (Figure 5-9). RDF embodies information regarding long range interparticle organization [142,219,220] and is used as a geometrical characterization of the CSA of 310 and 50 nm particles based on their top-down SEM images [215]. The center coordinates of the particles were measured in ImageJ software and used to calculate the RDFs. Furthermore, local structural order was

captured by the global orientational order parameter [142], ψ. Results and are shown for each structure in Figure 5-9 [215]. Crystals of 310 nm shows structural order based on the magnitude and number of sharp peaks in their RDF plots. However, RDFs of the nanoporous structures of 50 nm do not have as many peaks as the model reference crystal and also the magnitude of their peaks is quite shallow. In current study the same trend was observed for 310 and 50 nm nanoporous structures based on SEM images and the value of ψ obtained.

Huang and Pemberton's [214] studies of sub-100 nm silica particles showed better structural order for 53 ± 9.5% nm than that fabricated in this study for 50 nm. The polydispersity in their studies was lower, 9.5%, compared to the value of 10.48 ± 1.27% in [215]. Hence it can be concluded that polydispersity values higher than 8% reduce the lattice order, as pointed out by Jiang et al. [221]. In this work we used 50 nm silica particles with same polydispersity of 10.48 ± 1.27% as in [215]. The higher polydispersity means that the lattice order was reduced.

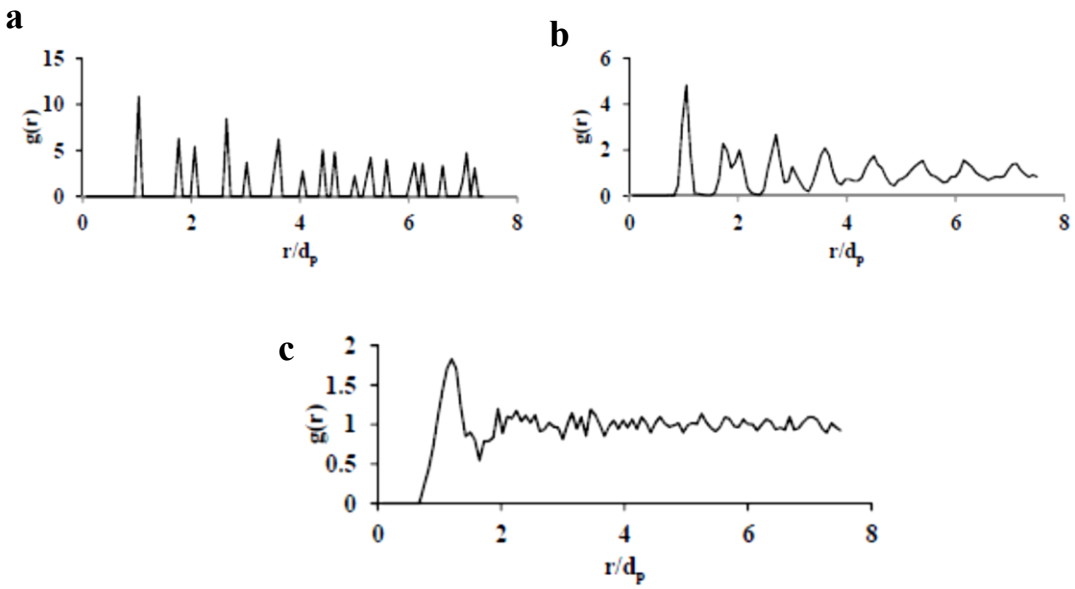

Figure 5-9. Profile of the radial distribution function of the colloidal crystals, g(r). a) Ideal hexagonally closed-packed (ψ=1). b) 310 nm (ψ=0.93±0.015). c) 50 nm (ψ=0.42±0.06) [215].

5.4 Separation of SDS-Denatured Proteins

Native 50 nm silica nanoparticle packed beds are stable at a low voltage (<30 V /cm) due to the existence of van der Waals forces and/or hydrogen bonds. An electropherogram of SDS denatured ovalbumin (45 kDa) and BSA (66 kDa) separation at 30 V/cm as observed at 4 mm in an CSA of 50 nm silica particles is shown in Figure 5-10 [215]. The peaks are broad, separation is slow (300 s), and the separation efficiency is not good.

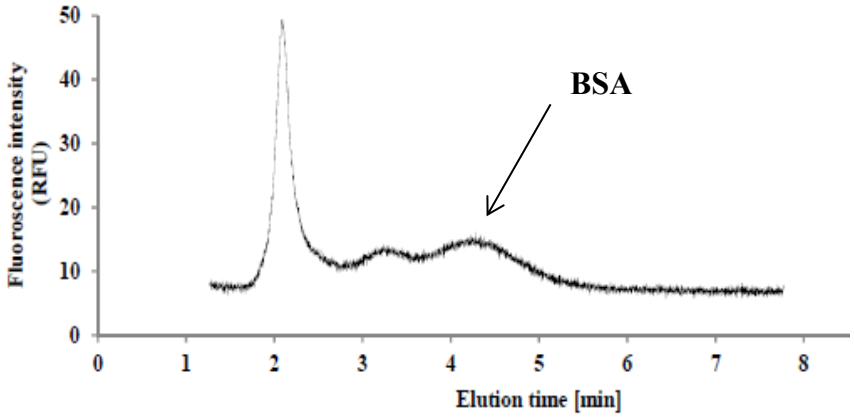

Figure 5-10. a) Electropherograms of FITC, ovalbumin (45 kDa) and BSA (66 kDa) separation at 30 V/cm as observed at 4 mm in CSA of 50 nm silica particles [215].

The stabilized beds were studied with various analytes. Figure 5-11a shows electropherograms of fluorescein dye at a detection length (L_d) of 2 mm, using different electric field strengths. The fluorescein dye peaks become sharper the electric field increases as expected. The figure also shows that the polymer entrapped column can withstand electric fields up to 1250V/cm, which is significantly higher than native 50 nm silica beds with no entrapment, for which ~30 V/cm is the limit [38]. The electric field versus migration rate is shown in Figure 5-11b, showing reasonable linearity up to 1250 V/cm. At 1300 V/cm the migration rate increased, showing the bed cannot tolerate more than 1250 V/cm.

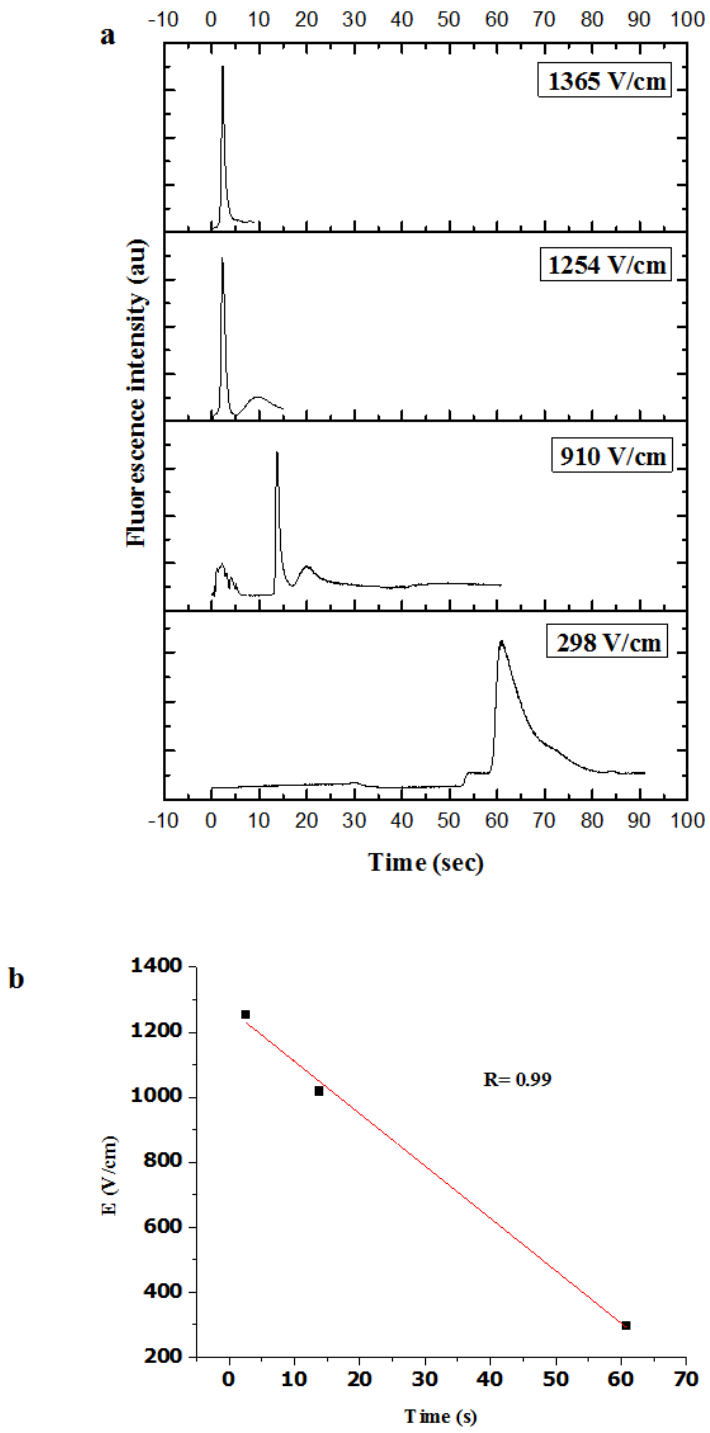

Figure 5-11. a) Electropherogram of fluorescein dye at increasing field strength, 310nm silica particle CSA in 2mm long bed entrapped with photopolymerized 0.09% monomer solution, using 4× TBE buffer (pH 8.3), (L_d) of 13 mm.b) b) plot of electric field vs. migration time.

Figure 5-12a shows electropherograms of a mixture of two FITC-labeled SDS denatured proteins: aprotinin (MW 6.5 kDa) and trypsin inhibitor (MW 20.1 kDa) detected at a separation length (L_d) of 3 mm and electric field of 1250 V/cm. The protein migration times increase with molecular weight, as determined by injecting each protein separately. Ready baseline separation of insulin (MW 5.8 kDa) and lysozyme (MW 14 kDa) SDS denatured was accomplished in less than 6 s for the separation conditions shown in Figure 5-12b: separation length (L_d) of 5 mm, electric field 1000 V/cm. Plate heights of 90 nm and 72 nm were achieved for insulin and lysozyme, respectively.

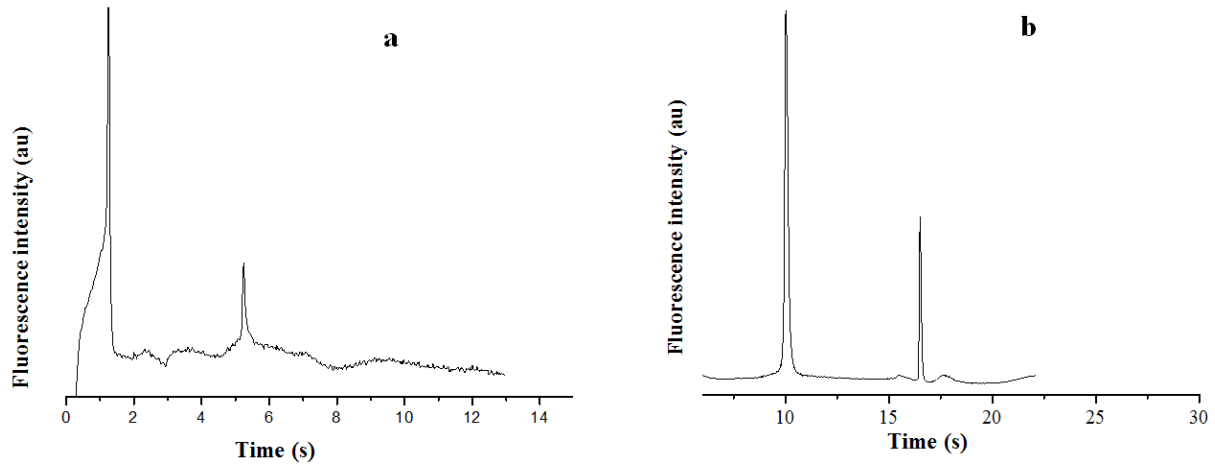

Figure 5-12. a) Electropherograms of aprotinin (6.5 kDa) and trypsin inhibitor (20 kDa)-SDS denatured separation at 1250 V/cm, L_d = 3 mm, 50 nm CSA stabilized with 0.08% HEMA/EDMA.b) Electropherograms of insulin (5.8 kDa) and lysozyme (14 kDa)-SDS denatured separation 1000 V/cm, L_d =5 mm, 50 nm CSA stabilized with 0.09% HEMA/EDMA.

To evaluate the stabilized 50 nm particle beds and comparing the result to previous work, BSA (66 kDa) was used. Figure 5-13 shows only BSA peak after immobilization of particles, BSA peaks get sharper and detected in 20 sec. The plate height of 38.3 µm is calculated in [215] for BSA and plate height of 1.4 µm was obtained in this work. The smaller plate height shows that the separation efficiency has been improved.

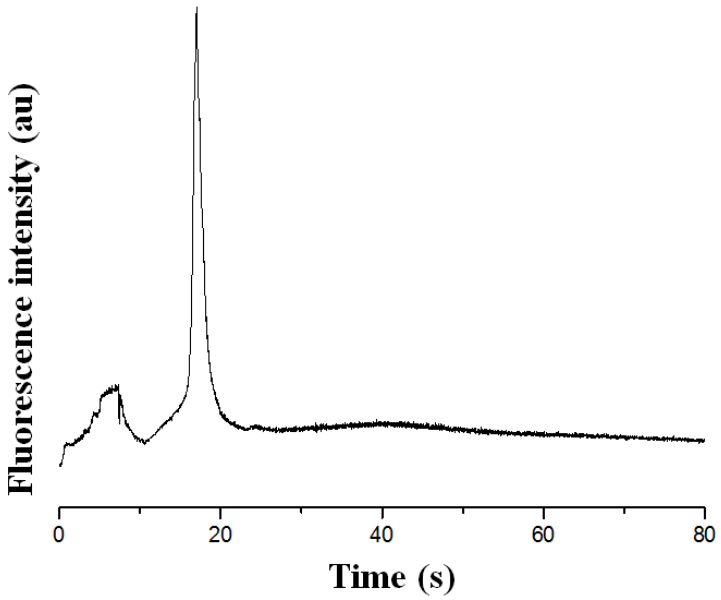

Figure 5-13. Electropherograms of BSA (66 kDa) separation at 615 V/cm, L_d =3 mm, 50 nm CSA stabilized with 0.09% HEMA/EDMA.

5.5 Conclusion

Crack free 50 nm CSA packed beds were obtained and the process of packing was discussed. Beds stabilized using photopolymerization of methacrylates were assessed with SEM imaging. The entrapment of CSA silica nanoparticles in microfluidic devices results in a highly stable structure, however SEM shows the crystallinity is not high. This polymer entrapment technique improved the stability of the CSA structure at high electric fields (up to at least 1,200 V/cm) allowing fast and highly efficient separation of SDS-denatured proteins with a plate height of 72 nm. The plate height of 93 nm achieved for same protein on 310 nm stabilized bed which shows separation efficiency improvement on stabilized 50 nm silica bed. Photopolymerization of methacrylates is a rapid, facile fabrication method for the stabilization of sub-micron scale CSA particle.

CHAPTER 6: CONCLUSION AND FUTURE WORK

6.1 Summary of the thesis

The colloidal self-assembled (CSA) bed was stabilized using photopolymerization of methacrylates and the entrapped bed was assessed with different techniques of imaging and non-imaging. The results showed that the entrapment of CSA silica nanoparticles in microfluidic devices results in a highly stable crystalline structure. These structures are fused together with minimal amounts of organic polymer in a web-like formation. Photopolymerization of methacrylates is a rapid, facile fabrication method for the stabilization of sub-micron scale CSA particle beds, retaining a high degree of order and packing quality upon polymerization. This polymer entrapment technique improved the stability of the CSA structure at high electric fields (up to at least 1,800 V/cm) allowing fast and highly efficient separation performance. The results presented demonstrate the flexibility and high reproducibility of this entrapped CSA bed methodology for protein separation across a wide size range. For a separation length of 13 mm, plate numbers of more than 10^6/m, with associated plate heights around 56 nm were observed for SDS denatured proteins. The study demonstrates the potential of CSA nanoparticles beds in microchips for ultra-fast separations. The ability to separate close molecular weight proteins (ΔM = 0.6 kDa) in such short separation lengths will be valuable for biomolecular separations in microfluidic devices.

Chapter 4 described the method and the processes required to photograft HEMA (2-hydroxyethyl methacrylate) coated CSA beds by META ([2-(methacryloyloxy) ethyl] trimethylammonium chloride) and SBMA (sulfobetaine methacrylate) functional polymer. Photo-initiated polymerization enabled coating the nanoparticles in microfluidic devices, and the surface chemistry was then tailored to fit the specific application by subsequent photografting of the surface. This coating strategy allows fast, robust, wall coatings with controlled surface chemistry and surface biocompatibility. The surface was characterized by energy-dispersive X-ray spectroscopy (EDX), X-ray photoelectron spectroscopy (XPS), and IR spectroscopy. In addition, electroosmotic flow was measured for both (META and SBMA) grafted surfaces. In both acidic and basic protein separations, the appropriate polymer coating and grafting layers showed good efficiency and reproducibility and improved separation of native particles compared to HEMA coated particle beds.

A 50 nm CSA bed was also stabilized using photopolymaerization of methacrylates and the entrapped bed was assessed with SEM imaging and by separation performance. This polymer entrapment technique improved the stability of the CSA structure at high electric fields (up to at least 1,200 V/cm) allowing fast and highly efficient separation performance.

To summarize, this thesis represents a facile method of entrapment and functionalization of CSA silica nanoparticle beds for size based and native proteins separation. This fast, simple, and robust technique of entrapment allows new applications in academic communities and industry.

6.2 Future work

6.2.1 Quantitative impurity analysis of monoclonal antibody size heterogeneity on microfluidics chip

The characteristics of physical, chemical, or biological properties of a protein product depend on their manufacture, and require specification and measurement in order to ensure the desired product quality. These properties are called Critical quality attributes (CQAs) [67]. Recombinant monoclonal antibody (rMAb) fragments, aggregates, and host cell impurities are potential CQAs monitored during clinical and commercial manufacture to ensure patient safety and product efficacy [67]. Among them, monoclonal antibodies (MAb) have become the most rapidly growing class of biopharmaceutical products [222]. Therefore, developing robust analytical methods for monitoring CQAs is crucial to control quality throughout the product lifecycle [67].

The major drawbacks of conventional SDS-PAGE are its inconvenience in data analysis, the irreproducibility associated with the staining/ destaining steps used in analyte detection, the use of toxic reagents, and high mobility variability. In addition, mechanical instability of gel at high electric field results in a long separation time and low separation efficiency. Replacement technologies to monitor CQA would be beneficial.

The emerging technique of capillary electrophoresis (CE) and microfluidics show many advantages over classical SDS-PAGE including on-column direct UV or fluorescence detection, automation, enhanced resolution and reproducibility, and accurate quantification of proteins and molecular weight determination [223]. UV absorbance is a

common detector in CE-SDS; however, the sensitivity is low due to the short optical path length across the capillaries. Hunt and Nashabeh [224] demonstrated that precolumn labeling of recombinant protein products with 5-carboxytetramethylrhodamine succinimidyl ester (5-TAMRA.SE) and laser-induced fluorescence (LIF) detection can be used for CE-SDS analyses as a replacement for silver-stained SDS-PAGE to detect low-level impurities and MAb size variants and to determine lot-to-lot consistency.

There is a potential to apply our stabilized CSA bed of 310 and 50 nm silica nanoparticles to develop a method for monitoring potential CQAs (process and product impurities) as they relate to size heterogeneity of therapeutic proteins. By reducing disulfide linkages, the method detects light chain (LC), heavy chain (HC), and HC glycosylation (Figure 6-1). Therefore replacing a polymer matrix with stabilized silica nanoparticles CSA in microchannel can improve the current resolving power of CE-SDS and can be developed into a commercial IgG Purity/Heterogeneity assay.

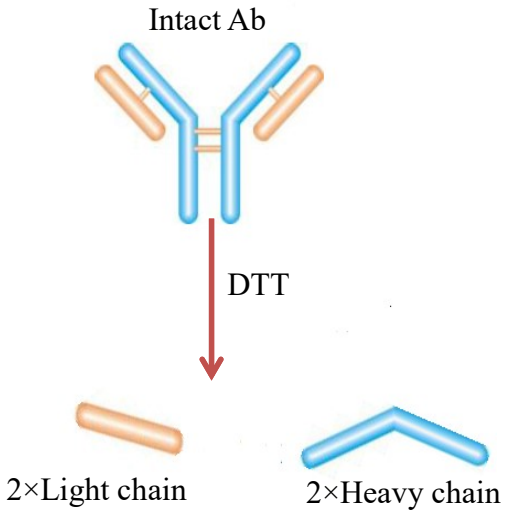

Figure 6-1. Schematic illustrations of antibody fragment generation by DTT (dithiothreitol) reduction.

Figure 6-2 shows electropherogram separations of non-reduced (a) and reduced (b) forms of IgG sample on our chip with stabilized 310 nm particle packed bed. The samples were labeled with fluorescein isothiocyanate (FITC).

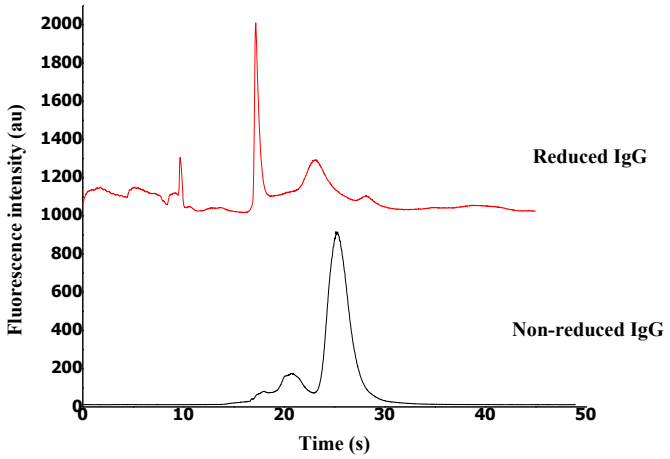

Figure 6-2. Electropherogram separations of nonreduced (a) and reduced (b) of IgG sample stabilized 310 nm particles.

The preliminary experiment demonstrates the possibility of employing the stabilize CSA bed for separation and detection of IgG fragmentations. Key to the success of this method relies on optimization of sample prep and fluorescent derivatization parameters. As future work the labeling parameters need to be optimized, such as choosing a suitable dye, dye-to-protein (D/P) ratio, labeling temperature and time. In addition we need to ensure detection limits suitable for low-level impurities. Also we should explore if better separation will be obtained by using a stabilized 50 nm CSA bed. After the optimization studies are completed and a thorough understanding of the method is obtained, validation studies will be performed according to the guidelines of the International Committee on Harmonization (ICH).

6.2.2 Trypsin digestion and peptide separation on chip

Peptide mass mapping is one of the routine methods that is commonly used to determine both protein identity and posttranslational modifications [225]. The method typically involves the digestion of the protein of interest by a proteolytic enzyme, e.g. trypsin, in free solution, followed by Mass identification of the resulting peptides. The most commonly method is using free solution protein digestion, the reaction time is typically 24 hours [226]. The immobilization of trypsin enzyme on the solid surface can accelerate this process. The HEMA coated silica nanoparticle beds can be an ideal solid support for trypsin immobilization because of its large surface area, permeability, hydrophilic nature, chemical, and mechanical stability. Also, the small pore sizes mean mass transfer to the enzyme should be rapid.

The schematic of the proposed chip is show in Figure 6-3. The protein is injected from reservoir 2 and will be digested in the channel on the trypsin enzyme immobilized particle surface. The peptides are injected into the separation microchannel, in which the particles are functionalized with SBMA. Finally the outlet of chip will be coupled to mass spectrometer for identification.

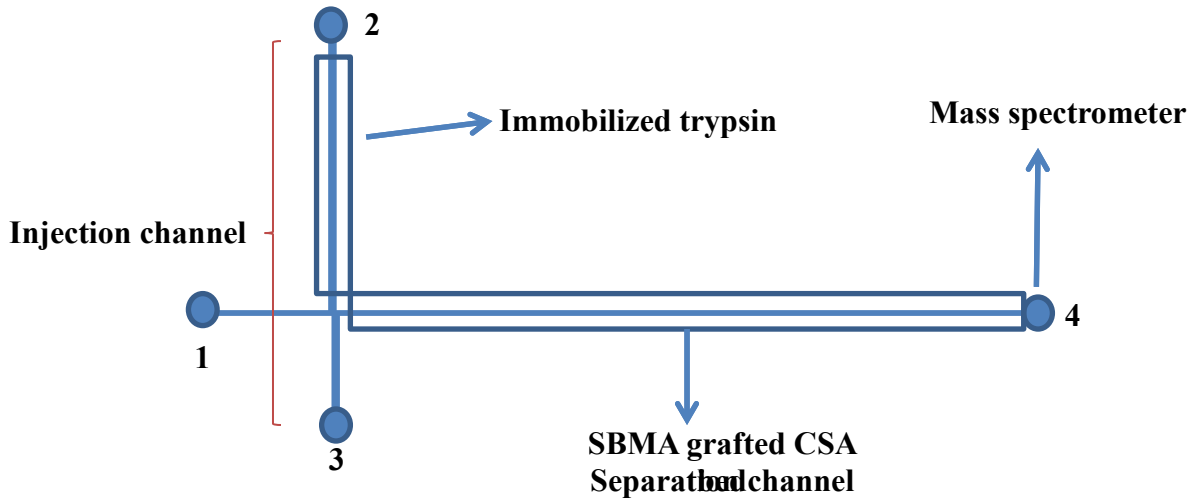

Figure 6-3. Schematic of 1D-chip for enzymatic digestion and peptide separation.

In general, possible real applications of entrapped CSA silica particle beds were discussed as future works. This includes quantitative impurity analysis of monoclonal antibody, fast trypsin digestion and peptide separation on chip.

REFERENCES

1. Dorfman, K. D., King, S. B., Olson, D. W., Thomas, J. D. P. & Tree, D. R. Beyond gel electrophoresis: Microfluidic separations, fluorescence burst analysis, and DNA stretching. *Chem. Rev.* **113,** 2584–2667 (2013).
2. Egas, D. A. & Wirth, M. J. Fundamentals of protein separations: 50 years of nanotechnology, and growing. *Annu. Rev. Anal. Chem.* **1,** 833–855 (2008).
3. Chung, M., Kim, D. & Herr, A. E. Polymer sieving matrices in microanalytical electrophoresis. *Analyst* **139,** 5635–5654 (2014).
4. Manz, A., Widmers, H. M. & Graber, N. Miniaturized total chemical analysis systems: A novel concept for chemical sensing. *Sensors Actuators B Chem.* **1,** 244–248 (1990).
5. Harrison, D. J. *et al.* Micromachining a Miniaturized Capillary Electrophoresis-Based Chemical-Analysis System on a Chip. *Science (80-.).* **261,** 895–897 (1993).
6. Chiem, N. & Harrison, D. J. Microchip-based capillary electrophoresis for immunoassays: Analysis of monoclonal antibodies and theophylline. *Anal. Chem.* **69,** 373–378 (1997).
7. Fluri, K., Fitzpatrick, G., Chiem, N. & Harrison, D. J. Integrated capillary electrophoresis devices with an efficient postcolumn reactor in planar quartz and glass chips. *Anal. Chem.* **68,** 4285–4290 (1996).
8. Liang, Z. *et al.* Microfabrication of a Planar Absorbance and Fluorescence Cell for Integrated Capillary Electrophoresis Devices. *Anal. Chem.* **68,** 1040–1046 (1996).
9. Khandurina, J., Jacobson, S. C., Waters, L. C., Foote, R. S. & Ramsey, J. M. Microfabricated porous membrane structure for sample concentration and electrophoretic analysis. *Anal. Chem.* **71,** 1815–1819 (1999).
10. Kutter, J. P., Jacobson, S. C., Matsubara, N. & Ramsey, J. M. Solvent-programmed microchip open-channel electrochromatography. *Anal. Chem.* **70,** 3291–3297 (1998).
11. Jacobson, S. C., Culbertson, C. T., Daler, J. E. & Ramsey, J. M. Microchip structures for submillisecond electrophoresis. *Anal. Chem.* **70,** 3476–3480 (1998).
12. Liu, S., Shi, Y., Ja, W. W. & Mathies, R. A. Optimization of high-speed DNA

sequencing on microfabricated capillary electrophoresis channels. *Anal. Chem.* **71,** 566–573 (1999).

13. Woolley, A. T. & Mathies, R. a. Ultra-High-Speed DNA Sequencing Using Capillary Electrophoresis Chips. *Anal. Chem.* **67,** 3676–3680 (1995).
14. Simpson, P. C. *et al.* High-throughput genetic analysis using microfabricated 96-sample capillary array electrophoresis microplates. *Proc. Natl. Acad. Sci.* **95,** 2256–2261 (1998).
15. Sia, S. K. & Whitesides, G. M. Microfluidic devices fabricated in poly(dimethylsiloxane) for biological studies. *Electrophoresis* **24,** 3563–3576 (2003).
16. Mcdonald, J. C., Duffy, D. C., Anderson, J. R. & Chiu, D. T. Review - Fabrication of microfluidic systems in poly (dimethylsiloxane). *Electrophoresis* **21,** 27–40 (2000).
17. McDonald, J. C. & Whitesides, G. M. Poly (dimethylsiloxane) as a Material for Fabricating Microfluidic Devices. *Acc. Chem. Res.* **35,** 491–499 (2002).
18. Giordano, B. C., Jin, L., Couch, A. J., Ferrance, J. P. & Landers, J. P. Microchip laser-induced fluorescence detection of proteins at submicrogram per milliliter levels mediated by dynamic labeling under pseudonative conditions. *Anal. Chem.* **76,** 4705–4714 (2004).
19. Phillips, T. M. Rapid analysis of inflammatory cytokines in cerebrospinal fluid using chip-based immunoaffinity electrophoresis. *Electrophoresis* **25,** 1652–9 (2004).
20. Roper, M. G., Shackman, J. G., Dahlgren, G. M. & Kennedy, R. T. Microfluidic chip for continuous monitoring of hormone secretion from live cells using an electrophoresis-based immunoassay. *Anal. Chem.* **75,** 4711–4717 (2003).
21. Colyer, C. L., Mangru, S. D. & Harrison, D. J. Microchip-based capillary electrophoresis of human serum proteins. *J. Chromatogr. A* **781,** 271–276 (1997).
22. Uthayakumaran, S., Batey, I. L. & Wrigley, C. W. On-the-spot identification of grain variety and wheat-quality type by Lab-on-a-chip capillary electrophoresis. *J. Cereal Sci.* **41,** 371–374 (2005).
23. Monti, G. *et al.* Monitoring food quality by microfluidic electrophoresis, gas

chromatography, and mass spectrometry techniques: Effects of aquaculture on the sea bass (Dicentrarchus labrax). *Anal. Chem.* **77,** 2587–2594 (2005).

24. Schulze, P., Ludwig, M., Kohler, F. & Belder, D. Deep UV Laser-Induced Fluorescence Detection of Unlabeled Drugs and Proteins in Microchip Electrophoresis Deep UV Laser-Induced Fluorescence Detection of Unlabeled Drugs and Proteins in Microchip Electrophoresis. *Anal. Chem.* **77,** 2178–2182 (2005).
25. Uthayakumaran, S., Listiohadi, Y., Baratta, M., Batey, I. L. & Wrigley, C. W. Rapid identification and quantitation of high-molecular-weight glutenin subunits. *J. Cereal Sci.* **44,** 34–39 (2006).
26. Kustos, I., Nyul, A., Lorand, T., Kocsis, B. & Kilar, F. Effect of antifungal agents on protein composition of Candida albicans studied by capillary electrophoresis and chip technology. *J. Biochem. Biophys. Methods* **69,** 57–65 (2006).
27. Sarkar, P. K., Prajapati, P. K., Shukla, V. J., Ravishankar, B. & Choudhary, A. K. Toxicity and recovery studies of two ayurvedic preparations of iron. *Indian J. Exp. Biol.* **47,** 987–992 (2009).
28. Tabuchi, M., Kuramitsu, Y., Nakamura, K. & Baba, Y. Rapid subpicogram protein detection on a microchip without denaturing. *J. Proteome Res.* **2,** 431–435 (2003).
29. Volkmuth, W. D. & Austin, R. H. DNA electrophoresis in microlithographic arrays. *Nature* **358,** 600–692 (1992).
30. Han, J., Fu, J. & Schoch, R. B. Molecular sieving using nanofilters: past, present and future. *Lab Chip* **8,** 23–33 (2008).
31. Xuan, J. & Lee, M. L. Size separation of biomolecules and bioparticles using micro/nanofabricated structures. *Anal. Methods* **6,** 27–37 (2014).
32. El-Safty, S. A. Designs for size-exclusion separation of macromolecules by densely-engineered mesofilters. *Trends in Anal. Chem.* **30,** 447–458 (2011).
33. Fu, J., Mao, P. & Han, J. Artificial molecular sieves and filters: a new paradigm for biomolecule separation. *Trends Biotechnol.* **26,** 311–320 (2008).
34. Han, J. & Craighead, H. G. Separation of long DNA molecules in a microfabricated entropic trap array. *Science (80-.).* **288,** 1026–1029 (2000).
35. Huang, L. R., Cox E.C., Austin R.H. & Sturm, J. C. Continuous particle

separation through deterministic lateral displacement. *Science (80-.).* **304,** 987–990 (2004).

36. Baba, M. *et al.* DNA size separation using artificially nanostructured matrix. *Appl. Phys. Lett.* **83,** 1468–1470 (2003).
37. Roy, P. *et al.* Size-selective separation of macromolecules by nanochannel titania membrane with self-cleaning (declogging) ability. *J. Am. Chem. Soc.* **132,** 7893–7895 (2010).
38. Zeng, Y. & Harrison, D. J. Self-assembled colloidal arrays as three-dimensional nanofluidic sieves for separation of biomolecules on microchips. *Anal. Chem.* **79,** 2289–2295 (2007).
39. Nazemifard, N., Bhattacharjee, S., Masliyah, J. H. & Jed Harrison, D. DNA dynamics in nanoscale confinement under asymmetric pulsed field electrophoresis. *Angew. Chemie - Int. Ed.* **49,** 3326–3329 (2010).
40. Zeng, Y., He, M. & Harrison, D. J. Microfluidic self-patterning of large-scale crystalline nanoarrays for high-throughput continuous DNA fractionation. *Angew. Chem., Int. Ed.* **47,** 6388–6391 (2008).
41. Malekpourkoupaei, A., Kostiuk, L. W. & Harrison, D. J. Fabrication of binary opal lattices in microfluidic devices. *Chem. Mater.* **25,** 3808–3815 (2013).
42. Wei, B., Malkin, D. S. & Wirth, M. J. Plate heights below 50 nm for protein electrochromatography using silica colloidal crystals. *Anal. Chem.* **82,** 10216–10221 (2010).
43. Birdsall, R. E., Koshell, B. M., Hua, Y., Ratnayaka, S. N. & Wirth, M. J. Modeling of protein electrophoresis in silica colloidal crystals having brush layers of polyacrylamide. *Electrophoresis* **34,** 753–760 (2013).
44. Gong, M., Bohn, P. W. & Sweedler, J. V. Centrifugal sedimentation for selectively packing channels with silica microbeads in three-dimensional micro/nanofluidic devices. *Anal. Chem.* **81,** 2022–2026 (2009).
45. Park, J. *et al.* Fully packed capillary electrochromatographic microchip with self-assembly colloidal silica beads. *Anal. Chem.* **79,** 3214–3219 (2007).
46. van Deemter, J. J., Zuiderweg, F. J. & Klinkenberg, A. Longitudinal diffussion and resistance to mass transfer as causes of noideality in chromatography. *Chem. Eng.*

Sci. **5,** 271 (1956).

47. Fonslow, B. R. *et al.* Protein Separation by Capillary Gel Electrophoresis: A Review. *Anal. Chem.* **10,** 54–56 (2013).
48. Sun, L., Zhu, G., Yan, X., Dovinchi, N. Plate heights below 50 nm for protein electrochromatography using silica colloidal crystals. *Proteomics* **4,** 622–628 (2011).
49. Effenhauser, C. S., Paulus, A., Manz, A. & Widmer, H. M. High-speed separation of antisense oligonucleotides on a micromachined capillary electrophoresis device. *Anal. Chem.* **66,** 2949–2953 (1994).
50. Herr, A. E. & Singh, A. K. Photopolymerized cross-linked polyacrylamide gels for on-chip protein sizing. *Anal. Chem.* **76,** 4727–4733 (2004).
51. Nagata, H., Tabuchi, M., Hirano, K. & Baba, Y. Microchip electrophoretic protein separation using electroosmotic flow induced by dynamic sodium dodecyl sulfate-coating of uncoated plastic chips. *Electrophoresis* **26,** 2247–2253 (2005).
52. Liu, J., Yang, S., Lee, C. S. & DeVoe, D. L. Polyacrylamide gel plugs enabling 2-D microfluidic protein separations via isoelectric focusing and multiplexed sodium dodecyl sulfate gel electrophoresis. *Electrophoresis* **29,** 2241–2250 (2008).
53. Yang, S., Liu, J., Lee, C. S. & Devoe, D. L. Microfluidic 2-D PAGE using multifunctional in situ polyacrylamide gels and discontinuous buffers. *Lab Chip* **9,** 592–599 (2009).
54. Tentori, A. M., Hughes, A. J. & Herr, A. E. Microchamber integration unifies distinct separation modes for two-dimensional electrophoresis. *Anal. Chem.* **85,** 4538–4545 (2013).
55. Birdsall, R E., Koshel, B. M., Wirth, M. J. Modeling of protein electrophoresis in silica colloidal crystals having brush layers of polyacrylamide. *Electrophoresis* **34,** 753–760 (2013).
56. Guttman, A. & Nolan, J. Comparison of the separation of proteins by sodium dodecyl sulfate-slab gel electrophoresis and capillary sodium dodecyl sulfate-gel electrophoresis. *Analytical Biochemistry* **221,** 285–289 (1994).
57. Plieva, F., Huiting, X., Galaev, I. Y., Bergenstahl, B. & Mattiasson, B. Macroporous elastic polyacrylamide gels prepared at subzero temperatures: control

of porous structure. *J. Mater. Chem.* **16,** 4065 (2006).

58. Hjerten, S. High-performance electrophoresis: the electrophoretic counterpart of high-performance liquid chromatography. *J. Chromatogr. A* **270,** 1–6 (1983).
59. Kim, D., Karns, K., Tia, S. Q., He, M. & Herr, A. E. Electrostatic protein immobilization using charged polyacrylamide gels and cationic detergent microfluidic western blotting. *Anal. Chem.* **84,** 2533–2540 (2012).
60. Karns, K. & Herr, A. E. Human tear protein analysis enabled by an alkaline microfluidic homogeneous immunoassay. *Anal. Chem.* **83,** 8115–8122 (2011).
61. Tia, S. Q., He, M., Kim, D. & Herr, A. E. Multianalyte on-chip native western blotting. *Anal. Chem.* **83,** 3581–3588 (2011).
62. He, M. & Herr, A. E. Automated microfluidic protein immunoblotting. *Nat. Protoc.* **5,** 1844–1856 (2010).
63. Lo, C. T., Throckmorton, D. J., Singh, A. K. & Herr, A. E. Photopolymerized diffusion-defined polyacrylamide gradient gels for on-chip protein sizing. *Lab Chip* **8,** 1273–1279 (2008).
64. Herr, A. E., Throckmorton, D. J., Davenport, A. A. & Singh, A. K. On-chip native gel electrophoresis-based immunoassays for tetanus antibody and toxin. *Anal. Chem.* **77,** 585–590 (2005).
65. Hughes, A. J. & Herr, A. E. Microfluidic Western blotting. *Proc. Natl. Acad. Sci. U. S. A.* **109,** 21450–5 (2012).
66. Greiner, M., Technologies, A. & Lies, M. Capillary Electrophoresis. *Anal. Chem.* **61,** 24–25 (2012).
67. Michels, D. A., Parker, M. & Salas-Solano, O. Quantitative impurity analysis of monoclonal antibody size heterogeneity by CE-LIF: Example of development and validation through a quality-by-design framework. *Electrophoresis* **33,** 815–826 (2012).
68. Yu, C., Davey, M. H., Svec, F. & Frechet, J. M. J. Monolithic porous polymer for on-chip solid-phase extraction and preconcentration prepared by photoinitiated in situ polymerization within a microfluidic device. *Anal. Chem.* **73,** 5088–5096 (2001).
69. Peters, E. C., Petro, M., Svec, F. & Fréchet, J. M. J. Molded rigid polymer

monoliths as separation media for capillary electrochromatography. *Anal. Chem.* **70,** 2296–2302 (1998).

70. Cong, Y., Svec, F. & Frechet, J. M. J. Towards stationary phases for chromatography on a microchip: Molded porous polymer monoliths prepared in capillaries by photoinitiated in situ polymerization as separation media for electrochromatography. *Electrophoresis* **21,** 120–127 (2000).
71. Liang, Y., Zhang, L. & Zhang, Y. Recent advances in monolithic columns for protein and peptide separation by capillary liquid chromatography. *Anal. Bioanal. Chem.* **405,** 2095–2106 (2013).
72. Wu, R., Hu, L., Wang, F., Ye, M. & Zou, H. Recent development of monolithic stationary phases with emphasis on microscale chromatographic separation. *J. Chromatogr. A* **1184,** 369–392 (2008).
73. Podgornik, A. & Krajnc, N. L. Application of monoliths for bioparticle isolation. *J. Sep. Sci.* **35,** 3059–3072 (2012).
74. Zhang, Z. *et al.* A 'one step' approach for preparation of an octadecyl–silica hybrid monolithic column via a non-hydrolytic sol–gel (NHSG) method. *RSC Adv.* **3,** 22160 (2013).
75. Plieva, F. M., Andersson, J., Galaev, I. Y. & Mattiasson, B. Characterization of polyacrylamide based monolithic columns. *J. Sep. Sci.* **27,** 828–836 (2004).
76. Van De Meent, M. H. M., Eeltink, S. & De Jong, G. J. Potential of poly(styrene-co-divinylbenzene) monolithic columns for the LC-MS analysis of protein digests. *Anal. Bioanal. Chem.* **399,** 1845–1852 (2011).
77. Premstaller, a, Oberacher, H. & Huber, C. G. High-performance liquid chromatography-electrospray ionization mass spectrometry of single- and double-stranded nucleic acids using monolithic capillary columns. *Anal. Chem.* **72,** 4386–4393 (2000).
78. Lin, Z. *et al.* Monolithic column based on a poly(glycidyl methacrylate-co-4-vinylphenylboronic acid-co-ethylene dimethacrylate) copolymer for capillary liquid chromatography of small molecules and proteins. *J. Chromatogr. A* **1246,** 90–97 (2012).
79. Shultz, A. & Joshi, M. Kinetics of photoinitiated free radical polymerization. *J.*

Polym. Sci. Polym. **22,** 1753–1771 (1984).

80. Hoyle, C. E. & Kinstle, J. F. in *ACS Symposium Series* (American Chemical Society, 1990). doi:10.1021/bk-1990-0417
81. Guo, C., Zhou, L. & Lv, J. Effects of expandable graphite and modified ammonium polyphosphate on the flame-retardant and mechanical properties of wood flour-polypropylene composites. *Polym. Polym. Compos.* **21,** 449–456 (2013).
82. Yu, C., Xu, M., Svec, F. & Frechet, J. M. J. Preparation of monolithic polymers with controlled porous properties for microfluidic chip applications using photoinitiated free-radical polymerization. *J. Polym. Sci. Part A Polym. Chem.* **40,** 755–769 (2002).
83. He, M., Zeng, Y., Jemere, A. B. & Harrison, D. J. Tunable thick polymer coatings for on-chip electrophoretic protein and peptide separation. *J. Chromatogra. A* **1241,** 112–116 (2012).
84. He, B., Tait, N. & Regnier, F. Fabrication of nanocolumns for liquid chromatography. *Anal. Chem.* **70,** 3790–3797 (1998).
85. Rosqvist, T. & Johansson, S. Soft micromolding and lamination of piezoceramic thick films. *Sensors Actuators, A Phys.* **97-98,** 512–519 (2002).
86. Gentile, F. *et al.* The five Ws (and one H) of super-hydrophobic surfaces in medicine. *Micromachines* **5,** 239–262 (2014).
87. Wirth, M. J. Separation media for microchips. *Anal. Chem.* **79,** 800–808 (2007).
88. Meistermann, L. & Tinland, B. DNA electrophoresis in a monodisperse porous medium. *Phys. Rev. E* **62,** 4014–4017 (2000).
89. Zhang, H. & Wirth, M. J. Electromigration of single molecules of DNA in a crystalline array of 300-nm silica colloids. *Anal. Chem.* **77,** 1237–1242 (2005).
90. Xia, Y., Gates, B., Yin, Y. & Lu, Y. Monodispersed colloidal spheres: Old materials with new applications. *Adv. Mater.* **12,** 693–713 (2000).
91. Xia, Y. *et al.* One-Dimensional Nanostructures: Synthesis, Characterization, and Applications. *Adv. Mater.* **15,** 353–389 (2003).
92. Wei, B., Malkin, D. S. & Wirth, M. J. Plate Heights below 50 nm for Protein Electrochromatography Using Silica Colloidal Crystals. *Anal. Chem.* **82,** 10216–

10221 (2010).

93. Liao, T., Guo, Z., Li, J., Liu, M. & Chen, Y. One-step packing of anti-voltage photonic crystals into microfluidic channels for ultra-fast separation of amino acids and peptides. *Lab Chip* **13,** 706–713 (2013).

94. Chirica, G. S. & Remcho, V. T. Fritless capillary columns for HPLC and CEC prepared by immobilizing the stationary phase in an organic polymer matrix. *Anal. Chem.* **72,** 3605–3610 (2000).

95. Xie, R. & Oleschuk, R. D. Photoinduced polymerization for entrapping of octadecylsilane microsphere columns for capillary electrochromatography. *Anal. Chem.* **79,** 1529–1535 (2007).

96. Gibson, G. T. T., Mugo, S. M. & Oleschuk, R. D. Surface-mediated effects on porous polymer monolith formation within capillaries. *Polymer (Guildf).* **49,** 3084–3090 (2008).

97. Gibson, G. T. T. *et al.* Entrapment of functionalized silica microspheres with photo-initiated acrylate-based polymers. *J. Colloid Interface Sci.* **320,** 82–90 (2008).

98. Gibson, G. T. T., Marecak, D. M. & Oleschuk, R. D. Reversed phase capillary HPLC using polymer-entrapped C18 particles. *J. Sep. Sci.* **32,** 4025–4032 (2009).

99. Rocco, A. & Fanali, S. Capillary electrochromatography without external pressure assistance: Use of packed columns with a monolithic inlet frit. *J. Chromatogra. A* **1191,** 263–267 (2008).

100. Ying, L., Wang, P., Kang, E. T. & Neoh, K. G. Synthesis and Characterization of Poly (acrylic acid) -graft-poly (vinylidene fluoride) Copolymers and pH-Sensitive Membranes. *Macromolecules* **35,** 673–679 (2002).

101. Kato, K., Uchida, E., Kang, E. T., Uyama, Y. & Ikada, Y. Polymer surface with graft chains. *Prog. Polym. Sci.* **28,** 209–259 (2003).

102. Norris, D. J., Arlinghaus, E. G., Meng, L., Heiny, R. & Scriven, L. E. Opaline photonic crystals: How does self-assembly work? *Adv. Mater.* **16,** 1393–1399 (2004).

103. Rohr, T., Hilder, E. F., Donovan, J. J., Svec, F. & Frechet, J. M. J. Photografting and the control of surface chemistry in three-dimensional porous polymer

monoliths. *Macromolecules* **36,** 1677–1684 (2003).

104. Yang, W., Zhang, L., Wang, S., White, A. D. & Jiang, S. Functionalizable and ultra stable nanoparticles coated with zwitterionic poly(carboxybetaine) in undiluted blood serum. *Biomaterials* **30,** 5617–5621 (2009).
105. Li, G. *et al.* Ultra low fouling zwitterionic polymers with a biomimetic adhesive group. *Biomaterials* **29,** 4592–4597 (2008).
106. Cheng, G. *et al.* Zwitterionic carboxybetaine polymer surfaces and their resistance to long-term biofilm formation. *Biomaterials* **30,** 5234–5240 (2009).
107. Zhang, Z., Chen, S., Chang, Y. & Jiang, S. Surface grafted sulfobetaine polymers via atom transfer radical polymerization as superlow fouling coatings. *J. Phys. Chem. B* **110,** 10799–10804 (2006).
108. Delgado, A. V., González-Caballero, F., Hunter, R. J., Koopal, L. K. & Lyklema, J. Measurement and interpretation of electrokinetic phenomena. *J. Colloid Interface Sci.* **309,** 194–224 (2007).
109. Zhao, C. & Yang, C. Advances in electrokinetics and their applications in micro/nano fluidics. *Microfluid. Nanofluidics* **13,** 179–203 (2012).
110. Sartori, A., Barbier, V. & Viovy, J. L. Sieving mechanisms in polymeric matrices. *Electrophoresis* **24,** 421–440 (2003).
111. Rahong, S. *et al.* Three-dimensional Nanowire Structures for Ultra-Fast Separation of DNA, Protein and RNA Molecules. *Sci. Rep.* **5,** 10584 (2015).
112. Masliyah, J. H. & Bhattacharjee, S. *Electrokinetic and Colloid Transport Phenomena*. *Electrokinetic and Colloid Transport Phenomena* (2005). doi:10.1002/0471799742
113. Bhuyan, A. K. On the mechanism of SDS-induced protein denaturation. *Biopolymers* **93,** 186–199 (2010).
114. Shirahama, K., Tsujii, K. & Takagi, T. Free boundary electrophoresis of sodium dodecyl sulfate protein polypeptide complexes with special reference to SDS polyacrylamide gel electrophoresis. *J. Biochem.* **75,** 309–319 (1974).
115. Slater, G. W., Mayer, P. & Drouin, G. *High Resolution Separation and Analysis of Biological Macromolecules Part A: Fundamentals*. *Methods in Enzymology* (Academic Press, 1996). doi:10.1016/S0076-6879(96)70014-9

116. Kozulić, B. Models of gel electrophoresis. *Analytical Biochemistry* **231,** 1–12 (1995).
117. Viovy, J.-L. Electrophoresis of DNA and other polyelectrolytes: Physical mechanisms. *Rev. Mod. Phys.* **72,** 813–872 (2000).
118. Lommasson, C., Herman, J. J., Lippman, L., Metmer, R. & Neill, J. O. No Title. **212,** (1970).
119. Ogston, A. G. The spaces in a uniform random suspension of fibres. *Trans. Faraday Soc.* **54,** 1754–1757 (1958).
120. Guttman, a. On the separation mechanism of capillary sodium dodecyl sulfate-gel electrophoresis of proteins. *Electrophoresis* **16,** 611–6 (1995).
121. Grossman, P. D., Menchen, S. & Hershey, D. Quantitative analysis of DNA-sequencing electrophoresis. *Gata* **9,** 9–16 (1992).
122. Klein, J. Evidence for reptation in an entangled polymer melt. *Nature* **271,** 143–145 (1978).
123. Lumpkin, O., Déjardin, P. & Zimm, B. Theory of gel electrophoresis of DNA. *Biopolymers* **24,** 1573–1593 (1985).
124. Giddings, J. C. Generation of Variance, 'Theoretical Plates,' Resolution, and Peak Capacity in Electrophoresis and Sedimentation. *Sep. Sci.* **4,** 181–189 (1969).
125. Fornstedt, T., Forssén, P. & Westerlund, D. *Basic HPLC Theory and Definitions: Retention, Thermodynamics, Selectivity, Zone Spreading, Kinetics, and Resolution*. (Wiley, 2015).
126. Heiger, D. *High-performance capillary electrophoresis: An introduction*. (Agilent Technologies, 2000). doi:10.1039/9781847550521-00208
127. Huang, X., Coleman, W. F. W. & Zare, R. N. Analysis of factors causing peak broadening in capillary zone electrophoresis. *J. Chromatogr. A* **480,** 95–110 (1989).
128. Schwartz, H. & Pritchett, T. in 66 (Beckman Coulter, 1994). at <http://www.ibt.unam.mx/computo/pdfs/met/Electroforesis/Electroforesis/CE/General/Aplicaciones/Proteins.pdf>
129. Kämpfe, B., Luczak, F. & Michel, B. Energy Dispersive X-Ray Diffraction. *Part. Part. Syst. Charact.* **22,** 391–396 (2005).

130. Hofmann, J. P., Rohnke, M. & Weckhuysen, B. M. Recent advances in secondary ion mass spectrometry of solid acid catalysts: large zeolite crystals under bombardment. *Phys. Chem. Chem. Phys.* **16,** 5465–74 (2014).
131. Tobergte, D. R. & Curtis, S. *An Introduction to SURFACE ANALYSIS by XPS and AES*. (Wiley, 2013). doi:10.1017/CBO9781107415324.004
132. Simmons, C. *Experimental techniques of Glass Science*. (Amer Ceramic Society, 1993).
133. Stroud, R. M. in *Treatise on Geochemistry: Second Edition* **15,** 231–244 (2013).
134. Michler, G. H. in *Electron Microscopy of Polymers* 473 (2008).
135. Jemere, A. B., Oleschuk, R. D., Ouchen, F., Fajuyigbe, F. & Harrison, D. J. An integrated solid-phase extraction system for sub-picomolar detection. *Electrophoresis* **23,** 3537–3544 (2002).
136. Ye, W. DNA electrophoresis in colloidal self-assembled arrays. (University of Alberta, 2013).
137. Seller, K., Fan, Z. H., Flurl, K. & Harrison, D. J. Electroosmotic Pumping and Valveless Control of Fluid Flow within a Manifold of Capillaries on a Glass Chip. *Anal. Chem.* **66,** 3485–3491 (1994).
138. He, M. & Harrison, D. J. Parameters governing reproducibility of flow properties of porous monoliths photopatterned within microfluidic channels. *Electrophoresis* **31,** 2422–2428 (2010).
139. Aoki, H., Tanaka, N., Kubo, T. & Hosoya, K. Polymer-based monolithic columns in capillary format tailored by using controlled in situ polymerization. **32,** 341–358 (2009).
140. Yu, C., Davey, M. H., Svec, F., Fre, J. M. J. & Berkeley, E. O. L. Monolithic Porous Polymer for On-Chip Solid-Phase Extraction and Preconcentration Prepared by Photoinitiated in Situ Polymerization within a Microfluidic Device. *Anal. Chem.* **73,** 5088–5096 (2001).
141. Katarzyna Chudaa, Joanna Jasika, Julien Carlierb, Pierre Tabourierb, Christian Druonb, Xavier Coquereta. Characteristics and fluidic properties of porous monoliths prepared by radiation-induced polymerization for Lab-on-a-Chip applications. *Radiat. Phys. Chem.* **75,** 26–33 (2006).

142. Nazemifard, N. *et al.* A systematic evaluation of the role of crystalline order in nanoporous materials on DNA separation. *Lab Chip* **12,** 146–152 (2012).
143. Brodowski, S., Amelung, W., Haumaier, L., Abetz, C. & Zech, W. Morphological and chemical properties of black carbon in physical soil fractions as revealed by scanning electron microscopy and energy-dispersive X-ray spectroscopy. *Geoderma* **128,** 116–129 (2005).
144. Bexell, U. L. F. Surface Characterisation Using ToF-SIMS , AES and XPS of Silane Films and Organic Coatings Deposited on Metal Substrates. (Acta Universitis, 2003).
145. Benninghoven, A. Chemical Analysis of Inorganic and Organic Surfaces and Thin Films by Static Time-of-Flight Secondary Ion Mass Spectrometry (TOF-SIMS). *Angew. Chem., Int. Ed.* **33,** 1023–1043 (1994).
146. Xu, H. *et al.* Preparation and characterization of a dual-receptor mesoporous silica nanoparticle–hyaluronic acid–RGD peptide targeting drug delivery system. *RSC Adv.* **6,** 40427–40435 (2016).
147. Ma, M., Niekiel, F., Wondraczek, L., Bitzek, E. & Spiecker, E. In situ mechanical quenching of nanoscale silica spheres in the transmission electron microscope. *Scr. Mater.* **121,** 70–74 (2016).
148. Peng, R. & Li, D. Journal of Colloid and Interface Science Effects of ionic concentration gradient on electroosmotic flow mixing in a microchannel. *J. Colloid Interface Sci.* **440,** 126–132 (2015).
149. Vanorman, B. B., Liversidge, G. G., Mcintire, G. L., Olefirowicz, T. M. & Ewing, A. G. Effects of Buffer Composition on Electroosmotic Flow in Capillary Electrophoresis. *J. Microcolumn Sep.* **180,** 176–180 (1990).
150. Lucy, C. A., Macdonald, A. M. & Gulcev, M. D. Non-covalent capillary coatings for protein separations in capillary electrophoresis. *J. Chromatogr. A* **1184,** 81–105 (2008).
151. Leinweber, F. C., Stein, J. & Otto, M. Capillary zone electrophoresis of proteins with poly (2-hydroxyethyl methacrylate) -coated capillaries : fundamentals and applications. *Fresenius. J. Anal. Chem.* **370,** 781–788 (2001).
152. Grushka, E., McCormick, J. R. M. & Kirkland, J. J. Effect of Temperature

Gradients on the Efficiency of Capillary Zone Electrophoresis Separations. *Anal. Chem.* **61,** 241–246 (1989).

153. Horiuchi, K. & Dutta, P. Joule heating effects in electroosmotically driven microchannel flows. *Int. J. Heat Mass Transf.* **47,** 3085–3095 (2004).
154. Weber, K. & Osborn, M. The reliability of molecular weight determinations by dodecyl sulfate-polyacrylamide gel electrophoresis. *J. Biol. Chem.* **244,** 4406–12 (1969).
155. Guttman, A., Nolan, J. A. & Cooke, N. Capillary sodium dodecyl sulfate gel electrophoresis of proteins. *J. Chromatogr. A* **17,** 1333–1341 (1993).
156. Harlow, E. & Lane, D. Antibodies: A Laboratory Manual. 726 (1988). doi:10.1016/0968-0004(89)90307-1
157. Goding, J. W. Conjugation of Antibodys with Fluorochromes: Modification of the standard methods. *J. Immunol. Methods* **13,** 215–226 (1976).
158. Jemere, A. B., Oleschuk, R. D., Ouchen, F., Fajuyigbe, F. & Harrison, D. J. An integrated solid-phase extraction system for sub-picomolar detection. *Electrophoresis* **23,** 3537–3544 (2002).
159. Jacobson, S. C., Hergenorder, R., Kounty, L. B., Warmack, R. J. & Ramsey, M. J. High-speed separations on a microchip. *Anal. Chem.* **66,** 1114–1118 (1994).
160. Hawkes, S. J. Modernization of the van Deemter equation for chromatographic zone dispersion. *J. Chem. Educ.* **60,** 393 (1983).
161. Ericson, C., Holm, J., Ericson, T. & Hejerten, S. Electroosmosis- and pressure-driven chromatography in chips using continuous beds. *Anal. Chem.* **72,** 81–87 (2000).
162. Liu, Y., Foote, R. S., Jacobson, S. C., Ramsey, R. S. & Ramsey, M. J. Electrophoretic separation of proteins on a microchip with noncovalent, postcolumn labeling. *Anal. Chem.* **72,** 4608–4613 (2000).
163. King, S. B. & Dorfman, K. D. Role of order during Ogston sieving of DNA in colloidal crystals. *Anal. Chem.* **85,** 7769–7776 (2013).
164. Wang, C. *et al.* Two- Dimensional Ordered Arrays of Silica Nanoparticles. *Chem. Mater* **12,** 3662–3666 (2000).
165. Graslund, S. Protein production and purification. *Nat. Methods* **5,** 135–146 (2008).

166. Rifai, N., Gillette, M. A. & Carr, S. A. Protein biomarker discovery and validation : the long and uncertain path to clinical utility. **24,** 971–983 (2006).
167. Sheehan, D. & Sullivan, S. O. Protein Electrophoresis. *Mol. Biomethods Handb.* **869,** 351–363 (2008).
168. Boechat, L. H. B. & Zollner, R. L. Reactivity of anti-thyroid antibodies to thyroglobulin tryptic fragments: Comparison of autoimmune and non-autoimmune thyroid diseases. *Brazilian J. Med. Biol. Res.* **32,** 449–455 (1999).
169. Oh-Ishi, M. & Maeda, T. Separation techniques for high-molecular-mass proteins. *J. Chromatogra. B* **771,** 49–66 (2002).
170. Rabilloud, T. Two-dimensional gel electrophoresis in proteomics: Old, old fashioned, but it still climbs up the mountains. *Proteomics* **2,** 3–10 (2002).
171. Fritz, J. D., Swartz, D. R. & Greaser, M. L. Factors affecting polyacrylamide gel electrophoresis and electroblotting of high-molecular-weight myofibrillar proteins. *Anal. Biochem.* **180,** 205–210 (1989).
172. Roncada, P. *et al.* Acrylamide-agarose copolymers: Improved resolution of high molecular mass proteins in two-dimensional gel electrophoresis. *Proteomics* **5,** 2331–2339 (2005).
173. Miller, I., Eberini, I. & Gianazza, E. Other than IPG-DALT: 2-DE variants. *Proteomics* **10,** 586–610 (2010).
174. Matte, A. *et al.* Performance of a novel sieving matrix of poly(vinyl alcohol)/acrylamide copolymer in electrophoretic separations of high molecular weight proteins from red cell membrane. *Electrophoresis* **35,** 1081–1088 (2014).
175. Agirregabiria, M. *et al.* SDS-CGE of proteins in microchannels made of SU-8 films. *Electrophoresis* **27,** 3627–3634 (2006).
176. Zhang, S. H., Zhang, J. & Horvath, C. J. Rapid separation of peptides and proteins by isocratic capillary electrochromatography at elevated temperature. *J. Chromatogra. A* **914,** 189–200 (2001).
177. Jin, S., Anderson, G. J. & Kennedy, R. T. Western blotting using microchip electrophoresis interfaced to a protein capture membrane. *Anal. Chem.* **85,** 6073–6079 (2013).
178. Lin, Q.-H., XCheng, Y.-Q., Dong, Y.-N., Pan, J.-Z. & Fang, Q. High-speed

separation of proteins by sodium dodecyl sulfate-capillary gel electrophoresis with partial translational spontaneous sample injection. *Electrophoresis* **32,** 2603–2898 (2011).

179. Jemere, A. B., Oleschuk, R. D. & Harrison, D. J. Microchip-based capillary electrochromatography using packed beds. *Electrophoresis* **24,** 3018–3025 (2003).
180. Jemere, A. B., Martinez, D., Finot, M. & Harrison, D. J. Capillary electrochromatography with packed bead beds in microfluidic devices. *Electrophoresis* **30,** 4237–4244 (2009).
181. Kim, D. & Herr, A. E. Protein immobilization techniques for microfluidic assays. *Biomicrofluidics* **7,** 1–47 (2013).
182. Fonslow, B. R. *et al.* Trajectory of isoelectric focusing from gels to capillaries to immobilized gradients in capillaries. *Proteomics* **10,** 54–56 (2013).
183. Malekpourkoupaei, A., Kostiuk, L. W. & Harrison, D. J. Fabrication of binary opal lattices in microfluidic devices. *Chem. Mater.* **25,** 3808–3815 (2013).
184. Reyes, D. R., Iossifidis, D., Auroux, P.-A. & Manz, A. Micro total analysis systems. 1. Introduction, theory, and technology. *Anal. Chem.* **74,** 2623–2636 (2002).
185. Auroux, P. A., Iossifidis, D., Reyes, D. R. & Manz, A. Micro total analysis systems. 2. Analytical standard operations and applications. *Anal. Chem.* **74,** 2637–2652 (2002).
186. Pamme, N. Continuous flow separations in microfluidic devices. *Lab Chip* **7,** 1644–59 (2007).
187. Whitesides, G. M. The origins and the future of microfluidics. *Nature* **442,** 368–73 (2006).
188. Horbett, T. A. The role of adsorbed proteins in animal cell adhesion. *Colloids Surfaces B Biointerfaces* **2,** 225–240 (1994).
189. Horvath, J. & Dolník, V. Polymer wall coatings for capillary electrophoresis. *Electrophoresis* **22,** 644–655 (2001).
190. Liu, J. & Lee, M. L. Permanent surface modification of polymeric capillary electrophoresis microchips for protein and peptide analysis. *Electrophoresis* **27,** 3533–3546 (2006).

191. Mccormick, R. M. Capillary Zone Electrophoretic Separation of Peptides and Proteins Using Low pH Buffers in Modified Silica Capillaries. *Anal. Chem.* **60,** 2322–2328 (1988).
192. Munce, N. R., Li, J., Herman, P. R. & Lilge, L. D. Microfabricated System for Parallel Single Cell Capillary Electrophoresis. *Anal. Chem.* **76,** 4983–4989 (2004).
193. Sakai-Kato, K., Kato, M. & Toyo'oka, T. On-line trypsin-encapsulated enzyme reactor by the sol-gel method integrated into capillary electrophoresis. *Anal. Chem.* **74,** 2943–2949 (2002).
194. Belder, D. & Ludwig, M. Surface modification in microchip electrophoresis. *Electrophoresis* **24,** 3595–3606 (2003).
195. Bushey, M. M. & Jorgenson, J. W. Capillary electrophoresis of proteins in buffers containing high concentrations of zwitterionic salts. *J. Chromatogr. A* **480,** 301–310 (1989).
196. Cao, F., Tan, L., Xiang, L., Liu, S. & Wang, Y. Application of the copolymers containing sulfobetaine methacrylate in protein separation by capillary electrophoresis. *J. Biomater. Sci. Polym. Ed.* **24,** 2058–70 (2013).
197. Green, J. S. & Jorgenson, J. W. Minimizing adsorption of proteins on fused silica in capil- lary zone electrophoresis by the addition of alkali metal salts to the buffers. *J. Chromatogr.* **478,** 63–70 (1989).
198. Oster, G., Shibata, O., To, L. & Editors, T. H. E. Graft copolymer of polyacrylamide and natural rubber produced by means of ultraviolet light. *J. Polym. Sci.* **26,** 233–234 (1957).
199. Yang, W. T. & Ranby, B. Bulk surface photografting process and its application. III. Photolamination of polymer films. *J. Appl. Polym. Sci.* **63,** 1723–1732 (1997).
200. Rånby, B. Surface modification and lamination of polymers by photografting. *Int. J. Adhes. Adhes.* **19,** 337–343 (1999).
201. Griebenow, K. & Klibanov, A. M. On protein denaturation in aqueous-organic mixtures but not in pure organic solvents. *J. Am. Chem. Soc.* **118,** 11695–11700 (1996).
202. Silverstein M.Robert, Webster X. Francis, K. J. D. Spectrometric Identification of Organic Compounds. *Organic Chemistry* 1–550 (2005). doi:10.1016/0022-

2860(76)87024-X

203. Jiang, W., Awasum, J. N. & Irgum, K. Control of electroosmotic flow and wall interactions in capillary electrophosesis capillaries by photografted zwitterionic polymer surface layers. *Anal. Chem.* **75,** 2768–2774 (2003).
204. Emerick, E., Grant, S. & Bernards, M. Electrospinning of Sulfobetaine Methacrylate Nanofibers. *Chem. Eng. Process Tech.* **1003,** 1–6 (2013).
205. Lewis, A. L. Phosphorylcholine-based polymers and their use in the prevention of biofouling. *Colloids Surfaces B Biointerfaces* **18,** 261–275 (2000).
206. Ishihara, K. *et al.* Why do phospholipid polymers reduce protein adsorption? *J. Biomed. Mater. Res.* **39,** 323–330 (1998).
207. Zhang, Z. *et al.* Nonfouling behavior of polycarboxybetaine-grafted surfaces: Structural and environmental effects. *Biomacromolecules* **9,** 2686–2692 (2008).
208. Yang, W., Xue, H., Li, W., And, J. Z. & Jiang, S. Pursuing 'zero' protein adsorption of poly(carboxybetaine) from undiluted blood serum and plasma. *Langmuir* **25,** 11911–11916 (2009).
209. Zhang, Z., Chen, S. & Jiang, S. Dual-Functional Biomimetic Materials : Nonfouling Poly (carboxybetaine) with Active Functional Groups for Protein Immobilization. *Biomacromolecules* **7,** 3311–3315 (2006).
210. Zhang, Z., Chao, T. & Jiang, S. Physical, chemical, and chemical-physical double network of zwitterionic hydrogels. *J. Phys. Chem. B* **112,** 5327–5332 (2008).
211. Yang, W., Cheng, G. & Jiang, S. Film thickness dependence of protein adsorption from blood serum and plasma onto poly(sulfobetaine) and poly(carboxybetaine)-grafted surfaces. *Langmuir* **24,** 9211–9214 (2008).
212. Micheletto, R., Fukuda, H. & Ohtsu, M. A Simple Method for the Production of a Two-Dimensional, Ordered Array of Small Latex Particles. *Langmuir* **11,** 3333–3336 (1995).
213. Denkov, N. *et al.* Mechanism of formation of two-dimensional crystals from latex particles on substrates. *Langmuir* **8,** 3183–3190 (1992).
214. Huang, Y. & Pemberton, J. E. Fabrication of colloidal arrays by self-assembly of sub-100nm silica particles. *Colloids Surfaces A Physicochem. Eng. Asp.* **377,** 76–86 (2011).

215. Malekpourkoupaei, A. Fabrication of colloidal crystals featuring sub-20 nm pore size for protein separation. (University of Alberta, 2012).
216. Dimitrov, A. S. & Nagayama, K. Continuous Convective Assembling of Fine Particles into Two-Dimensional Arrays on Solid Surfaces. *Langmuir* **12,** 1303–1311 (1996).
217. Dufresne, E. R. *et al.* Flow and Fracture in Drying Nanoparticle Suspensions. *Phys. Rev. Lett.* **91,** 224501 (2003).
218. Lan, D. & Wang, Y. Cracks formation in the vertical co-depositing colloidal crystal. in *13th International Conference on Fracture（ICF13）* 1–5 (2013). at <http://www.gruppofrattura.it/ocs/index.php/ICF/icf13/paper/download/11428/10807>
219. Mason, G. Radial Distribution Functions from Small Packings of Spheres. *Nature* **217,** 733–735 (1968).
220. Aste, T. Variations around disordered close packing. *J. Phys. Condens. Matter* **17,** 2361–2390 (2005).
221. Jiang, P., Bertone, J. F., Hwang, K. S. & Colvin, V. L. Single-Crystal Colloidal Multilayers of Controlled Thickness. *Chem. Mater.* **11,** 2132–2140 (1999).
222. Salas-Solano, O. *et al.* Optimization and validation of a quantitative capillary electrophoresis sodium dodecyl sulfate method for quality control and stability monitoring of monoclonal antibodies. *Anal. Chem.* **78,** 6583–6594 (2006).
223. Shen, Y. & Smith, R. D. Proteomics based on high-efficiency capillary separations. *Electrophoresis* **23,** 3106–3124 (2002).
224. Hunt, G. & Nashabeh, W. Capillary electrophoresis sodium dodecyl sulfate nongel sieving analysis of a therapeutic recombinant monoclonal antibody: a biotechnology perspective. *Anal. Chem.* **71,** 2390–2397 (1999).
225. Henzel, W. J., Watanabe, C. & Stults, J. T. Protein identification: The origins of peptide mass fingerprinting. *J. Am. Soc. Mass Spectrom.* **14,** 931–942 (2003).
226. Hustoft, H. K. *et al.* A Critical Review of Trypsin Digestion for LC-MS Based Proteomics. *Integr. Proteomics* 73–92 (2010). doi:10.5772/2473